Nanobiosensors Targeting Affordable Detection of Biomarkers and Pathogens: Experimental and Computational Outlook

A thesis submitted

in partial fulfilment of the requirements for the degree of

Doctor of Philosophy

Submitted by

Mitali Basak

Roll No: 186153003

Under the Guidance

of

Prof. Dipankar Bandyopadhyay

and

Prof. Harshal B. Nemade

Centre for Nanotechnology

Indian Institute of Technology Guwahati

June 2024

STATEMENT

- **Title of Thesis:** Nanobiosensors Targeting Affordable Detection of Biomarkers and Pathogens: Experimental and Computational Outlook.
- The thesis is submitted for the **Degree of Doctor of Philosophy (Ph.D.)**
- The results reported is research carried out by myself at the Centre for Nanotechnology, Indian Institute of Technology Guwahati, India with the supervision of Prof. Dipankar Bandyopadhyay and Prof. Harshal B. Nemade.
- Specifications regarding thesis format have been closely followed.
- The contents of the thesis have been organized based on the guidelines.
- The thesis has been prepared without resorting to plagiarism.
- All sources have been acknowledged appropriately wherever the work derived is based on the findings of other sources, in accordance with the general practice of reporting scientific observations.
- The thesis has not been submitted elsewhere for a degree.

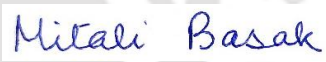

June, 2024 **Mitali Basak**

Centre for Nanotechnology **Ph.D. Student**

Indian Institute of Technology Guwahati, India **Roll No.: 186153003**

CERTIFICATE

This is to certify that the research works performed in the thesis entitled, "Nanobiosensors Targeting Affordable Detection of Biomarkers and Pathogens: Experimental and Computational Outlook" by **Ms. Mitali Basak**, have been carried out under our supervision and this work has not been submitted elsewhere for a degree.

Prof. Dipankar Bandyopadhyay
Supervisor
Professor
Department of Chemical Engineering
Indian Institute of Technology Guwahati

Prof. Harshal B. Nemade
Co-Supervisor
Professor
Department of Electronics and Electrical Engineering
Indian Institute of Technology Guwahati

ACKNOWLEDGEMENT

First and foremost, I would like to express my sincere gratitude to the Centre for Nanotechnology, Indian Institute of Technology Guwahati for providing me a platform to pursue my Ph.D. I am also thankful to my course instructors for enriching me with the fundamental knowledge of semiconductors, microfluidics, and nanotechnology.

Many thanks and praises to my thesis supervisors Prof. Dipankar Bandyopadhyay, and Prof. Harshal B. Nemade for their guidance, teaching, and continuous support. It is indeed an honor for me to work with professors with a positive attitude. They have acquainted me with the state-of-art research and gave me the opportunity to carry out my thesis work under their supervision. Their dynamism, vision, sincerity, and motivation have deeply inspired me.

I would also like to express my heartfelt gratitude to the doctoral committee members Prof. Chandan Das, Prof. Tapas Kumar Mandal, and Prof. Nageswara Rao Peela for their constructive feedback and critical evaluation of my research works, which have indeed enriched the upgradation of the thesis.

My sincere gratitude to Prof. Amaresh Dalal, Department of Mechanical Engineering, Indian Institute of Technology Guwahati and his family for providing parental support and academic guidance during the course of my thesis work.

I thank all the faculty and staff members of the Centre for Nanotechnology, the Department of Chemical Engineering, R&D section, Central Instrumental Facility, and academic section for all the help I received since the inception of my Ph.D.

My sincere gratitude to my labmates, my seniors, juniors and friends for helping me whenever required during my thesis work. Many thanks to Dr. Shirsendu Mitra for his endless guidance and help during carrying out the experiments and teaching me the correct pathway to analyze the outcomes which have upgraded the quality of the thesis

proposition enormously. I am thankful to my collaborators Dr. Swapnil Sinha, CEO Altanostics Pvt. Ltd, and Dr. Monika Sachdev, Scientist, Central Drug Research Institute, Lucknow for supportive interaction. I am also thankful to my all-other lab mates for their support and presence at any time of need.

I also acknowledge the Department of Science and Technology (DST), Ministry of Higher Education, and Ministry of Electronics and Information Technology (MeitY), IMPRINT MHRD for all the financial supports.

Finally, I am thankful to my beloved family for being the strongest support always and for their love, care and detriments for educating and preparing me for my future.

CONTENTS

LIST OF FIGURES

LIST OF TABLES

LIST OF ABBREVIATIONS

Abbreviation	Description	Abbreviation	Description
WHO	World health organization	**LOD**	Limit of detection
UN	United nations	**ADC**	Analog to digital converter
SDGs	Sustainable development goals	**Au NTs**	Gold nanotwins
NCDs	Non-communicable diseases	**EC**	*Escherichia coli*
POCT	Point-of-care testing	**UTI**	Urinary tract infection
STIs	Sexually transmitted infections	**APTES**	3-aminopropyl-triethoxysilane
FMI	Future market insight	**HAIs**	Healthcare associated infections
MEMs	Micro-electro-mechanical systems	**TCEP**	Tris (2–carboxyethyl) phosphine
IoMT	Internet of Medical things	**C_{10}**	1, 10–alkanedithiol
ELISA	Enzyme–linked immunosorbent assay	**TE**	Tris–EDTA
SPR	Surface plasmon resonance	**MTTC**	Microbial type culture collection
LSPR	Localized surface plasmon resonance	**EF**	Enterococcus faecalis
TERS	Tip enhanced Surface Raman Spectroscopy	**KP**	Klebsiella pneumoniae
SORS	Spatially offset Raman Spectroscopy	**SA**	Streptococcus aureus
SERRS	Surface enhanced resonance Raman spectroscopy	**LB**	Luria-bertani
SEIRS	Surface enhanced infrared spectroscopy	**FEM**	Finite element method
PSLR	Periodic surface lattice resonance	**PARDISO**	Parallel direct sparse solver
Ag	Antigen	**PML**	Perfectly matched layer
PP1Ɣ2	Protein–Phosphatase–1–gamma–2	**FESEM**	Field emission scanning electron microscope
CaCx	Cervical cancer	**R6G**	Rhodamine 6G
NCB–Ag	Novel Cancer Biomarker antigen	**Apt**	Aptamer
Au NPs	Gold nanoparticles	**Au NRs**	Gold nanorods
DTSP	3,3'–dithiodipropionic–acid–di(n–hydroxy–succinimide–ester)	**Ag–Au NRs**	Silver shelled gold nanoparticles
Ab	Antibody	**Cho**	Cholesterol
LED	Light emitting diode	**TG**	Tri-glyceride
HPV	Human papilloma virus	**SERS**	Surface enhanced raman spectroscopy
NCRP	National cancer registry program	**HDL**	High density lipoprotein
VILI	Visual inspection by applying Lugol's Iodine	**LDL**	Low density lipoprotein
VIA	Visual inspection by applying Acetic Acid	**VLDL**	Very low density lipoprotein
WB	Western-blot	**NCEP**	National cholesterol education program
GE	Gel-electrophoresis	**H_2SO_4**	Sulphuric acid
PCR	Polymerase chain reaction	**AA**	Ascorbic acid
CKD	Chronic kidney dysfunction	**$AgNO_3$**	Silver nitrate
SAW	Surface acoustic wave	**CTAB**	Cetyltrimethylammonium bromide
FET	Field effect transistor	**DTNB**	5,5′–dithiobis–(2–nitrobenzoic acid)
EDL	Electrical double layer	**4-ATP**	4–aminothiophenol
$HAuCl_4$	Tetrachloroauric acid	**EDC**	1–ethyl–3–(3–dimethylaminopropyl)carbodiimide
$NaBH_4$	Sodium borohydride	**NHS**	N–hydroxysuccinimide
BSA	Bovine serum albumin	**ChOx**	Cholesterol oxidase
HCl	Hydrochloric acid	**Lp**	Lipase
NaOH	Sodium hydroxide	**IPA**	Isopropanol

$Na_2HPO_4.7H_2O$	Di-sodium hydrogen phosphate	**MES**	2–(N–morpholino) ethanesulfonic acid
KH_2PO_4	Potassium di-hydrogen phosphate	**SAED**	Selected area electron diffraction
NaCl	Sodium chloride	**DP**	Diffraction pattern
KCl	Potassium chloride	**HRTEM**	High–resolution transmission emission microscopy
BME	B-mercaptoethanol	**FTIR**	Fourier transform infrared spectroscopy
HRP	Horseradish peroxide	**D-Glu**	D–glucose
RIPA	Radio-immunoprecipitation assay buffer	**NaCl**	Sodium ion
PEG	Polyethylene glycol	**KCl**	Potassium ion
CVF	Cervico-vaginal fluid	***T***	Temperature
PBS	Phosphate buffered saline	***RH***	Relative humidity
PBST	Phosphate Buffered Saline with Tween-20	**Virulets**	Virus laden respiratory microdroplets
SDS-PAGE	Sodium Dodecyl Sulfate-polyacrylamide Gel Electrophoresis	**SARS-CoV-2**	Severe–acute–respiratory–syndrome coronavirus 2
TEM	Transmission electron microscope	**ICU**	Intensive care units
CIN	Cervical intraepithelial neoplasia	**FPT**	Fluid–particle–tracing

LIST OF SYMBOLS

Symbol	Description	Symbol	Description
A_N	normalized absorbance	d	Diameter of droplet
$\Delta\lambda$	wavelength shift	μ_d	dynamic viscosity of the droplet
σ_{blank}	standard deviation of the blank sample	x_f	distance travelled by the droplet in the x–direction
k_0	wavenumber in free space	h	height of the nose inlet from the ground
μ_r	relative permeability of the medium	$f(n)$	probability of finding number of viruses inside a virulet
ε_r	relative permittivity of the medium	$V_L(d)$	viral load
σ	electrical conductivity	C_v	viral concentration
ω	angular frequency	N_d	number of droplets in 1 mL of water
E_b	plane wave	E_v	the total fraction of all the droplets that are loaded with virus
E_0	amplitude of the incident electric field	N_v	number of droplets containing virus
λ	wavelength	$n_{\max}$	maximum number of viruses
E_{sca}	scattered field	$\mathbf{F}_d^{Dx}$	x–directional drag force
I_{SERS}	SERS intensity	$\mathbf{F}_d^{Dy}$	*y*–directional drag force
I_{RAMAN}	RAMAN intensity	$\mathbf{F}_d^{Ix}$	*x*–directional inertia force
C_{SERS}	concentration of R6G considered for the SERS	$\mathbf{F}_d^{Iy}$	negative *y*–directional inertia force
C_{RAMAN}	concentration of R6G considered for the Raman	t_s	settling time of virulets
$E_{\max}$	maximum electric field	V_s	velocity of the virulet of radius R_0
I_N	normalized intensity	d_e	diameter of the virulets after complete evaporation
$\boldsymbol{I_{SERS\_N}}$	normalized SERS intensity	t_{eva}	evaporation time
$\mathbf{u}_f$	velocity vectors of the fluid	t_e	settling time of the miniaturized droplets after evaporation
$\mathbf{u}_d$	velocity vectors of the droplet	V_{virus}	volume of one virus
∇	gradient operator	$(\mathrm{d}m^R/\mathrm{d}t)$	evaporation driven rates of miniaturization of virulent
$\boldsymbol{D}$	material derivative	$(\mathrm{d}i^R/\mathrm{d}t)$	rate of occurrence of confirmed cases
p_f	air pressure	$\boldsymbol{m}$	evaporation rate
μ_f	dynamic viscosity of air	$\boldsymbol{i}$	number of confirmed cases
ρ_f	density of air	$\boldsymbol{M_L}$	molecular weight of water
$\mathbf{g}$	acceleration due to gravity	$\boldsymbol{\rho_L}$	density of water
m_d	mass of the droplet	$\boldsymbol{T}$	average absolute temperature
$\mathbf{F}_d^D$	drag force	$\boldsymbol{D_{v,f}}$	average diffusion coefficient for vapor molecules at T
$\mathbf{F}_d^g$	gravitational force	$\boldsymbol{R}$	gas constant
ρ_d	density of droplet	$\boldsymbol{\Delta p}$	difference between the vapor pressure near d and that in the ambient atmosphere
$\boldsymbol{Sc}$	Schmidt number	$\boldsymbol{Re}$	Reynolds number

SYNOPSIS

Nanobiosensors Targeting Affordable Detection of Biomarkers and Pathogens: Experimental and Computational Outlook

I. INTRODUCTION

The United Nations (UN) has recently established Sustainable Development Goals (SDGs) 2030 to address global challenges and ensuring better healthcare, social inclusion, and environmental sustainability by 2030[1]. These goals aim to ensure the well-being and healthy lives of people of all ages. Simultaneously, the World Health Organization has set a "triple billion" target[2], focusing on addressing disorders,[3-5] diseases,[6-8] and disabilities.[9,10] Despite the task actions set by UN, as a result of rapid mutations of pathogens,[11-14] several new diseases are frequently appearing in several corners of the globe, and sometimes severity reaches an extent where these can effect mass population across the entire world. One such catastrophe is the COVID-19 pandemic, which has severely affected people and economy globally, since the inception of the disease to the present day. Thus, the focus is not only in the direction of mitigating the existing problems in a much simpler manner but also to innovate around the new problems to provide affordable health solution.

One can classify health problems based on internal malfunctioning of the body, or due to the invasion of foreign pathogens, like bacteria,[15] viruses,[16] fungus,[17] protozoa,[18] and among others. The human body carries out complex biochemical breakdowns of materials, like carbohydrate, protein, and fat that is consumed in the form of food. Biochemical breakdown of foods involves a series of more complicated reactions exploiting biomolecules like enzymes, hormones, vitamins, minerals, essential metals, water, DNA, RNA, among others. Malfunctioning of any of the organs can lead to many disorders like abnormality of glucose in the blood,[19] abnormal lipid profiles,[20] abnormal bone calcium density,[21] hormonal imbalance[22] and many more. All these changes lead to some of the health issues and sometimes the severity can be life threatening. The influence of foreign pathogens into the body can have multilevel seriousness. Bacterial infections like strep throat, pneumococcal disease, whooping cough, impetigo, short term urinary tract infections and viral infections including common cold, influenza flu, sinusitis, cold sores, chickenpox are a few common maladies that are innocuous and are experienced in day–to–day life which could be easily avoided with hygienic lifestyle. However, pathogenic infections could be highly fatal like tuberculosis, pneumonia, sepsis,

COVID–19, HIV/AIDS, ebola viral infection, rabies, meningitis, herpes which require preemptive diagnosis and expeditious treatment.

Early recognition of any unhealthy condition can prevent communication and spread of diseases. Thus, identification of any infirmity is one of the prime targets for any health concern. The major focus was paid by the researchers, technologists, and medical practitioners over the last century to invent numerous devices and protocols for the detection and quantification of multiple physiological and psychological mal conditions. With the progress in time and invent of new technologies the diagnosis protocol has been revolutionized. Besides, diagnostic tests that are done in pathological laboratories, there are numerous point-of-care testing (POCT) devices[23-27] available for the timely detection of poor health. Commercially available test kits for COVID-19, pregnancy, glucose monitoring, HIV, malaria, ovulation prediction, hemoglobin measurement, hepatitis C, drug detection kits are a few adeptly executed examples.

All those POCT devices which are marketed and are being developed at the research level utilize colorimetric,[28-32] electrochemical,[33-37] resistive,[38,39] capacitive[40-42] and mechanical change based methods as detection principles. Of late, people started single-molecule/cell[43,44] level and microchannel based detection for various unhealthy conditions which are mostly based on specific enzymatic,[45,46] aptasensing,[47,48] or antigen antibody[49-51] based reactions. In a nutshell, an ample amount of literature is readily available for pathological quantification using lab-based techniques. In the recent past, due to the advent of nanotechnology and microfluidics, attempts are being made to miniaturize the existing diagnostic technologies targeting cost minimization and instant hassle-free quantification.

With the changing lifestyle, the demand for POCT devices for early, accurate and real time measurement is on the rise. Also, the personal care sector still needs many POCT devices to carry out a host of urine and blood tests at home or primary health care centers. This thesis proposes to deliver a few POCT prototypes which can be used as a personal care device or can be set up in primary health care centers. The proposed objectives contain the detection of inherent health issues along with diseases caused by external pathogens. The pointwise objectives of this thesis are as follow,

- Chapter 2: Non-invasive Point–of–Care Nanobiosensing of Cervical Cancer as an Auxiliary to Pap-Smear Test
- Chapter 3: Point-of-Care Biosensing of UTI Employing Optoplasmonic Surfaces Embedded with Metal Nanotwins

- Chapter 4: Quantification of Cholesterol and Tri–Glycerides Employing SERS of Silver Shelled Gold Nanorods
- Chapter 5: Pathways to Community Transmission Due to Rapid Evaporation of Respiratory Virulets

The details of the thesis objectives are provided in the following four chapters. A brief summary of the dissertation along with the prospective scope of the works are provided at the end of the fifth chapter.

II. TECHNICAL CHAPTERS

II.1. Chapter 2: Non-invasive Point–of–Care Nanobiosensing of Cervical Cancer as an Auxiliary to Pap–Smear Test

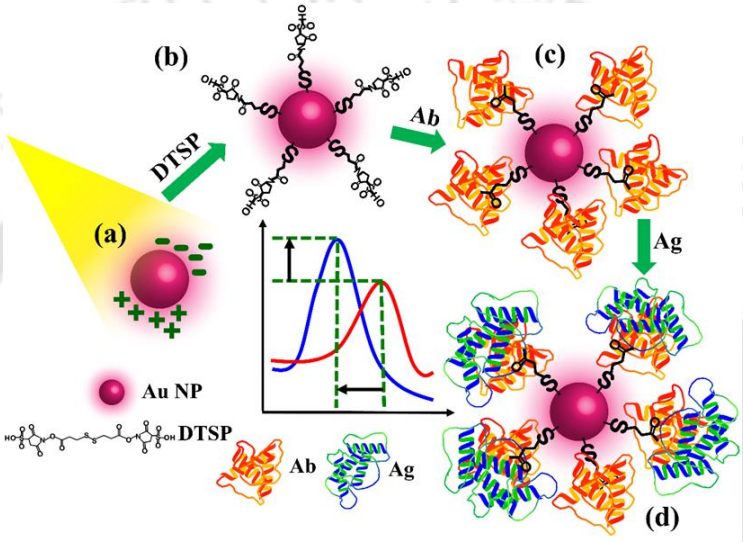

Figure 1: Schematically shows the detection methodology for cervical cancer specific antigen from urine sample. Image (a) represents the pristine Au NPs. Image (b) denotes the 3,3'–dithiodipropionic–acid–di(n–hydroxy–succinimide–ester) (DTSP) attached to Au NPs. Image (c) portrays the attachment of Ab on top of DTSP linked to Au NPs. Image (d) shows the final attachment of the selective protein-NCB-Ag on the surface of Ab immobilized DTSP linked Au NPs.

A potential cancer antigen (Ag), Protein–Phosphatase–1–gamma–2 (PP1ϒ2) with a restricted expression in testis and sperms has been identified as a potential biomarker specific to cervical cancer (CaCx). Detection of this cancer biomarker antigen (NCB–Ag) in human urine opens up the possibility of non-invasive detection of CaCx to supplement the dreaded and invasive Pap–smear test. A colorimetric response of an assembly of gold nanoparticles (Au NPs) has been employed for the quantitative, non–invasive, and point–of–care–testing (POCT) of CaCx in the urine. In order to fabricate the immunosensor, Au NPs of sizes ~5–20 nm have been chemically modified with a linker, 3,3'–dithiodipropionic–acid–di(n–hydroxy–succinimide–ester) (DTSP) to attach the antibody (Ab) specific to the NCB–Ag. Interestingly, the addition of Ag to the composite of Ab–DTSP–Au NPs leads to a significant hypsochromic

shift due to localized surface plasmon resonance (LSPR) phenomenon, which originates from the specific epitope–paratope interaction between the NCB–Ag and Ab–DTSP–Au NPs. The variations in the absorbance and wavelength shift during such attachments of different concentrations of NCB–Ag on the Ab–DTSP–Au NPs composite have been employed as a calibration to identify NCB-Ag in human urine. An in-house prototype has been assembled by integrating a light emitting diode (LED) of a narrow range wavelength in one side of a cuvette in which the reaction has been performed while a sensitive photodetector to the other side to transduce the transmitted signal associated with the loading of NCB–Ag in the Ab–DTSP–Au NPs composite. The proposed immunosensing platform has been tested against other standard proteins to ensure non–interference alongside proving the proof for specificity of the NCB detection.

II.2. Chapter 3: Point–of–Care Biosensing of UTI Employing Optoplasmonic Surfaces Embedded with Metal Nanotwins

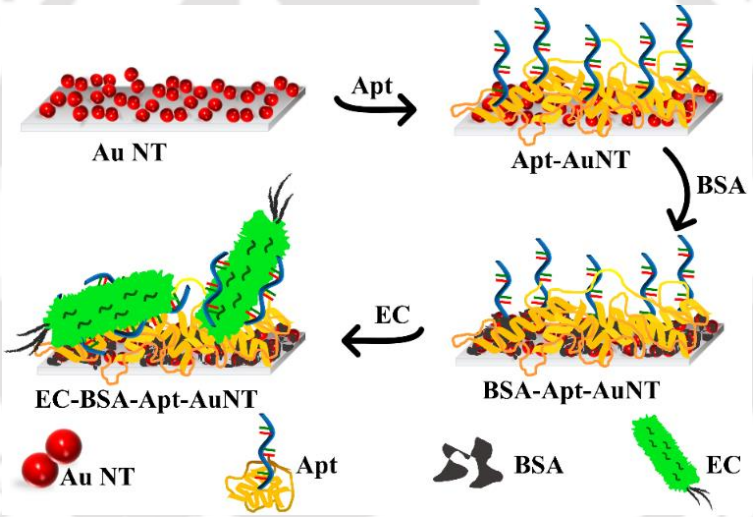

Figure 2: Schematic showing the preparation of plasmonic nanotwin glass substrates for the detection of Urinary Tract Infection causing *Escherichia Coli* bacteria. For this, the *Escherichia Coli* specific aptamer is immobilized on the gold nanotwin substrate and is then allowed to interact with *Escherichia Coli* present in urine sample which attaches with the BSA–Apt–AuNT coated glass substrates.

In this chapter, we report the synthesis of gold nanotwins (Au NTs) on a solid and transparent glass substrate which in turn has been employed for the selective optoplasmonic detection of *Escherichia coli* (EC) bacteria in human urine for the point-of-care diagnosis of urinary tract infection (UTI). As compared to the single nanoparticle system (Au NPs), the Au NTs show an enriched localized surface plasmon resonance (LSPR) due to the enhancement of the electric field under an electromagnetic irradiation, e.g., photon, which helps in improving the limits of detection. For this purpose, initially a simple glass surface has been coated with Au NPs, with the help of the linker 3–aminopropyl–triethoxysilane – APTES. The surface has

further been linked with another Au NP with the help of 1, 10-alkane-dithiol linker with two thiol ends, which eventually leads to the development of the optoplasmonic surface with Au NTs and enhanced LSPR response. Subsequently, EC specific aptamer has been chemically immobilized on the surface of Au NTs with the blocking of free sites via bovine serum albumin (BSA).

Remarkably, the Raman spectroscopy unfolds a seven-fold increase in the peak intensities with the Au NTs on the glass surface as compared to the surface coated with isolated Au NPs. The enhancement in LSPR response of glass substrates coated with Au NTs and EC specific aptamer has been further utilized for the selective and sensitive detection of UTI. The results have been verified with the help of UV-Visible spectroscopy to establish the utility of the proposed sensing methodology. An extensive interference study with other bacterial species unveils the selectivity and specificity of the proposed optoplasmonic sensors towards EC with a detection range of 5×10^3 to 10^7 CFU/mL. Intuitively, the method is more versatile in a sense that the sensor can be made specific to any other pathogens by simply changing the design of the aptamer. Finally, a low-cost, portable and point-of-care optoplasmonic transduction set up is designed with a laser light illumination source, a sample holder, and a sensitive photo-detector for the detection of UTI in human urine.

II.3. Chapter 4: Quantification of Cholesterol and Tri–Glycerides Employing SERS of Silver shelled Gold Nanorods

In this chapter, cholesterol (Cho) and tri-glyceride (TG) has been estimated employing excellent Surface Enhanced Raman Spectroscopy (SERS) of silver shelled gold nanoparticles (Ag–Au NRs). Briefly, gold nanorod (Au NRs) was synthesized employing seed-growth method followed by creating a shell of silver via reduction of $AgNO_3$ onto synthesized gold nanorod. The silver shelled gold nanorod shows augmented Surface Enhanced Raman Spectroscopy (SERS) property owing to spectrum coupling between silver and gold. The enhanced SERS property was utilized for selective quantification of Cho and TG. For capturing the SERS enhancement two specific Raman reporters, DTNB and 4ATP, were chemically attached on the surface of Ag–Au NRs to synthesize SERS nanoprobes, before the attachment of the bioreceptors –cholesterol oxidase (ChOx) and lipase (Lp). ChOx–DTNB–Ag–Au NRs and Lp–4ATP–Ag–Au NRs were used for the quantification of various concentrations of Cho and TG. Solution based liquid Raman spectroscopic study was performed to mitigate zone specific Raman effect that is common for solid substrates. The change in SERS signals of the specific Raman reporters were systematically recorded in reference to the blank sample. Further, the Raman spectrum was utilized for the preparing the calibration curve for both the

Cho and TG. Additionally, various interference studies taking ascorbic acid, glucose, sodium ion, and potassium ion were performed to justify excellent selectivity of the proposed method.

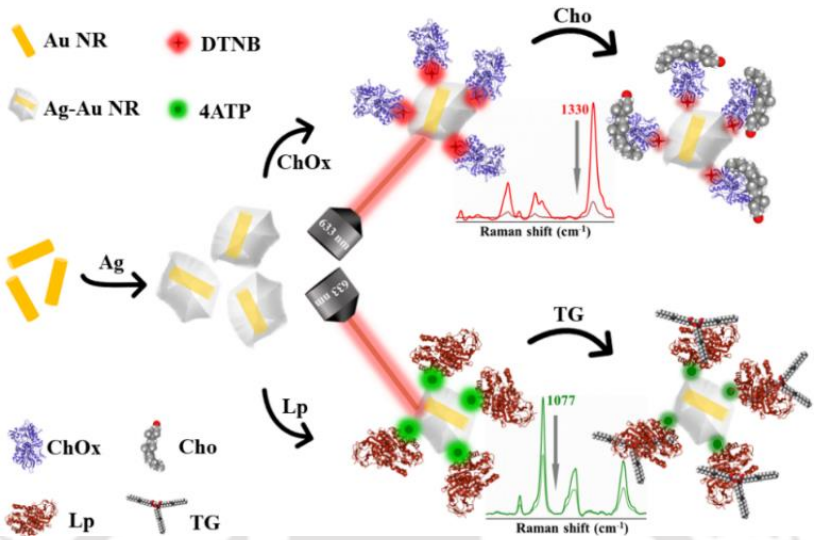

Figure 3: Schematic showing the detection methodology of Cho and TG. At first bimetallic nanostructures of Ag-Au NRs was prepared and was immobilized with DTNB/4ATP to prepare SERS nanoprobes. The SERS nanoprobes were then further immobilized with ChOx/Lp respectively which on attachment with Cho/TG caused variation in the SERS spectra that was used to detect various concentration of Cho/TG.

II.4. Chapter 5: Pathways to Community Transmission Due to Rapid Evaporation of Respiratory Virulets

The motions of virus laden respiratory microdroplets – '*virulets*' and their evaporation driven miniaturization in the open air are found to have significant impact on the community transmission of COVID–19 pandemic. In this direction, we simulate the motions of such droplets expelled from nose and/or mouth of a human being deploying the efficacies of computational fluid dynamics. The framework employs the physics for a laminar flow coupled with a droplet tracing model to track the motions of microdroplets while the sneezing or coughing have been emulated employing a time periodic Gaussian velocity distribution function. An analytical model has also been developed to incorporate the influence of temperature (T) and relative humidity (RH) on the rate of evaporation and subsequent miniaturization of the on–the–fly *virulets*. Subsequently, the study considers virulets of different size range to follow the motions and perform an infectivity analysis. In that attempt, a force field analysis has been included considering the gravity, drag, and inertial force to unleash some of the finer features of virulet trajectories leading to the droplet and airborne transmissions of the virus. The study elucidates that virulets of lower size range (1–50 μm) tend to form a bioaerosol and facilitate an airborne transmission with a very less viral load while the virulets of significantly larger dimensions (300–500 μm) are more prone to droplet

transmission as they settle faster under gravity towards the surfaces. Importantly, the rapidly evaporating virulets of intermediate size range (60–100 µm) with considerable viral loading are found to be more prone to the airborne transmission owing to on–the–fly bioaerosol formation. The study unveils the potency of such droplets to become airborne under suitable *T* and *RH*. Subsequently, the rate of evaporation and miniaturization of such droplets in different cities across the globe with the variations in the *T* and *RH* have been mapped to the extent of community spreading of COVID–19 during first and second waves. The results corroborate that these parameters can be faithfully employed to predict the future waves of the pandemic.

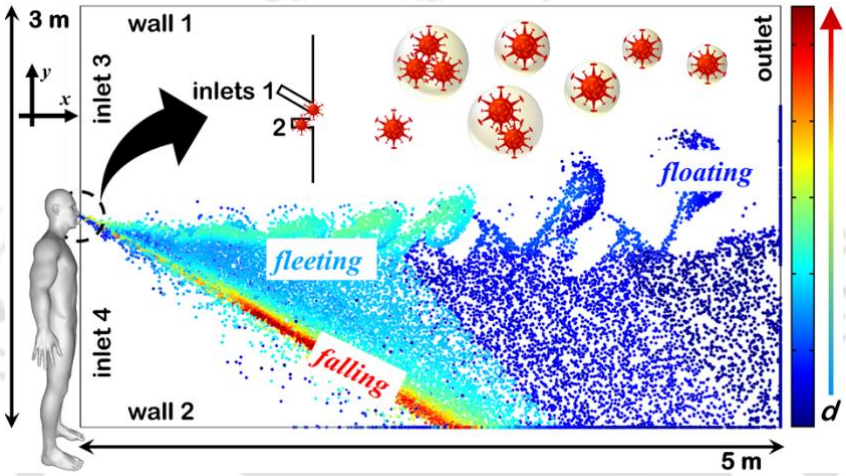

Figure 4: Schematic showing the 2D geometry with the dimensions and axes considered for the simulation study. The nose and mouth openings are indicated as inlets 1 and 2, respectively while inlets 3 and 4 show the open-air inlets. The walls 1 and 2, at the top and bottom show the upper boundary and ground of the solution space, respectively while the outlet in the geometry is shown towards the right side. The respiratory virulets of varied diameter *d* have been indicated by different color code. The inset schematically shows the SARS–CoV–2 loaded respiratory droplets expelled from an infected person.

III. Summary and future scopes

Conclusively, the thesis depicts the utilization of unique and excellent properties of plasmonic nanoparticles and nanoparticle assemblies for ultrasensitive and selective quantification of (i) cervical cancer antigen from urine samples (ii) urinary tract infection from urine samples (iii) lipid profile targeting blood plasma samples utilizing LSPR and SERS. Furthermore, the chapter four deciphers the airborne disease transmission mechanism that certainly helps in deciding the steps to mitigate such transmission and the role of environmental factors in the community transmission of airborne diseases like SARS–CoV–2. In designing all the biosensors, the focus is on improving the selectivity of the sensing without compromising with the level of detection and the cost of biosensor design. The thesis successfully shows mitigation of possible interferences during testing of the targeted biomarkers. During the process of biosensor design and sample testing the sources of error and

limitations are also described in the thesis for the benefit of the readers. The work covered in this thesis will lead to the following future scopes,

(i) Possibilities of technology transfer to the relevant group for the deployment of the developed biosensors for improved version of the prototypes.

(ii) Opportunities for collaboration with hospitals, health centers, and the research groups for extending the work for more clinical trials.

(iii) Incorporation of additional functionalities to the developed sensing protocols for further improvement of sensitivity and selectivity based on clinical studies.

(iv) The thesis extends a scope for development of similar portable optoelectronic devices for multiplexed biosensing approaches.

(v) The thesis also provides scope to further miniaturize the device prototypes for the ease of field applications.

(vi) Finally, the thesis can serve as a valuable research resource that may be used by researchers of diverse fields.

Chapter 1

INTRODUCTION

Health stands as an essential concern demanding the utmost attention and care for the perpetuity and well-being of the mankind. Basic healthcare facilities are the fundamental necessity of the humanity worldwide. Unfortunately, even in the era of modern technologies, health continues to be undervalued and neglected on a global scale leading to uneven access to healthcare resources and medical solutions. In pursuit of bridging the disparity, World Health Organization (WHO)[2] launched "triple billion" initiative for 2019–2023 ensuring better health and well-being, protection to health emergencies, and healthier living conditions. Also, The United Nations (UN) recently established Sustainable Development Goals (SDGs) 2030[52] to address global challenges and ensuring better healthcare, social inclusion, and environmental sustainability by 2030. Similarly, under non-communicable diseases (NCDs) initiative[53], WHO emphasizes the prevention and control of premature mortality due to non-infectious diseases like cardiovascular diseases, cancer, chronic respiratory diseases, and diabetes. These frameworks empower structured, coordinated and collaborative approaches towards improved global health and resilient health systems.

However, novel diseases are being witnessed globally as a result of rapid mutations of pathogens[54-56], and sometimes severity reaches an extent where these can effect mass population across the entire world. One such catastrophe is the COVID–19 pandemic, which has severely affected the people and the economy globally, since its inception to present day. Thus, the focus should not only in the direction of mitigating the existing problems in a much simpler manner but also to innovate around the new possibilities to provide affordable health solution. As per medical terminology, healthcare facilities are classified into three categories[57-59]; (i) primary, (ii) secondary and (iii) tertiary healthcare. Primary healthcare concerns about primary patient and doctor interaction to carry out basic health checkup for identifying medical issues[60]. Secondary healthcare relates to thorough diagnostics and detailed body check up to dig into the reasons behind critical health issues[61]. Tertiary healthcare relates to surgeries, blood transfusions, organ transplant or dealing with similar critical issues[62]. It is now evident that when diseases could be effectively treated at the primary care level, a significant number of cases can be prevented from progressing to advanced tertiary stages. This highlights the importance of primary care in the healthcare system.

One can classify health problems based on internal malfunctioning of the body, or due

to the invasion of foreign pathogens, like bacteria[63], viruses[64], fungus[65], protozoa[66], and among others. The human body carries out complex biochemical breakdowns of materials, like carbohydrate, protein, and fat that enter the body in the form of food. Biochemical breakdown of foods involves a series of complicated reactions exploiting biomolecules like enzymes, hormones, vitamins, minerals, and among others. Various biomolecules present in our body are employed to convert food into energy, which is subsequently used to facilitate the physiological functioning of the entire body. As an example, insulin, a biomolecule, plays a crucial role in facilitating the transport of glucose from the bloodstream to individual cells in the body[67,68]. Notably, the production and secretion of insulin are intricately regulated by various essential factors. Abnormal function of either insulin secretion or absorption leads to a malfunction commonly known as diabetes[69]. The human body operates through a complex and interconnected physiological mechanism to ensure its seamless functionality. Dysfunctions within one or multiple body systems can give rise to various pathological conditions, commonly recognized as diseases. Alongside the cited example of glucose malfunctioning there are other issues which leads to diverse diseases that include abnormality of lipid profiles[70], abnormal bone calcium density[71], hormonal imbalance[72], malfunctioning of pancreas[73], and many more. Elevated lipid profile leads to deposition of plaque on blood capillaries leading to high blood pressure[74], low bone condition leads to Osteoporosis[75], hormonal imbalances lead to various types of diseases[76], abnormal enzyme secretion from pancreas leads to pancreatitis[77] to count a few. All the aforementioned physiological issues can be of different severity ranging from curable disease to serious health disorders even leading to death. Similarly, an invasion of foreign toxic proteins or microorganism also leads to various communicable and non-communicable ailments. The seriousness of foreign invasion could be ranging from common cough and cold to deadly diseases like COVID–19, AIDS, hepatitis, dengue, and others[78,79]. Bacterial infections[80,81] like strep throat, pneumococcal disease, whooping cough, impetigo, short term urinary tract infections and viral infections[82,83] including common cold, influenza flu, sinusitis, cold sores, chickenpox are a few common maladies that are innocuous and are experienced in day–to–day life which could be easily avoided with hygienic lifestyle. However, pathogenic infections[84,85] could be highly fatal like tuberculosis, pneumonia, sepsis, COVID-19, HIV/AIDS, ebola viral infection, rabies, meningitis, herpes which require preemptive diagnosis and expeditious treatment. Identification of such diseases are generally done by identifying the foreign protein or the microorganism via some biochemical interaction mechanisms.

Certainly, early recognition of any unhealthy condition can prevent the disease progression, complications, healthcare costs, and outbreaks of pandemics or epidemics. Thus, deciphering any infirmity is one of the prime targets for any health concern. A major focus has been accomplished by the researchers, technologists, and medical practitioners over the last century to invent various devices and protocols for the detection and quantification of multiple physiological and psychological malconditions. With the progress of time and invent of new technologies the diagnosis protocols have revolutionized. Besides, diagnostic tests that are done in pathological laboratories there are numerous point–of–care testing (POCT) devices[86,87] available for the timely detection of poor health. POCT devices are portable diagnostic tools designed for performing medical tests outside the large–scale laboratories with equal precision, lowering turn–over–time, and improving point of patient interaction for better clinical management of disease prognosis[88,89]. As healthcare is approaching more towards patient–centered rather centralized clinics, it is imperative to encourage patient assessment and testing at primary or community health care centers instead of expensive care in secondary and tertiary hospitals[90]. However, large scale installation of analytical laboratories is impractical, both geographically and economically. In this context, POCT devices has proven to be an innovative tool to transform the diagnostic landscape. Commercially available test kits for COVID–19, pregnancy, glucose monitoring, HIV, malaria, ovulation prediction, hemoglobin measurement, hepatitis C, drug detection kits are a few adeptly executed examples[91-93]. According to World Health Organization (WHO) guidelines for sexually transmitted infections (STIs), a POCT should be "ASSURED"[94] – Affordable, Sensitive, Specific, User-friendly, Rapid & Robust, Equipment–free, and Delivered to the end users. Lately, the marketed POCT devices are referenced as (i) "non-professional testing" like glucose monitoring & pregnancy testing, and (ii) "professional testing" that includes critical care, and diagnosis of infectious diseases, cardiac markers, diabetes, lipids, coagulation, and hematology[95]. As per Future Market Insight (FMI) report, POCT market is valued at US $4.4 billion by 2023 and anticipated to raise by US $11.1 billion by 2033 (https://www.futuremarketinsights.com/reports/point-of-care-molecular-diagnostics-market). Therefore, focusing on advancements in various POCT technologies is not only strategically advantageous but is highly sought for its increasing demand targeting user–friendliness, rapidity, high sensitivity, and specificity.

POCT devices could be broadly categorized into – (i) small handheld/portable POCT devices and (ii) larger bench–top POCT Devices[95]. Small handheld/portable POCT Devices are the small devices like dipsticks or small cartridge devices that are basically used by the

patients themselves or by any healthcare professional at patient's site, for e.g., Siemens Multistix for urinalysis by Siemens Healthineers, immunoassays such as Preganews by Mankind Pharma Limited or Accu–check by Roche Diabetes Care, i–STAT by Abbott, Epoc by Siemens Healthineers. However, larger bench–top POCT devices are miniaturized and portable versions of pathological laboratory's analytical instruments. The size and complexity of these devices are reduced so that it could be installed at any geographic location, could be relocated and could be operated by any non–laboratory trained staff, for e.g., an auto–analyzer detecting a pool of biomarkers such as Siemens DCA (Direct Connect to Analyzer) by Siemens Healthineers, Abaxis Piccolo Xpress, LABGEO by Samsung Corporation, PIMA by Alere. Design and fabrication of POCT devices demands high sensitivity, miniaturization of the device, and integration of digital electronics alongside advanced graphical user interface for recording patient data. Excellent progress in semiconductor physics, digital electronics, and fabrication technologies have made possible the miniaturization of point of care testing devices easier than before. Over a period of last few decades, scientists, technologists, and engineers came together to develop different POCT devices that include lab-on a chip device[96,97], immunochromatographic assays[98,99], lateral flow assays[100,101], Micro-Electro-Mechanical Systems (MEMs)[102], smartphone integrated optical[103,104] biosensors, medical image analysis based digital classifiers[105], artificial intelligence and machine learning integrated smart biosensors[106,107] and more. Currently, POCT integrated with Internet of Medical things (IoMT)[108,109] have gained much importance owing to incorporation of wireless connection with healthcare professionals for rapid analysis and validation of results for personalized patient data management.

The principle of detection of POCT devices could be classified into techniques such as–colorimetric[110,111], electrochemical[112,113], resistive[114,115], capacitive[116,117] or mechanical change[118,119] based approaches. Optical biosensors are one of the major forerunners in the field of POCT device design and manufacturing. Explicitly, optical biosensors are mostly focused on assessment of biochemical reactions which are sensitive, selective, and capable of producing a variation in color even with lower concentrations of target analyte. Utilizing color development reactions, diagnostic tools like various colorimetric assays[110,120], spectroscopy based detection[121,122], Enzyme–Linked Immunosorbent Assay (ELISA)[123] have been developed chronologically. In the last two–decades, optical biosensors based on plasmonic shifts have been in use leaps and bound[47,124]. Plasmon is a property which is observed in a few specific metallic nanostructures including gold, silver, and platinum. In general, in the presence of light irradiation, the surface electrons of these metal

nanostructures form a dipole which oscillates with the photons[125]. The light irradiation onto the thin metal surface excites surface electrons to form plasmonic wave which propagates horizontally across the metal surface and this phenomenon is known as Surface Plasmon Resonance (SPR)[126,127]. The surface plasmon resonance occurs at a specific angle of light incidence which is sensitive to the dielectric constant of the materials surrounding metal surface. The tunability of SPR with dielectric property of material has been utilized extensively for designing biosensors[128,129]. Briefly, a capture molecule like antibody, enzyme, aptamer, RNA, DNA fragments are attached on to the thin plasmonic metal surface and the interaction of these capture molecules with their complementary targets lead to shift of SPR signal and the same forms the basis of sensing. A chronological development in the field of such SPR biosensors are observed in the form of prism coupled SPR biosensors[130,131], waveguide coupled SPR biosensors[132], optical fiber coupled SPR biosensor[133], side polished fiber coupling photonic crystal[134], grating coupled SPR biosensors[135] and long-range and short-range SPR biosensors[136].

It is to be noted that SPR takes place on a flat thin metal surface. However, metal nanoparticles like gold, silver, and platinum show a slightly different property than SPR. The photonic excitation onto nanoparticles also lead to occurrence of plasmon however this plasmon remain confined locally around the nanoparticles and hence termed as Localized Surface Plasmon Resonance (LSPR)[137,138]. The LSPR is also sensitive to the change of local dielectric constants and hence this property is hence utilized for the development of enzymatic sensors, immunosensors, aptasensors and many more. In general, absorption property and plasmonic shift (change of resonance wavelength) are generally used for the designing of biosensors[139]. An antigen-antibody, enzyme-substrate, aptamer-target interaction onto the nanoparticle surface leads to change in both absorption and wavelength shift of plasmonic nanoparticle. With further development of nanoplasmonic sensors, people fabricated nanoparticles of various shape like rods, prism, star, needle, and others which have enhanced plasmonic property compared to spherical nanoparticles and hence those enhanced plasmonic response show better resolution of sensing[140-142]. The propensity for further plasmonic enhancement instigated inventions of core shell nanostructures[143], porous nanostructures[144], hybrid nanostructures[145] which also find significant contribution in nanoplasmonic sensor development. A further step towards betterment initiated the concept of plasmonic overlaps and creation of hotspot in plasmonic dimers[146], plasmonic nanostructure arrays[147], and plasmonic nanohole arrays[148] for next generation and precise biosensor design. Apart from utilization of plasmonic biosensors, gold nanoparticle–based

aggregation and segregation technique[149] catalyzed by the target molecule has also been shown as a potential pathway for biosensor design. With further advancement of technology optical detection was escalated in the form of labelled fluorescence detection[150], Tip enhanced Surface Raman Spectroscopy (TERS)[151], Spatially offset Raman Spectroscopy (SORS)[152], Surface Enhanced Resonance Raman Spectroscopy (SERRS)[153], Surface Enhanced Infrared Spectroscopy (SEIRS)[154], Periodic Surface Lattice Resonance (PSLR)[155], interferometers[156], photonic crystals[157] and more. In a nutshell, current research is dedicated to improving disease identification and quantification utilizing advanced technologies.

With the changing lifestyle, the demand for POCT devices for early, accurate and real time measurement is on the rise. Also, the personal care sector needs many POCT devices to carry out a host of urine and blood tests at home or primary health care centers. This thesis proposes to deliver a few POCT prototypes which can be used as a personal care device or can be set up in primary health care centers. The proposed objectives contain the detection of inherent health issues along with diseases caused by external pathogens. The details of the thesis objectives are provided in the following four chapters. A summary of the dissertation along with the prospective scope of the works are provided at the end in fifth chapter followed by the list of publications. The pointwise objectives of this thesis are as follow,

(i) Chapter 2: Non-invasive Point–of–Care Nanobiosensing of Cervical Cancer as an Auxiliary to Pap–Smear Test

The chapter delves into the development of a methodology for non-invasive screening of cervical cancer utilizing urine sample analysis. The conventional cervical cancer diagnostic techniques reported so far are highly invasive that necessitates scrapping of cervical cells. In the present chapter, we identified a urinary protein, Protein Phosphatase-1-Gamma-2 (PP1Ɣ2), which we claim as a potential biomarker for the detection of the cervical cancer. Later, a gold nanoparticle based immunosensing methodology was developed employing PP1Ɣ2 antibody immobilization. Further, a 3D printed point of care testing device prototype was fabricated targeting on-site screening of the disease.

(ii) Chapter 3: Point–of–Care Biosensing of UTI Employing Optoplasmonic Surfaces Embedded with Metal Nanotwins

This chapter aimed at enhancing the selectivity of EC bacteria biosensing utilizing plasmon enhanced Au NTs. The precise quantification of EC in urine sample predicts different stages

of UTI. The chapter specifically focuses on creating a bed of aptamer immobilized plasmonic hotspots on glass substrate to enable enhanced plasmonic signal for the efficient detection of EC. Interference studies with other bacteria showed excellent selectivity of the method.

(iii) Chapter 4: Quantification of Cholesterol and Tri–Glycerides Employing SERS of Silver Shelled Gold Nanorods

The present chapter focuses on the enzymatic detection of Cho and TG employing enhanced SERS properties of plasmonic bimetallic nanostructures Ag-Au NRs. The nanostructures showed significant enhancement in the plasmonic property as compared to the pristine Au NRs. Herein, Ag-Au NRs were synthesized and immobilized with ChOx and Lp enzymes separately to record the change in SERS intensity and shift in wavelength owing to the interaction of the ChOx and Lp with Cho and TG, respectively. The developed sensing platform was also validated against different interfering agents mostly found in the human blood, which showed a good selectivity for the biomolecule of interest.

(iv) Chapter 5: Pathways to Community Transmission Due to Rapid Evaporation of Respiratory Virulets

This chapter models the possibilities of community transmission of COVID-19 via sneezing and coughing of the SARS-CoV-2 infected patient. A CFD model has been created using COMSOL Multiphysics to look into the droplet trajectories and thereby disease transmissions during sneezing and coughing. Different realistic case studies, such as transmission in calm air, various air breeze, effect of virulet size distributions, effect of evaporation of droplets owing to various geographic temperature and relative humidity conditions have been studied to emulate the most accurate picture of the disease transmission. Additionally, detailed kinetic studies for the droplet evaporation has been introduced and the results obtained are mapped with COVID-19 transmission of different cities across the globe to validate the model.

(v) Chapter 6: Summary and Future scopes

भारतीय प्रौद्योगिकी संस्थान गुवाहाटी
Indian Institute of Technology Guwahati

Chapter 2

Non-invasive Point–of–Care Nanobiosensing of Cervical Cancer as an Auxiliary to Pap-Smear Test

ABSTRACT

A potential cancer antigen (Ag), Protein–Phosphatase–1–gamma–2 (PP1ϒ2) with a restricted expression in testis and sperms has been identified as a biomarker specific to cervical cancer (CaCx). Detection of this cancer biomarker antigen (NCB–Ag) in human urine opens up the possibility of non-invasive detection of CaCx to supplement the dreaded and invasive Pap-smear test. A colorimetric response of an assembly of gold nanoparticles (Au NPs) has been employed for the quantitative, non-invasive, and point-of-care-testing (POCT) of CaCx in the urine. In order to fabricate the immunosensor, Au NPs of sizes ~ 5–20 nm have been chemically modified with a linker, 3,3'-di-thio-di-propionic-acid-di(n-hydroxy-succinimide-ester) (DTSP) to attach the antibody (Ab) specific to the NCB–Ag. Interestingly, the addition of Ag to the composite of Ab–DTSP–Au NPs leads to a significant hypsochromic shift due to localized surface plasmon resonance (LSPR) phenomenon, which originates from the specific epitope-paratope interaction between the NCB–Ag and Ab–DTSP–Au NPs. The variations in the absorbance and wavelength shift during such attachments of different concentrations of NCB –Ag on the Ab–DTSP–Au NPs composite have been employed as a calibration to identify NCB–Ag in human urine. An in-house prototype has been assembled by integrating a light emitting diode (LED) of a narrow range wavelength in one side of a cuvette in which the reaction has been performed while a sensitive photodetector to the other side to transduce the transmitted signal associated with the loading of NCB–Ag in the Ab–DTSP–Au NPs composite. The proposed immunosensing platform has been tested against other standard proteins to ensure non–interference alongside proving the proof–for–specificity of the NCB detection.

2.1. Introduction

Cervical cancer (CaCx) is presently one the most common forms of carcinoma among women. Nearly 2.8 billion females aged ~15 years or older are at risk of developing this dreaded disease.[158] Every year, nearly 5,28,000 women are diagnosed with CaCx and 2,66,000 succumb to death.[158] Pathologically, CaCx appears at the squamocolumnar junction (SCJ) of the cervix, which undergoes continuous metaplasia during puberty, sexual life, and pregnancy of a female.[159] The females undergoing a peak metaplastic change between 18–30 years of age are at high risk of developing the CaCx through the viral infections of the Human Papilloma Virus (HPV).[159] The risk of HPV infection intensifies with early marriage, polyamory, multiparity, smoking, poor genital health, a diet deficient in antioxidants, long-term use of contraceptives, and lack of awareness, among others.[159] The HPV statistics of 2018[160] suggest that CaCx is more prevalent in the areas with low-resource locales, e.g., Sub-Saharan Africa, South-Central Asia, Central and South America, and Central-Eastern Europe. The National Cancer Registry Program (NCRP) data indicate that, in India, after breast cancer, CaCx is the second most common cancer in females. The women aged between 15–44 years account for ~ 6–29% of the cancer cases specific to females while 50–59 year carry ~ 27.37% of all CaCx cases.[159]

Interestingly, among the all available strains, HPV 16 and HPV 18 are largely responsible for the development of CaCx.[159] Unfortunately, the disease does not express any physical alterations at the early stages. The patient remains rather asymptomatic unless a systematic and regular screening of cervix health is done.[159] Importantly, the currently available cervical screening test is a painful and invasive procedure, known as Pap-smear or Papanicolaou test, in which the precancerous and/or cancerous tissues at the cervix are scraped out to identify the abnormal lesion through colposcopic examination, biopsy, and histological confirmation.[159] In this regard, ThinPrep imaging,[159] portable or multispectral colposcopy,[159] and HPV detection in urine[161] or blood plasma[161] are some of the other alternative methods. There are a number of techniques currently available for the screening of CaCx like Papanicolaou smear[159,162,163] Pelvic examination[159,164,165], Colposcopy[159,166,167], Liquid-based cytology[159,162,163], HPV testing[159,168,169], Polar probe[159], Laser-induced fluorescence[159,170], Visual inspection by applying Lugol's Iodine (VILI) or acetic acid (VIA)[159,171,172], Speculoscopy[159,173], Cervicography[159,174,175], and Neuromedical systems[159]. However, such methods are in general invasive and tedious for the patients during the examination, involve bulky and costly instruments for detection, and require trained healthcare professionals for analysis. Clearly, the need of the hour is a non-invasive, point-of-care (POC), user-friendly, and cost-effective

solution for the detection of CaCx. In this direction, the present manuscript focuses on the POC detection of a novel protein biomarker antigen (NCB-Ag) Protein-Phosphatase-1-gamma-2 (PP1ϒ2) specific to CaCx, expressed in the urine sample of a patient, after integrating the efficacies of state-of-art nanoscience and nanobiotechnology.

In the past few decades, a rapid advancement in the morphological and materials characterization of nanoscale objects, supplemented by the improvement in the efficacy of the separation and purification of proteins, has opened up a number of avenues in the domain of nanobiotechnology. For example, the prior-art suggests that the protein biomarkers are of significant medical importance in the diagnosis and monitoring of the health of diverse human organs,[176] malignancy of tissues,[177] antigen attacks like bacteria[178] or viral[178] infections, among others. Rapid progress in the development of bench-top analytical techniques like Western-Blot (WB),[179] Enzyme-Linked-Immunosorbent-Assay (ELISA),[179] gel-electrophoresis (GE),[180] and Polymerase Chain Reaction (PCR)[179] have also enabled the laboratory scale identification of disease specific protein markers in various body fluids, such as sebum,[181] serum,[182] urine,[182] tear,[183] swab,[184] soft tissues,[185] or cervicovaginal fluids.[186] For example, the level of total protein[187] or albumin in urine or blood serum has now been employed for the early diagnosis of Chronic Kidney Dysfunction (CKD), proteinuria, and micro or microalbuminuria, among others. Further, the levels of β-2-microglobulin, TGF-β, or TNF-α in urine or blood serum are well-known protein markers for predicting the stages of diabetic retinopathy[188] or cancers. It is now well established that, although such protein markers are found in a much larger quantity in the blood serum, they are either non-existent or minimal in the urine of a healthy human. Thus, detection of protein markers in urine samples has been a serious challenge over the years. Importantly, as of now, there is no work reported on the detection of a definite protein biomarker specific to CaCx in a urine sample.

On the other hand, of late the point-of-care-testing (POCT) devices have gained considerable attention because of their crucial utilities in healthcare,[189] environmental monitoring,[190] and real time surveillance. The POCT devices are found to play a vital role in the detection and monitoring of routine health irregularities,[191] chronic diseases,[6,8] or asymptomatic disorders.[3,4] From the engineering point of view, the POCT devices employ diverse chemical and electronic principles for the detection of disease specific biomarkers. They include resistive,[39] electrochemical,[33] colorimetric,[32] and capacitive[40] techniques. Of late, a wide range of POCT devices has been designed and developed wherein the resistive,[192] electrochemical,[33] surface acoustic wave (SAW),[193] field effect transistor (FET),[194] CMOS,[195] electrical double layer (EDL),[196] optoelectronic,[197] microelectromechanical systems

(MEMS),[198] or immunosensing[51] principles have been utilized for the recognition of diverse biomarkers present in different body fluids. The glucometer,[199] pregnancy kit,[200] weighing machine, or blood pressure monitoring device[201] are commercially successful.

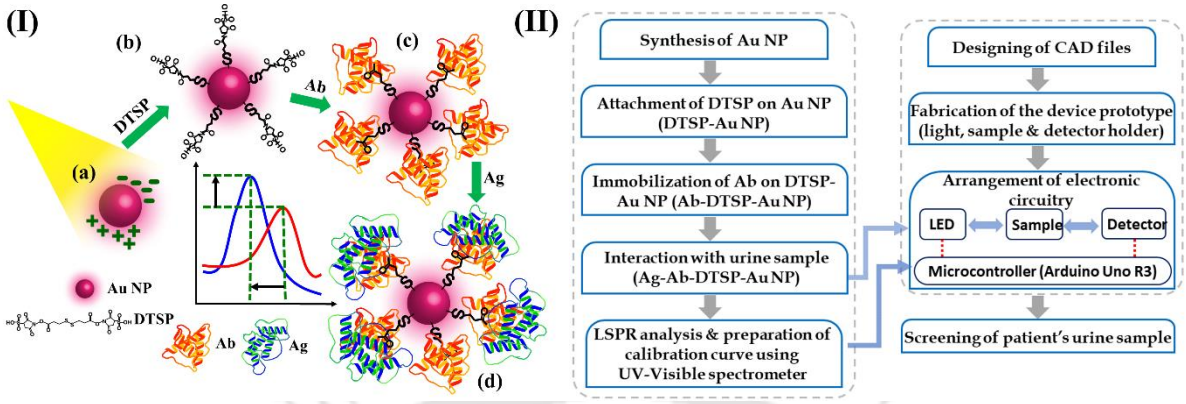

Figure 2.1: (I) Shows different stages of biomolecule attachment on the surface of Au NPs. Image (a) represents the pristine Au NPs. Image (b) denotes the 3,3'–dithio–dipropionic–acid–di(n–hydroxy–succinimide–ester) (DTSP) attached to Au NPs. Image (c) portrays the attachment of Ab on top of DTSP linked to Au NPs. Image (d) shows the final attachment of the selective protein-NCB-Ag on the surface of Ab immobilized DTSP linked Au NPs. (II) Shows the flow chart depicting the fabrication/testing process involved in the present work.

In view of this background, a proof–of–concept POCT prototype has been developed for the detection of a CaCx specific protein marker in human urine. Since the concentration of such proteins is rather meagre in urine, we employ a highly sensitive localized surface plasmon resonance (LSPR) based immunosensing[202] method for the qualitative, reliable, and specific detection of the biomarker. **Figure 2.1** schematically shows the proposed principle employed for the non-invasive POCT of CaCx. The Ab is initially attached to the plasmonic Au NPs through a DTSP linker to form a composite Ab–DTSP–Au NPs,[203] which undergoes a plasmonic shift after the interaction with NCB–Ag in the urine.[204] The sensor is specific because the 'paratope' in the composite Ab–DTSP–Au NPs binds selectively to 'epitope' in NCB–Ag following a specific lock and key mechanism. The LSPR signal from Au NPs is found to be sensitive to such an interaction owing to a change in the electronic/optical properties at Au NPs–electrolyte (metal–dielectric) interface.[205] Such variation in wavelength shift is initially measured by UV–Visible spectroscopic analysis to prepare a calibration for a known amount of NCB–Ag in the urine. Following this, a proof–of–concept POCT prototype has been developed wherein a light source and a photodiode have been integrated into a cuvette in a transmission mode before tracking the variations in the intensity and wavelength shift of the Ab–DTSP–Au NPs composite during the binding of NCB–Ag with Ab–DTSP–Au NPs. In a nutshell, utilizing the efficacies of nanoscale science and technology, the study elucidates

economic and non-invasive urine based POC detection of CaCx, which may not only enable early screening but also help in regular monitoring of the disease at the patient site.

2.2. Materials and methods

2.2.1. Materials

Analytical grade tetrachloroauric acid ($HAuCl_4$), 3,3'-dithiodipropionic acid di(N-hydroxysuccinimide ester) (DTSP), and sodium borohydride ($NaBH_4$), bovine serum albumin (BSA), tween 20, hydrochloric acid (HCl), sodium hydroxide (NaOH), di-sodium hydrogen phosphate ($Na_2HPO_4.7H_2O$), potassium di-hydrogen phosphate (KH_2PO_4), sodium chloride (NaCl), potassium chloride (KCl), β-mercaptoethanol (BME), horseradish peroxide (HRP) and radio-immunoprecipitation assay buffer (RIPA buffer) were procured from Sigma-Aldrich.

2.2.2 Methods

I. Generation of antibody in rabbit

Synthetic peptide specific to the NCB protein i.e., PP1Ƴ2 was dosed to the female rabbit at an optimized time point to raise the polyclonal antibodies in two female rabbits. Pre-immune sera were collected from these animals. Afterward, these animals were immunized with the first dose of 200 µg of the purified peptide with complete Freund's adjuvant and boosted five times with 100 µg of the same peptide at intervals of 7 days in incomplete Freund's adjuvant. A 500 µL of serum was collected after every two dosages of peptide injection and the complete serum was collected from the final bleed, which was affinity-purified through the same synthetic peptide. The specificity of the affinity-purified Antibody was tested against the 200 ng of this peptide and 50 µg of mouse testis extract.

II. Collection of patient samples

(a) Cervico-vaginal fluid (CVF):

Samples were collected from patients diagnosed with pre-cancerous lesions and cervical cancer. Cervico-vaginal smear was collected through the cyto-brush (Rovers) and made thin smear on clean glass slide followed by immediate fixing of the smear with the Polyethylene glycol (PEG) based fixative, now the cyto-brush is snapped off carefully, and cell scrapings were collected in the 10 mL of 24 % ethanol vial. This entire collection was done from patients regularly visiting King George's Medical University, Lucknow, (U.P) India with requisite ethical permissions and informed consent.

(b) Urine sample:

10–50 mL of midstream urine samples was collected through micturition in a 50 mL sterilized centrifuged tube at any random time point of the day. The samples were directly

placed in a cool box with having frizzed cartridge and transported to the lab under ambient conditions.

(c) Isolation of total RNA from CVF samples

The cyto brush tip was carefully removed from the tubes having 24 % ethanol. Tubes were centrifuged at 8000*g* for 10 min at 25° C to pellet the residual cells and washed with PBS twice. RNA isolation was done through ReliaPrep™ RNA Miniprep Systems (Promega) in RNase free condition following the manufacturer's instructions.

(d) cDNA synthesis and RT-PCR:

The first-strand synthesis of mRNA into cDNA was performed using a Verso cDNA synthesis kit following the manufacturer's protocol. Briefly, 0.5 µg or 1 µg of total RNA was mixed with 2 µL dNTPs and water in the prescribed amount. Heat treatment of RNA/primer mix was done at 65° C for 5 min and then placed on ice for 5 min. Further, 1 µL random hexamer primer, 1 µL RT enhancer, 1 µL Verso enzyme mix (Reverse Transcriptase), and 4 µL of 10 X Verso enzyme buffers were added. Components were mixed and incubated at 42°C for 30 min, followed by enzyme activation by heating it at 95°C for 5 min. The preparation was stored at 4°C for short-term storage or at – 20°C for a long time. About 2 µL of cDNA was used for PCR in a 12.5 µL reaction volume. PCR Master Mix (2X) (Thermo Scientific) was used for PCR amplification. 0.5 µL of each primer (5 pM) was added to the reaction. Samples were amplified with a pre-cycling hold at 95°C for 3 min, followed by 30 cycles of denaturing at 95°C for 1 min, annealing at 43°C for NCB (PP1Ɣ2) and β-Actin (used as an internal control) at 56°C temperatures for 30 s, and extensions at 72°C for 1 min followed by a final extension step at 72°C for 3 min in a thermal cycler (ProFlex PCR system Applied Biosystems). The specific primer sequence for PP1Ɣ2 (forward 5' GTGGTTGAAGATGGATATGA 3' and reverse 5' CTGATGCAACCCTTG 3') and β-Actin (forward 5'GAGCTACGAGCTGCCTGACG3'and reverse 5' CCTAGAAGCATTTGCGGTGG 3') were used for the amplification. Further, PCR products were separated on 2 % agarose gels containing ethidium bromide and visualized on a Gel doc (Bio-Rad, Hercules, CA, USA).

III. Immunofluorescence on cervical scrap/smear

Cervical scrap slides were first incubated with 95% ethanol to remove the layer PEG present in the spray fixative and then washed with PBS. The smear on the slide is divided into two halves through the tissue paper to demarcate positive and negative sides and make boundary via liquid blocker. Now slides were permeabilized for 10 min and followed by 1X PBS washing after that blocking with 2% BSA. Cell scrap was subjected to primary antibody i.e, PP1Ɣ2 (raised in rabbit) and HPV (raised in mouse), for 10 to 12 h incubation inside the

humid chamber at 4° C. The slides were gently washed 2 times, with 0.1 % PBST, followed by 1X PBS twice. After that, slides were incubated with respective fluorophore tagged secondary antibody for 4 h inside the dark humid chamber at room temperature. After incubation, slides were again washed with 0.1% PBST and 1X PBS twice. Subsequently, the slides were counterstained with DAPI (Sigma Aldrich) at 1µg/mL concentration for 20 min followed by washing with 1X PBS twice, and then smear on glass slides was mounted by coverslip up-side-down on the drop of Prolong Gold Antifade Reagent (Invitrogen) and sealed with nail polish. Pap smear slides were viewed, and images were captured using confocal (LEICA TCS SP8) and fluorescence microscopes (LEICA DMI 6000B).

IV. Protein isolation from urine

Freshly collected midstream urine samples in 50 mL sterilized centrifuged tube were filtered through 8 µm Whatman filter paper and centrifuged at 1000*g* for 5 min in 4° C. The supernatant was collected in a fresh tube and an equal volume of acetone was added. Protein was precipitated by incubating tubes at – 20°C for 45 min. After precipitation, tubes were centrifuged at 12000*g* for 5 min at 4°C. The supernatant was discarded and precipitated protein was resuspended in RIPA lysis buffer, and protein was quantitated through the Bradford method, made aliquots, and stored at -80ºC until use.

V. SDS-PAGE and western blotting

Extracted and accurately quantified 30 µg protein from urine were denatured with Laemmli buffer (1M Tris-HCl, pH 6.8, 6.25%; Glycerol 25%; SDS 2% and 0.01% Bromophenol blue) by addition in 1:1 ratio. The samples were then boiled at 95°C for 10 min. The urine isolated protein was loaded into each well and electrophoresed on 12.5% SDS-PAGE gel. The SDS-PAGE separated proteins were transferred onto a nitrocellulose membrane by electro-blotting. The blotted membrane was stained with ponceau stain for the confirmation of complete transfer of protein from gel to the membrane. It was then washed with 1X PBS and kept for blocking in 2 % Bovine serum albumin (BSA) in 0.1 % PBST for 1 h. The blotted membrane was then incubated with a specific primary NCB (PP1Ƴ2) antibody raised in rabbit (1:5000), for 10-12 h at 4° C. The nitrocellulose membrane was washed with 0.1 % PBST three times, and then with 1X PBS twice at the interval of 10 min. The membrane was further subjected to secondary antibody i.e., anti-Rabbit HRP (1:10000) for 4 h at room temperature (25° C). Thereafter, the membrane was washed with 0.1% PBST three times at an interval of 10 min along with 1X PBS twice; further protein bands were detected by using ECL reagent and developed with the aid of a chemi-documentation system (Image Quant LAS 4000, GE Life Science, PA, USA).

VI. Preparation of solutions

(a) Phosphate buffered saline (PBS) buffer:

For 1 L 10X Phosphate Buffered Saline (PBS), 25.6 g of di-Sodium hydrogen phosphate ($Na_2HPO_4.7H_2O$), 80 g of NaCl, 2 g of KCl, and 2 g of potassium di-hydrogen phosphate (KH_2PO_4) reagents were dissolved properly in Milli-Q water and the final volume was made up to 1 L. This 10X PBS buffer was stored at 4°C for further use and diluted to 1X at the time of using this buffer.

(b) Phosphate buffered saline with Tween-20 (PBST) buffer

Phosphate buffered saline with Tween–20 (PBST) buffer was prepared by dissolving 0.1% (v/v) of Tween–20 surfactant to the required amount of prepared 1X PBS buffer and 4° C storage condition was maintained.

(c) Laemmli buffer

Laemmli sample buffer (2X) was prepared by using 100 mM of Tris HCL (pH 6.8), 0.02% bromophenol blue, 10% β-mercaptoethanol, 2% SDS, and 20% glycerol in double distilled/RO water.

(d) Tris-Glycine and SDS buffer

Tris–glycine running buffer (1X) was prepared by dissolving 25 mM Tris, 192 mM glycine, and 0.1% SDS in double distilled/RO water.

(e) Transfer buffer

Transfer buffer (2X) was prepared by dissolving 50 mM Tris Base, 384 mM Glycine, and 10% Methanol in double-distilled/RO water.

(f) Antibody solution

About 1% (w/v) Bovine Serum Albumin (BSA) solution was prepared with a previously prepared PBST solution. A 2.44 mg/mL stock solution of antibody was diluted maintaining a ratio of 1:3000 in freshly prepared 1% BSA solution. The stock solution of the antibody was stored initially at – 20° C. For dilution purposes, the antibody stock solution was thawed at 4°C. The diluted antibody solution was then kept again at – 20°C until further use.

VII. Sensor preparation

(a) Synthesis of Au NPs

Aqueous $HAuCl_4$ solution of 0.25 mM was prepared by dissolving 10 mg of $HAuCl_4$ in 100 mL of Milli-Q water with stirring to mix the solution well. 0.1 M aqueous reducing agent solution was prepared by dissolving 0.38 g of $NaBH_4$ in 100 mL of Milli-Q water. Afterward, 20 mL of $HAuCl_4$ was taken in a beaker and was stirred at 1030 rpm. Then, 100 µL of reducing

agent solution was added, dropwise, to $HAuCl_4$ solution under vigorous stirring. The change in the color of the stirring solution from yellow to orange at first and subsequently to wine red, in nearly 10 min, indicates the formation of Au NPs. The Au NPs solution thus synthesized was stored at 4º C in an airtight container for further use.

(b) Preparation of DTSP solution

DTSP solution having the strength of 5 mM was prepared by dissolving 2 mg of solid DTSP powder in 1 mL of Milli-Q water. For further usage, 1:10 dilution of the prepared DTSP solution in Milli-Q water was done and was kept at 4º C in an airtight container for subsequent use.

(c) Attachment of DTSP on Au NPs

To obtain DTSP attached Au NPs solution, 1300 µL of the DTSP solution (1:10 diluted) was added to 7 mL of synthesized Au NPs solution. It was then filtered using a 0.45 µm diameter syringe filter after 1 h. The filtered solution was stored at 4°C for experimental purposes.

(d) Attachment of Ab on DTSP linked Au NPs

About 1.5 mL of DTSP-Au NPs solution was mixed with 60 µL of the prepared Ab solution and kept for 30 min at 4° C.

2.3 Characterization

2.3.1 Instruments

For the present study, the characterization instruments used were UV-vis spectrophotometer (Shimadzu, UV-2600 230 V EN), transmission electron microscopy (TEM, JEOL, JEM 2100 at the acceleration voltage of 200 kV), Raman spectroscopy (Horiba Scientific, LabRAM HR Evolution), magnetic stirrer cum hot plate (Tarsons, Digital Spinot), weighing machine (Sartorius, BSA224S-CW), desiccator (Tarsons), vacuum pump (Toshmiwal), deep freezer (Haier), SDS-PAGE and western blot assembly (Bio-Rad), Pierce power station (Thermo Scientific), gel doc (Bio-Rad, Hercules, CA, USA), confocal microscope (LEICA TCS SP8), fluorescence microscope (LEICA DMI 6000B), and chemi-documentation system (Image Quant LAS 4000, GE Life Science, PA, USA).

2.3.2 Characterization of NCB

I. Western blot (WB) analysis

Sample preparation was done in Laemmli buffer by adding isolated protein extract from a urine sample in 1:1 ratio v/v.[206] In this process, accurately quantified protein extracted from urine was denatured with Laemmli buffer containing BME (10%). The samples were heated at 95°C for 10 min on a hot plate to complete the denaturation process. Thereafter, the denatured

protein samples (30 µg) were loaded in each well of 12.5 % SDS-PAGE before the gel was electroporated in a tris-glycine-SDS buffer system at a constant voltage of 50 V. Proteins separated through SDS-PAGE were transferred onto nitrocellulose membrane by electro-blotting. The membrane was then stained with ponceau stain to visualize the blotted proteins. Thereafter, the membrane was washed with 1X PBS and kept for blocking in 2 % BSA prepared in PBST (0.1%) for 1 h on a rocker shaker, at 25°C. The blot was then incubated with NCB specific primary Ab at 1:3000 standardized dilutions overnight at 4°C. Following this, the membrane was washed with 0.1% PBST three times and with PBS (1X) twice. Then the secondary Ab tagged with HRP was added at a standard dilution (1:5000) and left undisturbed for 4 h at 25°C. The membrane was then washed with PBST (0.1%) three times followed by two times washing through PBS (1X) buffer.

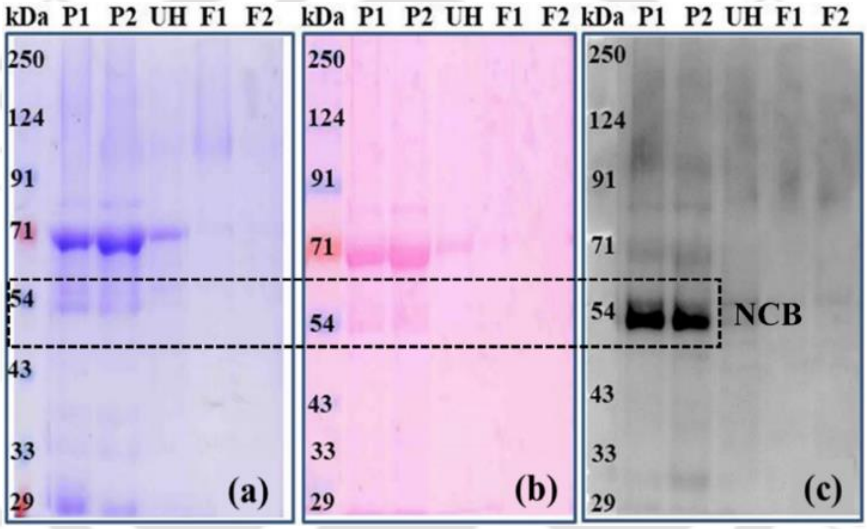

Figure 2.2: The comparison of the total excreted protein and detection of NCB in the urine samples of healthy female and CaCx patients. (a) Coomassie staining of blot shows separated urine proteins through SDS–PAGE. (b) Ponceau staining of blot shows blotted protein profile of various urine samples. (c) WB shows the shedding of NCB–Ag in CaCx patients' urine. P1: recurrence of CaCx; P2: CaCx stage IIIB; UH: unhealthy with abnormal pap but noncancerous cervix; F1 and F2: healthy female urine sample.

Figures 2.2(a) and **2.2(b)** show total protein profiles obtained after size-based separation of the different proteins present in the loaded urine samples in each lane. In these plots, P1 represents the samples of the patients with the recurrence of CaCx, P2 represents the samples of the patients with CaCx stage IIIB, UH represents the samples of the patients having unhealthy abnormal pap but noncancerous cervix, and F1 and F2 represent the samples of the healthy female patients. **Figure 2.2(a)** shows the results with the Coomassie brilliant blue staining solution to visualize the protein bands in the acrylamide gel after the electrophoresis. In **Figure 2.2(b)** ponceau pink stain is showing protein bands on the nitrocellulose membrane after electro transfer of protein from SDS-PAGE gel to nitrocellulose membrane. Coomassie

staining is used to visualize the separated proteins in the gel, whereas the pink color ponceau stain is used to confirm the protein blotting on the membrane when the proteins are transferred from gel to the nitrocellulose membrane. Since the ponceau staining is temporary, it could be washed away through water easily. The bands apparent from these two stains depict the abundance of any separated protein(s) present in the urine sample, based on their size. The prominent bands may or may not have the protein of interest.

However, when a specific anti–NCB Ab is used against the protein of interest, the Ag–Ab complex is formed. Consequently, the luminescent signal associated with the enzyme–substrate reaction can be captured through the Gel Doc. **Figure 2.2(c)** depicts the specific band on the membrane, which has been probed with anti–NCB specific primary Ab followed by enzyme tagged secondary Ab. Subsequently, the substrate has been characterized using the chemiluminescence method to produce the specific signal showing the existence of NCB–Ag in the urine sample. Thus, it can be inferred that, although **Figure 2.2(a)** and **Figure 2.2(b)** have protein(s) abundance at 71 kDa, WB does not show any signal at 71 kDa in **Figure 2.2(c)**. In contrast, the NCB protein, at 54 kDa, is not abundant in **Figures 2.2(a)** and **2.2(b).** However, in **Figure 2.2(c)**, a sharp band around 54 kDa for NCB can be observed, due to the specificity of the Ag–Ab complex. It proves the specific binding affinity of the Ab to NCB present in the urine sample.

2.3.3 Characterization of sensor

I. Raman spectroscopy

Raman Spectroscopy was used to characterize Ag–Ab interactions. For the characterization, a small piece of glass was cleaned thoroughly following a standard glass cleaning protocol for impurity free analysis purposes. A layer of Au NPs was deposited on the pre–cleaned glass pieces before the actual preparation of the sample. For this purpose, Au NPs solution (20 µL) was dispensed, followed by a vacuum drying step. The steps were repeated thrice for sufficient Au NPs deposition on the glass surface. After appropriate drying, Ab solution (20 µL) was dispensed on the prepared glass substrate and was kept overnight for vacuum drying. The sample for Raman spectroscopy of Ag was also prepared following the same protocol.

For the interaction study, the Ag solution was mixed with Ab solution in a separate Eppendorf and the mixture was allowed to interact for ~ 1 h, at 4^{o}C. Subsequently, the prepared solution (20 µL) was dispensed on Au NPs embedded glass slide and was kept overnight under vacuum drying. The same protocol was followed for sample preparation for the characterization of Ag and Ab interactions on top of DTSP linked Au NPs.

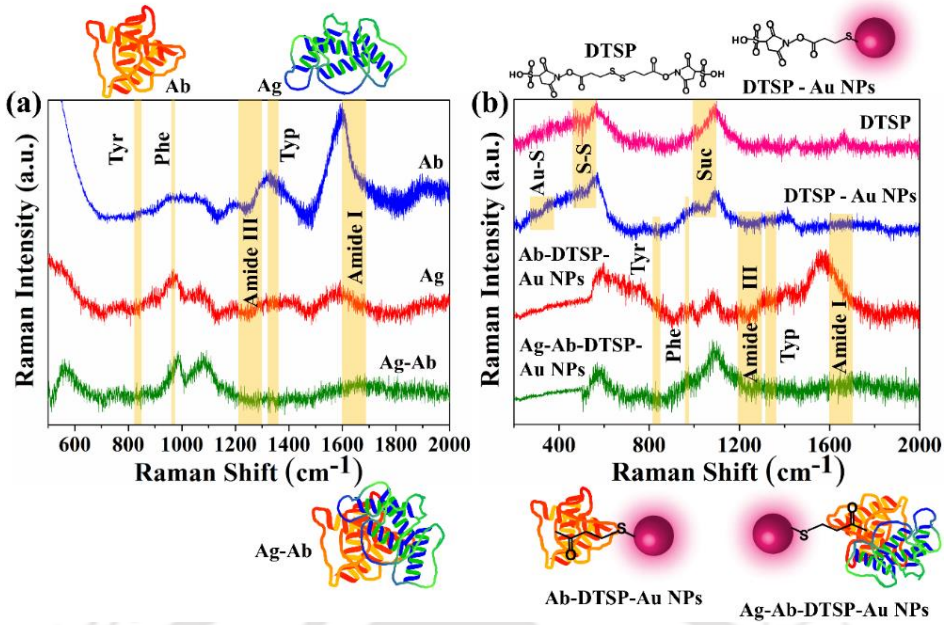

Figure 2.3: Image (a) shows Raman spectra of pristine Ab, Ag, and Ag–Ab interaction. Image (b) shows Raman spectra of pristine DTSP, DTSP–Au NPs, Ab–DTSP–Au NPs, and Ag–Ab–DTSP–Au NPs.

Figure 2.3(a) shows Raman characterization of pure Ab, pure Ag, and of Ag–Ab after 1 h interaction. The characterization parameters were as follows: 532 nm laser wavelength, 10 s accumulation time, 4 s acquisition time, 10% modulation, 20X optical magnification, and grating of 1800 gr/mm. **Figure 2.3(a)** shows that for both pure Ab and pure Ag samples, medium characteristic peaks for amide III (ranging from 1229–1300 cm^{-1}) and strong spectral peak for amide I (ranging from 1600–1690 cm^{-1}) are present, which signifies the primary structure of the proteins. In addition, characteristic peaks for secondary structures of aromatic amino acids such as phenylalanine (Phe) (at 1000 cm^{-1}), tyrosine (Tyr) (ranging from 830–850 cm^{-1}), tryptophan (Typ) (ranging from 1340–1360 cm^{-1}) are also observed for both Ab and Ag samples. The disulphide band (ranging from 500-550 cm^{-1}) is also observed for Ag. The details of characteristic peaks of Ag and Ab obtained from these experiments are listed in **Table 2.1**.

The interaction of Ag–Ab is considered as a reversible biomolecular reaction,[207] where the Ab binds to the corresponding Ag by weak van der Waals and/or weak columbic interaction between the opposite charges and complementary hydrogen bonds of the two species. Thus, the weak interaction of Ag–Ab does not modify the secondary structures and the disulphide band ranging in between 500–550 cm^{-1}. The unmodified secondary structure bands and significant disulphide band after Ag–Ab interaction can be seen in **Figure 2.3(a)**. The previous studies on Ag–Ab interaction[208] explain that due to coupling from weak forces of attraction, the interaction of Ag–Ab shows no distinct characteristic peak but a combination of spectral

peaks of pristine Ab and Ag in Raman analysis, consistent with **Figure 2.3(a)**. Importantly, a similar trend is expected when the interactions materialize on the surface of Au NPs, since the Au NPs are inert with respect to Raman spectroscopy. For verification, Raman characterizations are repeated with pure DTSP, DTSP linked Au NPs (DTSP–Au NPs), Ab immobilized on DTSP linked Au NPs (Ab–DTSP–Au NPs), and Ag–Ab attached DTSP linked Au NPs (Ag–Ab–DTSP–Au NPs), and are shown in **Figure 2.3(b)**.

Table 2.1: Raman spectroscopy spectral peaks.

Pristine Ab		**Pristine Ag**		**Ag–Ab interaction**	
Spectrum	Shift (cm^{-1})	Peak	Shift (cm^{-1})	Peak	Shift (cm^{-1})
Aliphatic side chain vibration	1420–1466	Aliphatic side chain vibration	1420–1466	Aliphatic side chain vibration	1420–1466
C-H stretching of aliphatic side chain	2860–2940	C–H stretching of aliphatic side chain	2860–2940	C–H stretching of aliphatic side chain	2860–2940
C-C vibration or alkyl C-N	1032–1170	C–C vibration or alkyl C–N	1032–1170	C–C vibration or alkyl C–N	1032–1170
Amide III	1229–1300	Amide III	1229–1300	Amide III	1229–1300
Amide I	1600–1690	Amide I	1600–1690	Amide I	1600–1690
Tyrosine	830–850	Tyrosine	830–850	Tyrosine	830–850
Phenylalanine	1000	Phenylalanine	1000	Phenylalanine	1000
Tryptophan	1340–1360	Tryptophan	1340–1360	Tryptophan	1340–1360
		Disulphide	500–550	Disulphide	500–550
DTSP–Au NPs		**Ab–DTSP–Au NPs**		**NCB–Ab–DTSP–Au NPs**	
Au-S bond	300–400	Aliphatic side chain vibration	1380–1470	Aliphatic side chain vibration	1380–1470
Symmetric and asymmetric C=O bend	512–598	C–H stretching of an aliphatic side chain	2860–2990	C–H stretching of an aliphatic side chain	2880–2960
Succinimide ring bend (Suc)	1000-1050	C-C vibration or alkyl C-N	1050–1100	C–C vibration or alkyl C–N	1035–1135
C-C stretching band	1077-1133	Amide III	1229–1300	Amide III	1229–1300
Symmetric C=O stretch	1680-1820	Amide I	1600–1690	Amide I	1600–1690
C-S	630-790	Tyrosine	830–850	Tyrosine	830–850
C-C vibration	1380-1470	Phenylalanine	1000	Phenylalanine	1000
		Tryptophan	1340–1360	Tryptophan	1340–1360

It shows the peaks specific to the pristine DTSP such as disulphide bond (ranging from 500–550 cm^{-1}), ring bending of succinimide (Suc) structure (ranging from 1000–1050 cm^{-1}), aliphatic C–S bond (ranging from 630–790 cm^{-1}), and C=O bond (ranging from 1680–1850 cm^{-1}). **Figure 2.3(b)** also shows the spectral peak of the Au–S bond (ranging in between 300–400 cm^{-1}) along with other specific peaks of DTSP, signifying the attachment of DTSP on Au NPs via thiol bond. In the subsequent attachment of Ab to DTSP–Au NPs, the Ab attaches to

the linker by amide bonding (–NH_2 of the Ab attaches with the –COOH of linker). The figure shows all the specific peaks of primary and secondary structures of Ab (refer to Figure 2.3(a)) along with Au–S peak, and proves the linking of Ab with DTSP–Au NPs. **Figure 2.3(b)** also illustrates the spectral peaks observed after the addition of Ag on Ab–DTSP–Au NPs solution. As expected, all the peaks including the amide I and III are observed with a distinct variation in the peak intensities with a marginal Raman shift, as summarized in **Table 2.1**. It should be noted that the Raman spectra obtained after the addition of Ag on Ab–DTSP–Au NPs shows a significant relevance with the Raman spectra for the interaction of pristine Ag and Ab with the addition of Au–S peak.

II. TEM analysis

The TEM analysis was performed to visualize the change in size and agglomeration pattern at different steps of linker and biomolecule attachments on Au NPs. **Figure 2.4(a)** shows the TEM image for pristine Au NPs with a scale bar of 50 nm. It is observed that the size of the synthesized Au NPs remains in the range of ~ 5–10 nm, as shown in the particle size distribution of the Au NPs in **Figure 2.4(a)**. In this range, the Au NPs have a characteristic wine–red color, as shown in the inset of Figure 2.4(a). **Figure 2.4(b)** shows the TEM image of DTSP–Au NPs, which form a chain like agglomeration of DTSP linked Au NPs. The DTSP is bifunctional linker molecule containing reactive groups in both the ends with a disulfide bond at the center. In the presence of the gold nanoparticles, the disulfide bond cleaves to form two fragments of DTSP, each containing a sulfhydryl group (-SH) and a succinimidyl group at the other end. DTSP attaches to the gold nanoparticles via strong coordination bond formation of Au-S. The proximity of alike DTSP bound gold nanoparticle with similar negative surface charges facilitates a controlled aggregation of the nanoparticles with a degree of uniformity[209] through non-covalent interactions such as van der Waals forces, electrostatic interactions. These non-covalent forces long with the steric hindrance and spatial arrangement of DTSP provides a stable aggregated structure forming networks of gold nanoparticles which in the present work was observed to be a serpentine chain like aggregation. Similar aggregated chain like structures were recorded for multiple experiments performed in the present work. The chaining of DTSP linked Au NPs shows a blue coloration due to the effects of LSPR, as seen in the inset of **Figure 2.4(b)**.

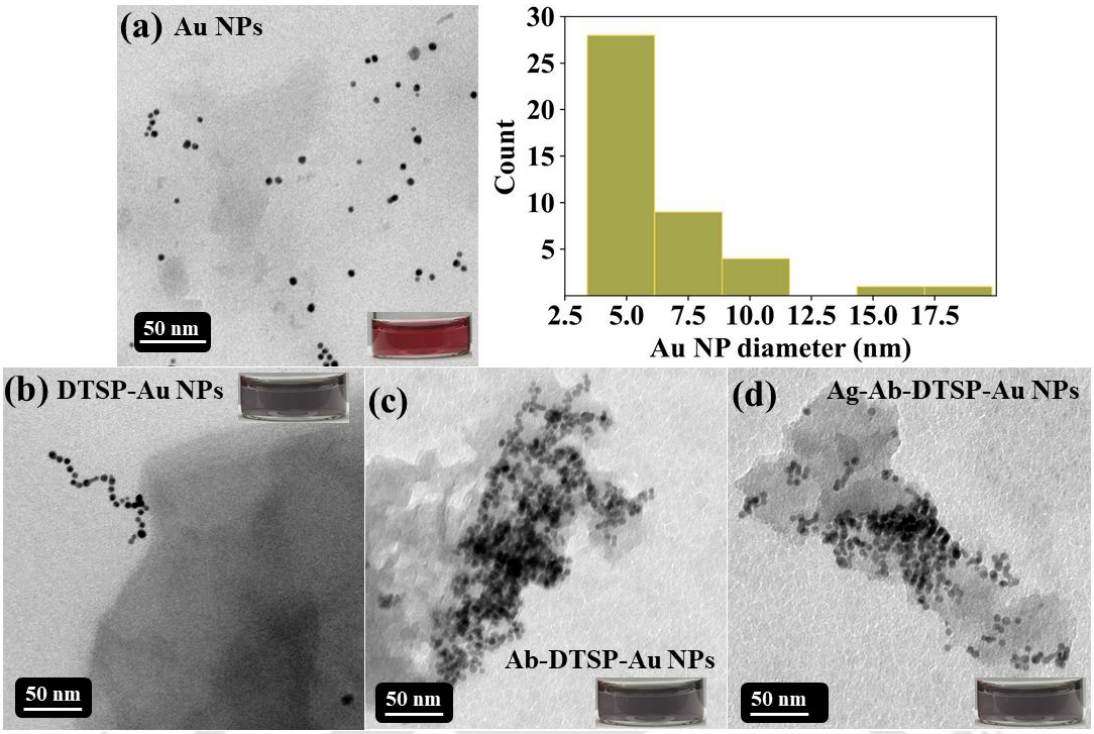

Figure 2.4: The TEM images of (a) pristine Au NPs and particle size distribution of the Au NPs (b) DTSP–Au NPs (c) Ab–DTSP–Au NPs (d) Ag–Ab–DTSP–Au NPs. The inset in each image shows the corresponding color of Au NPs.

Figure 2.4(c) shows the TEM image of Ab–DTSP–Au NPs, which makes clusters. Inset of Figure 2.4(c) shows that there is not much visual color change on the addition of the Ab on the DTSP linked Au NPs solution; however, due to the aggregation of dielectric Ab, the charge distribution changes and leads to an LSPR change, which has been discussed in the following section. **Figure 2.4(d)** and its inset show change in clustering and visual color of the system, after the addition of Ag to this Ab–DTSP–Au NPs. In this case, it can be seen that on the addition of Ag, the chaining collapses, and the interparticle distance between Au NPs increases.

2.4. Results and Discussion

2.4.1. NCB for CaCx diagnosis

Cancer Testis Antigens (CTAs) are proteins for which the expression is restricted to the testis and overexpression of them has been observed in various malignancies.[210] Thus, aberrant CTA profiles are explored as biomarkers for detection as well as the selection of cancer. Importantly, unusually higher expression of CTAs remains foreign to the immune system of a human body and is considered to be a potent biomarker for cancer diagnosis.[210] For example, PP1Ɣ2, the NCB considered here, has been reported[211] as a testis-specific isoform of protein phosphatase. In this study, the expression of this protein has been observed in the cervical cancer cells before characterizing the same as NCB to develop the pathway of non-invasive POCT of CaCx.

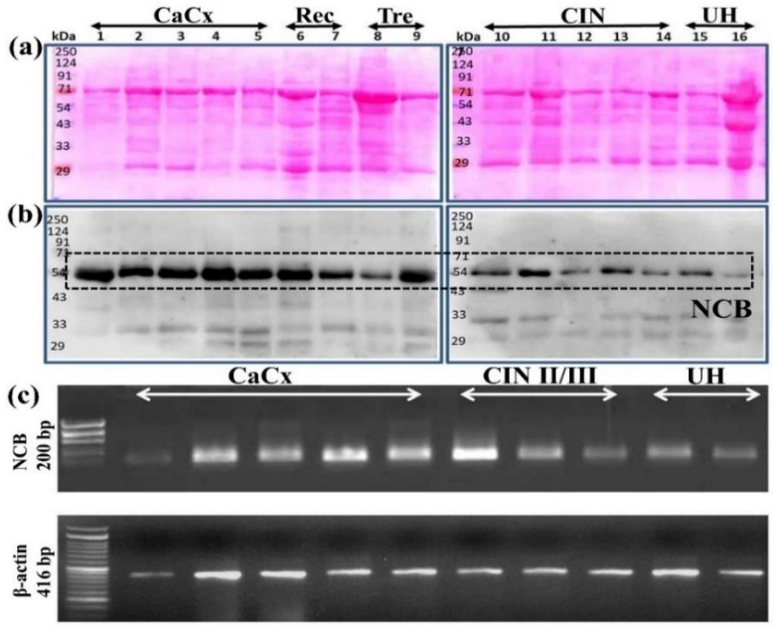

Figure 2.5: Shows the detection of NCB in the urine samples collected from various stages and groups of CaCx. Plot (a) shows the ponceau staining of blots. The WB analysis in the plot (b) shows the shedding of NCB–Ag in urine, where lanes 1 to 5 correspond to CaCx, lanes 6 and 7 correspond to recurrence cases (Rec), lanes 8 and 9 correspond to patients undergoing treatment (Tre), lanes 10 to 14 for CIN, and lanes 15 and 16 for abnormal pap with unhealthy but noncancerous cervix (UH). (c) Gel-electrophoresis showing the expression of NCB transcript in the CVF collected from clinically confirmed patients of CaCx, CIN, and UH stages. Here, β–actin served as an internal control for the reaction.

Figure 2.5 shows the results of WB analysis obtained using urine samples of patients suffering from different stages of CaCx. The results correspond to the patients, (i) having a recurrence of CaCx (Rec), (ii) undergoing treatment (Tre), (iii) having a precancerous stage of cervical intraepithelial neoplasia (CIN), and (iv) having an abnormal pap with an unhealthy cervix, however, not diagnosed with CaCx (UH). **Figure 2.5(a)** shows the ponceau stained profiles of all the proteins in the urine samples separated by the SDS–PAGE procedure. The color intensities of the bands suggest that NCB at 54 kDa is not present in abundance as compared to other proteins for any patient. In fact, the intensities of the bands for NCB are rather weak in the ponceau stained membrane. **Figure 2.5(b)** shows the results after the separated proteins are allowed to interact with the Ab specific to NCB–Ag. In this situation, intense bands are observed after the interaction since the NCB–Ag has the highest affinity towards the Ab. Importantly, the figure also suggests that the intensity of the NCB bands in the urine sample of the unhealthy patients varies with the cases, viz. CaCx, Rec, Tre, CIN, and UH. The results indicate that the NCB can also be a competent marker in identifying different stages of CaCx. In particular, the NCB can be conclusively employed to differentiate CaCx from the cases of CIN, Rec, or Tre. In order to confirm the results, the expression of NCB transcript has been verified in the cervico–vaginal fluid (CVF) of the clinically confirmed

patients of CaCx and CIN with the help of Gel Electrophoresis (GE) and micrograph staining. The CVF has been collected at the early as well as advanced stages of the clinically confirmed patients for CaCx and the RNA is extracted. Expression of NCB transcript has been checked in these samples through conventional Reverse Transcriptase Polymerase Chain Reaction (RT-PCR) using NCB specific primers. **Figure 2.5(c)** shows the transcript expression of NCB (~200 bp) in all the cancerous samples. The signals have also been observed in CIN stages while faint bands are detected in CVF collected from the UH cases.

In order to evaluate the NCB expression at the translational level in the CVF collected from the CaCx patients, the indirect immunofluorescence technique has been used. For this purpose, the slides have been prepared from the patient's CVF samples and then incubated with anti-NCB specific antibody for immunostaining. The columns (b) and (c) in **Figure 2.6** confirm the NCB expression in the CVF samples of the CaCx patients with stages IIB and IIIB, while the same being absent in the CVF of healthy patients in column (a) as it did not show any immune-reactivity when incubated with anti–NCB primary Ab. Co–immuno–localization of NCB and HPV in the CVF collected from patients with precancerous as well as various stages of CaCx has also been analyzed using the dual immunostaining technique. For this purpose, the CVF slides have been probed with specific anti-NCB and anti-HPV primary Ab. The HPV Ab has been chosen against the consensus region of E6 oncoprotein of HPV 16 and 18.

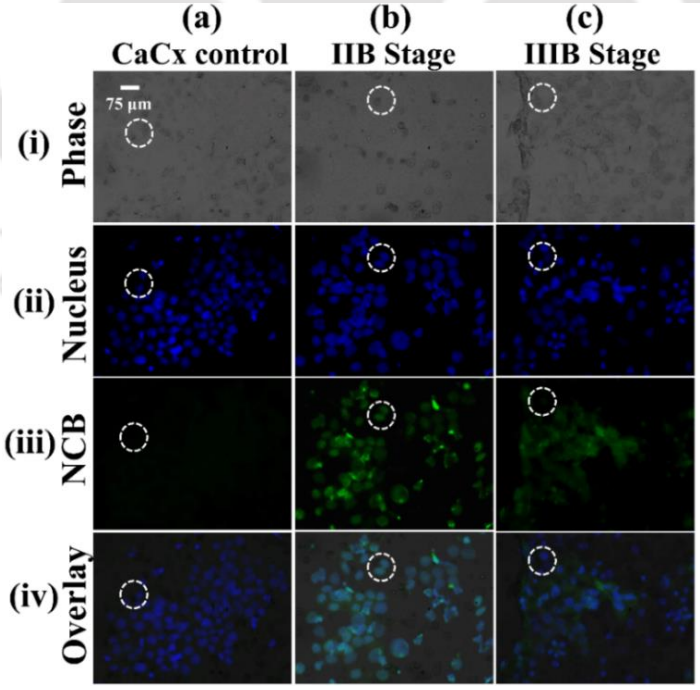

Figure 2.6: Confocal photomicrograph showing signal of NCB in the cells of the CVF collected from the clinically confirmed CaCx patients. The columns (a) – (c) show the images corresponding to the control and CaCx at stages IIB and IIIB. The rows (i) – (iv) display the grayscale, DAPI stained nucleus, FITC fluorophore showing green fluorescence to signify NCB and overlays, respectively. Scale bar has been shown to represent 75 µm microscopically.

Figure 2.7 shows a positive immuno-staining for both NCB (red fluorescence from CY3 attached to the secondary Ab of NCB, as shown in row (iii)) and HPV (green fluorescence from FITC attached to the secondary Ab of HPV, as shown in row (iv)) in the unhealthy patient samples wherein the blue fluorescence in the row (ii) depicts the nucleus stained with DAPI. A number of studies have also been done to test the presence of the NCB in the urine samples of healthy or affected patients using WB, as tabulated in **Table 2.2**. The results suggest that the NCB is proficiently expressed in ~86% of precancerous CIN II/III stage of CaCx, ~73% of the patients undergoing treatment, ~73% of patients having abnormal pap, and 100% of the recurred cases.

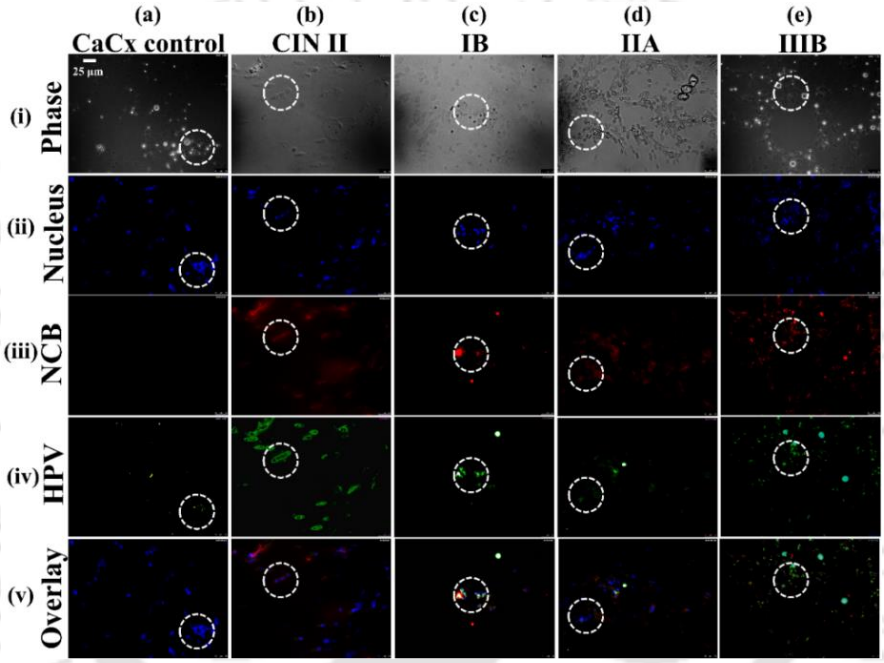

Figure 2.7: Confocal photomicrograph showing co-expression of NCB and HPV in CVF collected from early and advanced stages of CaCx patients. The columns (a)–(e) show the response from the samples from the different stages of CaCx, i.e., control, CINII, IB, IIA, and IIIB. The rows (i)–(v) respectively display the grayscale, DAPI stained nucleus, CY3 fluorophore showing red fluorescence for NCB, FITC fluorophore showing green fluorescence for HPV, and overlays. Scale bar has been shown to represent 25 µm microscopically.

The data in **Table 2.2** suggest that the said biomarker is capable of confirming the different stages of CaCx (IA/IB, IIA/IIB, and IIIA/IIIB) with average ~90% accuracy. Interestingly, of all the healthy volunteers tested, none is found to be positive for the presence of NCB, which shows the efficacy of the said biomarker to distinguish the healthy and CaCx patients.

In addition, the expression of NCB in CVF samples is also confirmed by performing RT-PCR of the CVF samples collected from a number of patients at different stages of CaCx, as summarized in **Table 2.3**. All these results direct the potential of the NCB in the detection of CaCx along with differentiating various stages.

Table 2.2: Statistics of urine samples tested for NCB through Western Blot technique.

Sample type	Number of samples tested	Number of positive samples in WB
Healthy volunteers	05	0/05 (0%)
Abnormal noncancerous Pap	30	22/30 (73%)
CIN II/III	50	43/50 (86%)
IA/IB	05	04/05 (80%)
IIA/IIB	42	39/42 (93%)
IIIA/IIIB	33	31/33 (94%)
Follow-up treated cases	15	11/15 (73%)
Recurrence	05	05/05 (100%)
Total urine samples	**185**	**155/185 (84%)**

Table 2.3: Clinoco-pathology of CVF samples for NCB using RT–PCR.

Clinoco-Pathological Stage of Samples	Sample Size	Samples positive for NCB (RT–PCR)
Non-Cancerous Abnormal pap	25	11/25 (44%)
CIN	25	15/25 (60%)
Cervical cancer	50	41/50 (82%)
Treated	10	04/10 (40%)
Recurrence	05	03/05 (60%)
Total	**115**	**74/115 (64%)**

Table 2.4 summarizes the clinico-pathological details of samples, found to be positive for the expression of NCB in both CVF (Pap) and urine specimens of the various stages of CaCx patients. The results show that the WB technique is competent enough to recognize the presence of the NCB protein in unhealthy cases. The process is highly specific because, firstly, the step of GE where the proteins get separated according to size provides a clue about the presence of the protein of interest. The second specificity comes in the step of the Ag–Ab interaction where the specific Ab shows high affinity towards the specific NCB–Ag present in the mixture of separated proteins. Since the WB method is sensitive enough to detect proteins even at the nanogram level, this technique has been employed to serve as an effective diagnostic tool to sense the slightest immunogenic response of NCB in the urine sample of a patient. Clearly, the results summarized in **Tables 2.2, 2.3,** and **2.4** elucidate that the detection of the different stages of CaCx through the level of NCB in urine can be a reliable method and the predictions from the same are either comparable or better than the existing GOLD standard[162] method for screening.

The results summarized in **Figures 2.5–2.7** and **Tables 2.2, 2.3,** and **2.4**, help in concluding that the NCB protein in urine can be deployed as a potential biomarker to detect various CaCx cases at different stages. Importantly, such a noninvasive pathway can stimulate a paradigm

shift in the POC screening of CaCx avoiding the presently available invasive techniques. However, using the aforesaid method, the major roadblock in the POC detection has been the use of WB, which requires about ~ 8 h to perform a single test. Further, the technique requires skilled professionals to reduce the risk of false negative cases. Moreover, the WB technique also limits a POC application because of (i) expenses for bulky and pricey laboratory equipment, (ii) requirement of additional detection and imaging apparatus such as chemiluminescent, fluorescent, radioactive, or laser detection systems, and (iii) utility in a centralized path-lab for operations. In view of such challenges, we propose the development of a portable, user friendly, and easy-to-handle POCT prototype for real time detection of NCB from the urine samples.

Table 2.4: Clinico–pathological details of samples positive for the expression of NCB in CVF and urine specimens of various stages of CaCx.

Sl.No.	Sample type	Total number of samples	Positive for NCB expression	
			PAP (RT–PCR)	Urine (Western Blot)
1.	Non–Cancerous/Abnormal	08	03/08(37%)	04/08(50%)
2.	CIN II/III	13	04/13(31%)	10/13(77%)
3.	CaCx IIA/IIB	12	06/12(50%)	11/12(92%)
4.	CaCx IIIA/IIIB	10	06/10(60%)	09/10(90%)
5.	Treated	07	02/07(29%)	06/07(86%)
6.	Recurrence	02	01/02(50%)	02/02(100%)
	Total	**52**	**22/52(42%)**	**42/52(81%)**

2.4.2. Sensing principle

Previously, while describing Figure 2.1, we have summarized the working principle of the proposed sensor. **Figure 2.8(a)** shows the absorbance spectra of the synthesized Au NPs and the composites, viz. DTSP–Au NPs, Ab–DTSP–Au NPs, and NCB–Ab–DTSP–Au NPs. At the outset, the synthesized Au NPs (0.5 mL) show a characteristic absorption peak at ~520 nm (pink line) after mixing with Mili–Q water (1 mL). Considering this, a solution of DTSP–Au NPs (0.5 mL) diluted with Mili–Q (1 mL) water shows a red shift of 2-3 nm. The shift of 2-3 nm after the attachment of DTSP on the surface of Au NPs as obtained was found to be consistent for multiple experiments performed in the present work. Such a shift of peak wavelength with the linking of DTSP and Au NPs has been reported by a number of prior arts hinting the immobilization of Ab on DTSP–Au NPs and its origin towards the effects of LSPR.[212] Subsequently, Ab solution (60 µL) in PBST buffer is added to the DTSP–Au NPs where no considerable shift in the spectra is observed, as shown by the delta symbols in the plot. The kinetics of the attachment of the Ab to the DTSP capped Au NPs has also been studied

using UV–Vis Spectroscopy by following the variations in absorbance at an interval of 5 min for a period of 40 min. Next urinal protein solution (300 µL) containing the NCB–Ag, which is separated from urine collected from the CaCx patient, is added to the Ab–DTSP–Au NPs solution. As shown in **Figure 2.8(a)**, a significant blue shift ($\Delta\lambda$) with a concurrent increase in absorbance is observed on the addition of NCB–Ag to the Ab–DTSP–Au NPs solution.

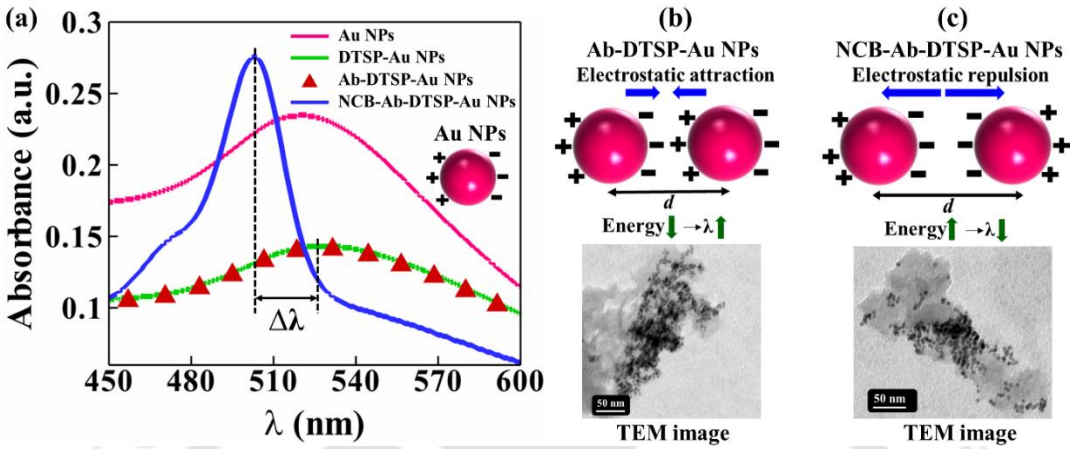

Figure 2.8. Plot (a) shows UV–Vis absorbance of pristine Au NPs, DTSP-Au NPs, Ab-DTSP-Au NPs, and NCB–Ab–DTSP–Au NPs. Image (b) shows the schematic diagram and the corresponding TEM image for a decrease in interparticle distance between the Au NPs after the immobilization of Ab on DTSP–Au NPs. Image (c) shows the schematic diagram and the corresponding TEM image for an increase in interparticle distance between the Au NPs after the attachment of NCB–Ag on Ab–DTSP–Au NPs.

The explanation of such observation lies in the near field coupling phenomenon, which occurs due to change in the interparticle distance between the plasmonic Au NPs caused by the change in the surrounding dielectric medium. When the bare Au NPs of size ~5–15 nm are irradiated with an incident electromagnetic wave, the coherent oscillation of the plasmons on the surface of Au NPs stimulates LSPR and gives the characteristic UV-Vis peak. Such LSPR creates a dipole with a separation of charges on the Au NPs surface, and develops a localized electric field opposing the incident radiation. On the addition of DTSP, the localized electric field generated on the Au NPs induces polarization of the surrounding dielectric liquid medium to buildup charges.[213] Such mutual polarization compensates the accumulation of electrons on the surface of Au NPs, eventually reducing the net charge on Au NPs. Importantly, the adjustment of the charges on Au NPs depends on the dielectric property of the surrounding medium.[213] The schematic diagram in **Figure 2.8(b)** and the corresponding green line in **Figure 2.8(a)** help in explaining this situation. The TEM characterization in Figure 2.4(b) has already confirmed that a chain formation of Au NPs takes place after the attachment of DTSP on Au NPs due to the reduction in the interparticle distance. The scheme suggests that, under the normal electromagnetic irradiation, a weak attractive force is generated between every pair of

DTSP–Au NPs owing to the aforesaid polarization effects. Subsequently, the attractive force between DTSP–Au NPs weakens the existing repulsive interaction between the particles causing the chain formation.[214] As a combined effect of dielectric charge compensation and dipole–dipole interaction, the resonance frequency of the Au NPs reduces and causes a red shift of the plasmonic oscillation. Moreover, the nucleation of the Au NPs collectively lessens the effective number of particles, and in turn lowers the absorbance of the DTSP–Au NPs solution.

Further, on the addition of Ab on the DTSP–Au NPs solution, no significant change in the wavelength and absorbance is observed. The TEM characterization in **Figure 2.8(b)** shows the further agglomeration of the chains during such a process. Thus, it can be anticipated that the addition of Ab does not bring much change in the interparticle distance of the Au NPs. On the addition of NCB–Ag protein to Ab–DTSP–Au NPs, a blue shift of the plasmonic peak is observed, as shown in **Figure 2.8(a)**. The interaction between Ab and NCB–Ag causes the accumulation of charges from the surrounding protein on the Au NPs surface, and eventually reduces the compensation effect due to the mutual polarization of Au NPs and the interfaced medium. Subsequently, the charge distribution of two interacting Au NPs cooperatively enhances the repulsive forces[214] causing increase in the interparticle distance and fragmentation of the chain. The TEM characterization in **Figure 2.8(c)** shows the fragmentation of the agglomerated chains leading to many islands of Au NPs during such a process. These effects mutually shift the resonant frequency of oscillation of the charges on Au NPs towards a lower wavelength causing a blue shift, as shown in **Figure 2.8(c)** and by blue line in the absorbance spectra in **Figure 2.8(a)**. The breakdown in the chaining of the particles increases the effective number of particles in the solution, and in turn enhances the absorbance of the plasmonic peak.

Figure 2.9 shows the variations in the peak position and intensity of absorbance with the loading of different volumes of urine samples of CaCx patients. In this case, the Ab solution (60 µL) has been added to a diluted solution of DTSP–Au NPs (2.5 mL) to obtain the Ab–DTSP–Au NPs solution. Further to this, different volumes of urine collected from a CaCx patient have been added and the UV–Vis spectroscopic spectra are recorded. **Figure 2.9(a)** shows the UV–Vis spectroscopic absorbance spectra after the addition of the urine sample (100 µL) to the Ab–DTSP–Au NPs solution indicating a prominent blue shift with a significant increase in absorbance, confirming the attachment of NCB–Ag in the urine sample with the Ab–DTSP–Au NPs. **Figure 2.9(b)** shows the variation in the absorbance intensity and the subsequent blue shifts ($\Delta\lambda$) with progressive addition of different volumes of the urine sample (20 µL to 420 µL) of CaCx patients. The experiment suggests that as long as the unbound paratope sites on the Ab are available, the epitope of NCB–Ag selectively binds to the same

via a very specific lock and key mechanism. Any noticeable shift has not been observed after the addition of 420 µL, which indicates the saturation in the attachment of NCB–Ag from the urine sample of the CaCx patient to the Ab–DTSP–Au NPs.

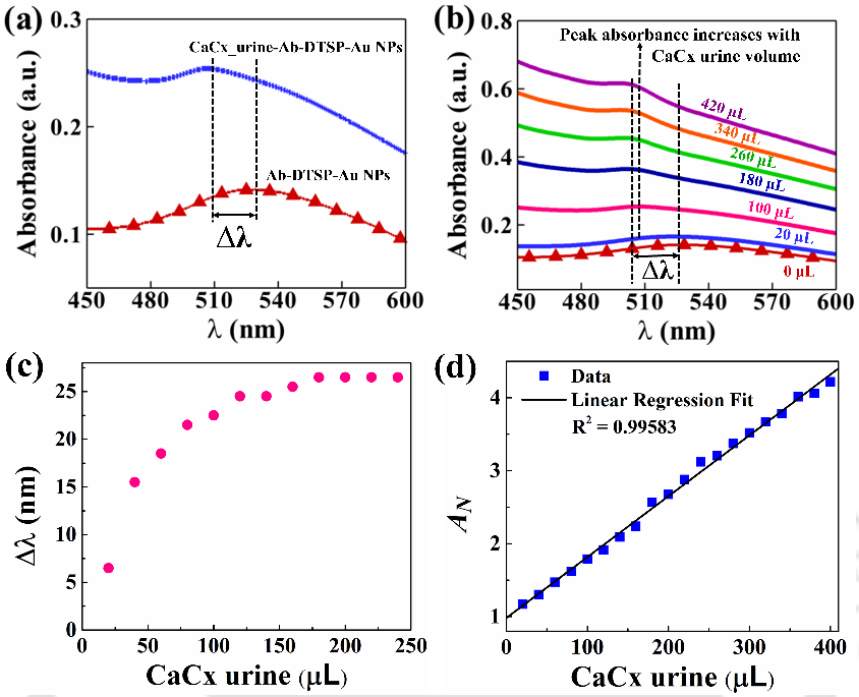

Figure 2.9. Plot (a) shows UV-Vis spectra of Ab–DTSP–Au NPs and after the attachment of NCB–Ag present in the urine sample of CaCx patient to Ab–DTSP–Au NPs. Plot (b) shows the change of UV-Vis absorbance along with gradual blue shifts of spectra on successive additions of CaCx urine with respect to Ab–DTSP–Au NPs. Plot (c) shows the change in the wavelength, $\Delta\lambda$ – blue shift, and (d) shows the change in intensity of absorbance on addition of different volumes of urine samples of a CaCx patient.

It may be noted here that the concentration of protein present in a urine sample of a CaCx patient may vary with stages of CaCx, water intake by the patient, time of sample collection, and other physiological issues. Further, the separation of different concentrations of NCB–Ag from different urine samples is a time consuming and costly process. Due to these complexities, different volumes of a CaCx urine sample have been used to observe the trend in the increase in the intensity of absorbance and corresponding blue shift of wavelength for the increasing concentration of NCB–Ag. The hypothesis here is that the concentration of the NCB–Ag present is expected to increase proportionately with the increase in CaCx urine volume. **Figures 2.9(c)** and **Figure 2.9(d)** show the change in wavelength shift ($\Delta\lambda$) and UV–Vis normalized absorbance (A_N), respectively, on the addition of different volumes of the urine sample into the Ab–DTSP–Au NPs solution. Here the parameter A_N is evaluated by eq (2.1)

$$A_N = \frac{|A_{No} - A_{Ni}|}{A_{No}} \tag{2.1}$$

where A_{No} represents the UV–Vis spectroscopic absorbance of the Ab–DTSP–Au NPs solution and A_{Ni} represents the UV–Vis spectroscopic absorbance observed immediately after the addition of the respective volume of CaCx urine sample to the Ab–DTSP–Au NPs solution. In this experiment, the addition of the volume of a particular cervical cancer affected patient's urine sample has been increased gradually (20 to 400 µL in steps of 20 µL) into diluted Ab–DTSP–Au NPs (2.5 mL) solution. The plots 2.9(c) and 2.9(d) indicate that until the addition of 180 µL of urine, both the A_N and $\Delta\lambda$ was increasing. However, on subsequent addition of urine, only the A_N increase while the value of $\Delta\lambda$ shows no significant variation. Concisely, the experiments confirm that such variations in $\Delta\lambda$ and A_N can be employed as the sensing principle for the detection of CaCx from the patient's urine samples. Moreover, the linear regression fit in **Figure 2.9(d)** shows a good coefficient of determination, $R^2 = 0.99583$, which indicate a strong linear correlation between the change in the A_N with the change in the concentration of the targeted protein present in different volume of the urine sample, considered for the study. Owing to the good linear fit of the regression model, the limit of detection (LOD) of the system was found to be ~ 6.5 µL obtained by eq (2.2), which indicates that the proposed biosensing technique is capable to show change in A_N to even minute amount of antigen presents in ~ 6.5 µL of the urine sample.

$$LOD = \frac{3.3 \times \sigma_{blank}}{Slope} \tag{2.2}$$

where σ_{blank} is the standard deviation of the blank sample and slope is obtained from the calibration curve shown in **Figure 2.9(d)**. Herein, the plots in Figure 2.9(c) and Fig. 2.9(d) were obtained by employing only one cervical cancer affected patient's urine sample. Owing to limited multiple availability of the same patient's urine sample, no error bars were marked. However, it is to be noted that similar observations were observed for multiple patients' urine sample as reported further in Figure 2.11 later. Based on all the observations of the response of the biosensing technique as described above, strong linear regression data, and lower LOD values, we have further utilized the change in LSPR A_N in response to the targeted protein concentration in the urine sample as a potential tool for the detection of cervical cancer positive cases, as described later.

2.4.3. Interference study

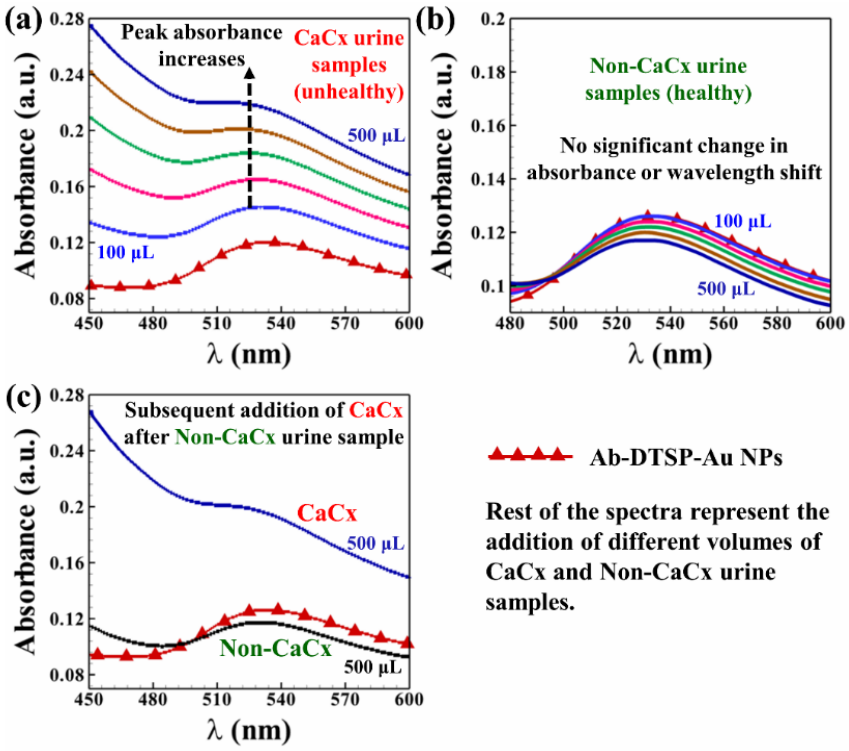

Figure 2.10: Plot (a) shows UV–Vis spectroscopic spectra of Ab–DTSP–Au NPs and after addition of different amounts urine samples of CaCx patient (other lines) to Ab–DTSP–Au NPs solution. Plot (b) shows UV–Vis spectroscopic spectra of Ab–DTSP–Au NPs solution and on addition of different amounts of healthy (Non–CaCx) urine sample (other lines) to Ab–DTSP–Au NPs solution. Plot (c) shows the UV–Vis response of Ab–DTSP–Au NPs solution and the change in intensity of absorbance on the addition of 500 µL of healthy patient's urine sample (black solid line) and subsequent addition of 500 µL of CaCx patient's urine sample (blue solid line).

An interference study has also been performed to validate the specificity of the binding affinity of NCB–Ag present in the CaCx urine samples with Ab–DTSP–Au NPs, for both positive and negative CaCx cases. In this study, the interaction of the Ab–DTSP–Au NPs sensor with the healthy urine samples has been checked. Here, a healthy urine sample means the urine sample that does not contain any NCB–Ag but contains all other urine constituents. **Figure 2.10(a)** shows the UV–Vis spectroscopic spectra for the interaction of NCB–Ag present in different volumes of CaCx positive patient's urine sample with Ab–DTSP–Au NPs. A progressive increase in the intensity of absorbance with concurrent blue shift of the peak confirms the attachment of NCB–Ag to Ab–DTSP–Au NPs after the addition of different volumes of CaCx urine sample to the Ab–DTSP–Au NPs solution. On the other hand, **Figure 2.10(b)** shows no such trend on the addition of different volumes of healthy (Non–CaCx) patient's urine sample to Ab–DTSP–Au NPs solution. It can be inferred from the plot that the intensity of absorbance reduces only marginally alongside the absence of the blue-shift of the

peak. The reason for such observation is the absence of NCB–Ag in the healthy patient's urine sample, which causes no interaction between NCB–Ag and Ab–DTSP–Au NPs.

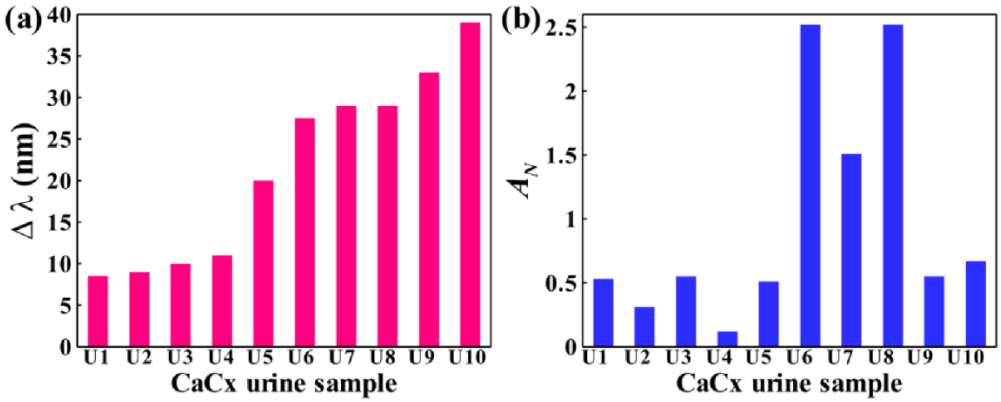

Figure 2.11: Plot (a) shows the $\Delta\lambda$ of the UV–Vis spectroscopic spectra observed after the addition of ten different urine samples of CaCx patients into the Ab–DTSP–Au NPs solution. Plot (b) shows the variations in the normalized peak intensity (A_N) of absorbance of the UV–Vis spectroscopic spectra after the addition of urine samples of ten different CaCx patients to the Ab–DTSP–Au NPs solution.

The experiments with the healthy urine sample also prove the specificity of the NCB-Ag towards anti–NCB Ab in the presence of a mixture of various other proteins, normally present in any urine sample. **Figure 2.10(c)** shows the change in the UV–Vis spectroscopic spectra of the Ab–DTSP–Au NPs solution after the sequential addition of, initially the healthy patient's urine sample (500 μL), followed by, the addition of CaCx patient's urine samples (500 μL). Again, the plot confirms a significant blue-shift of the peak and increase in the intensity of absorbance only after the addition of NCB–Ag loaded urine samples from CaCx patient. The experiments help in concluding that the proposed technique can faithfully identify CaCx patients non-invasively from the urine sample.

The authenticity of the proposed sensing technique has further been verified with the urine samples from a set of ten different CaCx patients (U1–U10). **Figure 2.11** shows that in all the ten cases, both the blue–shift and the variation in the intensity of absorbance of the UV–Vis spectra have been apparent after the addition of the said NCB–Ag marker to Ab–DTSP–Au NPs solution. **Figure 2.11(a)** shows $\Delta\lambda$ obtained while **Figure 2.11(b)** shows the corresponding change in the normalized peak intensity of absorbance, A_N, after the addition of ten different CaCx urine samples. The plot depicts that the magnitude of $\Delta\lambda$ and A_N are different for different CaCx affected urine samples. It probably is due to the presence of different quantities of NCB–Ag in the different samples owing to different stages of CaCx.

2.4.4. POCT for CaCx screening

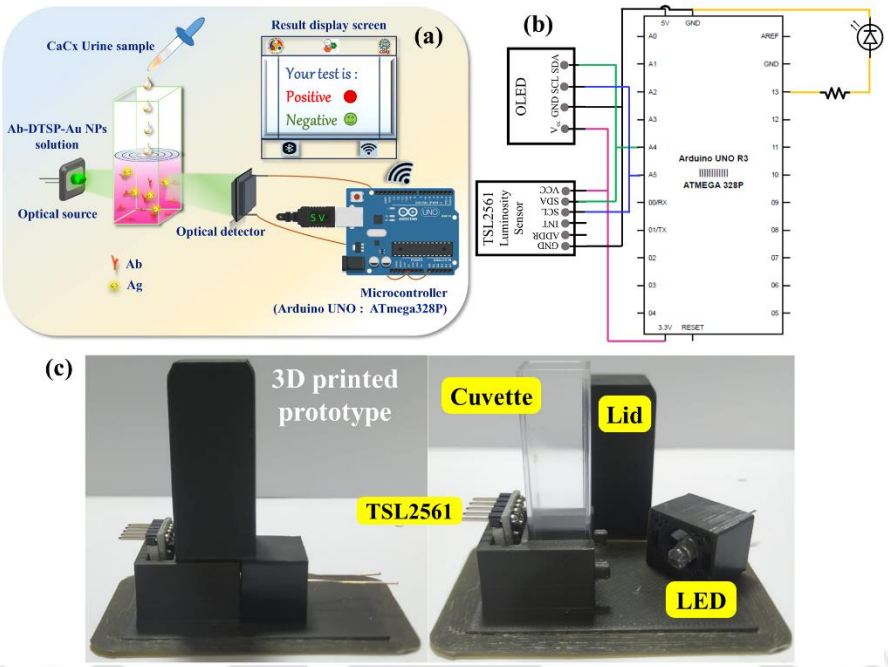

Figure 2.12: Shows the (a) schematic diagram of the portable POC prototype for non–invasive CaCx identification from urine samples, (b) circuit diagram of the POCT device for CaCx screening, and (c) 3D printed prototype of the developed POCT.

Based on the results discussed up to this point, an electronic transduction setup has been developed for POCT for screening CaCx. The electronic arrangement comprises an optical source of decisive wavelength for illuminating the sensor, a socket for keeping a cuvette filled with the Ab–DTSP–Au NPs solution, a luminosity sensor (TSL2561) with built-in analog to digital converter (ADC). **Figure 2.12(a)** shows the entire arrangement of the portable proof–of–concept prototype. The electronic circuitry contains an Arduino UNO board for processing the incoming data, and an Organic Light Emitting Diode (OLED) display the results of the test. The circuit diagram of the arrangement of the prototype is shown in **Figure 2.12(b)**. **Figure 2.12(c)** shows the image of the 3D printed prototype of the developed POCT labelled with different parts of the device.

In this prototype, a high intensity green-colored light-emitting diode (LED) with a narrow wavelength range, ~ 515–540 nm, has been used as the optical source. The use of this light source with a specific wavelength eliminates the interference of other wavelengths of light to allow a noise–free absorbance signal at around 523 nm of the Au NPs, before and after attachments of NCB–Ag. Thus, the narrowing of the wavelength of inspection gives the opportunity to assess the intensity of absorbance in that range owing to the interaction of NCB and Ab as a measure to check the positivity or negativity of the provided urine sample to CaCx. Inside the sensor embodiment, the incoming light with a specific wavelength has been allowed

to pass through a cuvette of 1 cm × 1 cm filled in with the Ab–DTSP–Au NPs solution. After the addition of NCB–Ag loaded urine sample of CaCx patients, a part of the incoming light is absorbed by the sensor while the rest of the transmitted light has been collected in the photodetector unit. It is to be noted here that the optical detector used is capable of irradiance measurement (make: Adafruit, model: TSL2561), which has a silicon photodiode of spectral range 400 nm to 800 nm for visible light recognition and effective 20–bit dynamic range suitable for explicit measurement of the intensity of absorbance in the specified wavelength range. The apparatus is packaged inside a 3D printed black Polylactic Acid (PLA) box to minimize stray light and ensure fixed optical distance between the source and detector.

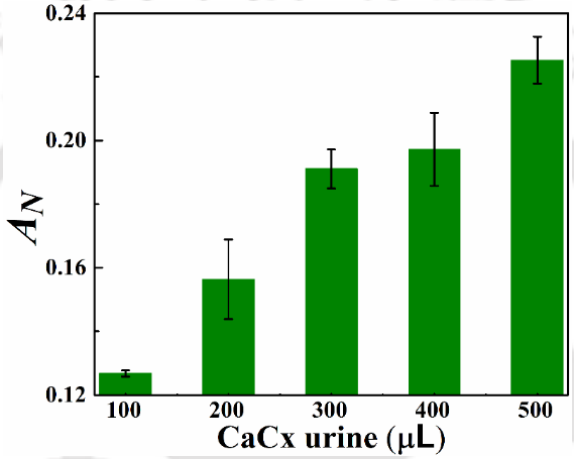

Figure 2.13: The results obtained from the proposed portable POCT device for CaCx identification in urine samples.

The interaction of the analyte with the sensor increases the absorbance, which is then transduced into electrical signal by the integrated photodiode. The signal is digitized with 16-bit resolution and transmitted to Arduino UNO microcontroller which is programmed to process the signal, decide whether the analyte is positive or negative to CaCx, and display the result on an OLED display. **Figure 2.13** shows the change in the normalized absorbance (A_N) obtained from the proposed portable POCT prototype for the addition of 100 µL, 200 µL, 300 µL, 400 µL, and 500 µL of a urine sample of a CaCx patient to Ab-DTSP-Au NPs solution. The parameter A_N is evaluated similarly as described before in eq (2.1). Interestingly, a progressive increase in the absorbance value has been observed with increasing volume of urine of CaCx affected patients, consistent with the UV–Vis spectroscopic spectra observed in Figure 2.9. The results confirm that the proposed portable POCT prototype is proficient enough in the screening of CaCx from healthy patients, non-invasively from the urine sample of the patients, unlike the conventional CaCx screening methodologies where the cytology–based investigation is required for the identification of abnormal cells.

2.5. Conclusions

The research work showcases the development of a POCT device from establishing a sensing principle to the prototype development for hassle–free, economical, and robust screening of cervical cancer following a non–invasive pathway. For this purpose, a cervical cancer specific urinal protein, PP1Ƴ2, has been identified as a specific biomarker. Conventional RT–PCR and WB analyses confirm the presence of this protein biomarker at different concentrations in the urine samples of patients.

Further, for the development of the POCT device for this biomarker, plasmonic Au NPs have been immobilized with the anti–PP1Ƴ2 antibodies, grown in rabbit. On the addition of the patient's urine sample containing NCB–Ag, the modified Au NPs undergo a significant blue shift with concurrent increase in the absorbance of the LSPR, which hints towards the capacity of the proposed methodology in selectively identifying the different stages of cervical cancer.

An interference study with healthy urine samples ensures the specificity of the proposed plasmonic detection, which has further been verified by the experimentation with different patient samples. A proof–of–concept portable prototype is developed exploiting a decisive wavelength (~540 nm) optical source and a sensitive photodiode, to trace the variation in the LSPR signal with the addition of NCB–Ag.

Concisely, the proposed methodology paves a painless, non-invasive, and early screening of cervical cancer at patients' sites, without physical contact with the patient. The proposed concept can stand as a game–changer in the field of medical science for the early screening of cancer biomarkers in urinal proteins.

भारतीय प्रौद्योगिकी संस्थान गुवाहाटी
Indian Institute of Technology Guwahati

Chapter 3

Point–of–Care Biosensing of UTI Employing Optoplasmonic Surfaces Embedded with Metal Nanotwins

ABSTRACT

We report the synthesis of gold nanotwins (Au NTs) on a solid and transparent glass substrate which in turn has been employed for the selective optoplasmonic detection of *Escherichia coli* (EC) bacteria in human urine for the point-of-care diagnosis of urinary tract infection (UTI). As compared to the single nanoparticle systems (Au NPs), the Au NTs show an enriched localized surface plasmon resonance (LSPR) due to the enhancement of the electric field under an electromagnetic irradiation, e.g., photon, which helps in improving the limit of detection. For this purpose, initially a simple glass surface has been coated with Au NPs, with the help of the linker 3-aminopropyl-triethoxysilane – APTES. The surface has further been linked with another Au NP with the help of 1,10-alkane-dithiol linker with two thiol ends, which eventually leading to the development of the optoplasmonic surface with Au NTs and enhanced LSPR response. Subsequently, EC specific aptamer has been chemically immobilized on the surface of Au NTs with the blocking of free sites via bovine serum albumin (BSA). Remarkably, the Raman spectroscopy has revealed a seven-fold increase in the peak intensities with the Au NTs on the glass surface as compared to the surface coated with isolated Au NPs. The enhancement in LSPR response of glass substrates coated with Au NTs and EC specific aptamer has been further utilized for the selective and sensitive detection of UTI. The results have been verified with the help of UV-visible spectroscopy to establish the utility of the proposed sensing methodology. An extensive interference study with other bacterial species unveils the selectivity and specificity of the proposed optoplasmonic sensors towards EC with a detection range of 5×10^3 to 10^7 CFU/mL. Intuitively, the method is more versatile in a sense that the sensor can be made specific to any other pathogens by simply changing the design of the aptamer. Finally, a low–cost, portable and point–of–care optoplasmonic transduction set up is designed with a laser light illumination source, a sample holder, and a sensitive photodetector for the detection of UTI in human urine.

3.1. Introduction

The novel physical properties of the noble metal nanostructures have fascinated the researchers for ages. In particular, the usage of the Localized Surface Plasmon Resonance (LSPR) effects of gold or silver nanoparticles originating from the interaction of the free electrons at the metal-dielectric interface with an incident electromagnetic irradiation[215] have been under the scanner for a while. Of late, this phenomenon has been widely exploited to develop high-precision colorimetric nanobiosensors with enhanced absorption[216], scattering[217], and electronic properties[218,219]. Subsequently, a host of prototypes and devices have been developed targeting diagnostics[220], therapeutics[221], optoelectronics[222], and spectroscopy[223,224]. The recent studies indicate that the LSPR of metal nanoparticles can be precisely modulated spanning the visible to the near infrared spectral range by controlling the size[225], surface anisotropy[146], composition[226], aggregation[227] and physical[228] or chemical[229,230] patterning of the surface[231]. Apart from structural alterations, the LSPR of nanostructures can also be modulated by the variation in the local dielectric environment surrounding medium[232], and it has been widely employed for the development of biosensors.

Importantly, a number of previous studies highlight that an array of nanotwins of noble metals is capable of generating significant localized electric field at the junction of their association by creating zones with "hotspots"[233,234]. These hotspots are created as a result of the plasmonic coupling (or constructive interference) of the each unit of the nanotwins, and eventually enhance the electric field as compared to an isolated nanostructure[235]. In a way, for such an assembled nanostructure, the enhancement or lowering of the resultant electric field under the exposure of an electromagnetic irradiation is decided by the inter particle gap. For example, a pair of nanostructures far from each other behave very similar to an individual nanostructure. On the other hand, when the gap between the twins is near a critical threshold (e.g. ~1 nm)[235], a field enhancement as high as 10^7-10^8 is observed. However, when the gap decreases further to enter into quantum regime[235] of < 1 nm, the resultant electric field diminishes as a result of the tunneling of the electrons directly from one nanostructure to other, disrupting the localization of the electrons required to form the hot spots. Thus far, the synthesis of such nanotwins with a very specific gap between them and an enhanced LSPR response have been performed either by high-end lithography techniques[236], by precise chemical synthesis methods[235] or by DNA origami formulation[237]. A host of recent studies uncover that an array of nanotwins generating localized hotspots of LSPR can be widely employed for high resolution biomedical imaging[238], biosensing[239,240], and single molecule detection[241].

It is also important to note here that, in the post n-COV pandemic era, the diagnostics have slowly started shifting from the pathological laboratory to the patients' site in the form of the point-of-care-testing (POCT) devices[242,243]. In this direction, a specific, sensitive, low-cost and accurate detection of various pathogens is one of the important areas for the early identification of various healthcare associated infections (HAIs)[244]. In this regard, urinary tract infections (UTIs) have been among the very common HAIs, and account for ~35-45% of all the HAIs reported in India. UTI is a medical condition in which microorganisms like bacteria grow and multiply in the urinary tract to create infections in the internal organs like kidney, ureter, urinary bladder and urethra. In the severe cases, the concerned bacterium can be found in the bloodstream also, thus affecting the upper body organs. The common pathogens that cause UTI are *Escherichia coli* (EC), *Klebsiella spp., Proteus spp., Enterococci spp., Pseudomonas aeruginosa, Serratia marcescens, Candida spp., Staph. Aureus, Staph. Epidermidis*, with EC accounts for more than 50% of the cases[245]. Diagnosis of UTI is based on the clinical symptoms of fever, suprapubic pain, frequency of urination, dysuria, urination with dark color, cloudy urine appearance, presence of blood or foul smell and presence of bacteria in the urine in significant amount marked as the number greater than 10^5 CFU/mL for any of the bacterium enlisted above[246,247]. Although UTI can affect both males and females[248], the infection risk is higher in women because the urethra in females is shorter and closer to the anus, where the concentration of pathogens are on the higher side[249]. In addition, a large number of recurrences has also been reported in the premenopausal and postmenopausal women as a result of declined oestrogen levels and vaginal atrophy[250]. Along with these, one of the major causes of the UTI infection is the presence of catheter in the urinary tract, normally in the hospitalized patients[251].

As of today, a number of conventional diagnosis methods are available for the detection of UTI, of which bacterial culture of the urine sample at microbiology department in a hospital is considered to be the most reliable technique of identification of the disease[252]. However, it takes a long time of three days for the confirmatory test of the patient sample. Another test used in the pathological laboratories is the microscopy test, which visually identifies the presence of any bacteria by gram staining of the microorganism present but it lacks in identifying the species of the bacteria[253]. The nitrate test using urinalysis dipsticks is a rapid test and is an indirect test to detect the presence of any microorganism in the urine sample and thus does not reveal the identity of the microorganism present[254]. The frequent recurrence of the UTI in a patient is diagnosed by imaging the urinary tract using ultrasonography, a computerized tomography (CT) scan or magnetic resonance imaging (MRI)[255]. Another method used for

imaging severe infection is cystoscopy, where a thin tube with camera and light on the end is inserted into the urethra to the urinary bladder to diagnose the extent of infection[256].

Prior-arts suggest that, previously, a number of attempts have been made to develop POCT devices for the diagnosis of UTI targeting bacteria[257-260] detection. For example, Plasmonic gold nanoparticles (Au NPs) have been used for the naked eye detection of EC for UTI by controlled aggregation of the nanoparticles[261]. In another approach, a smartphone based platform has been developed for the detection of five UTI pathogens applying Au NPs[262]. Likewise, gold nanoclusters have also been employed the detection of pathogenic bacteria via Plasmon enhanced fluorescence[263]. In another study, antibody linked Au NPs have been applied for the designing of an origami platform for the facile detection of bacterial infection[264]. Apart of nanoparticle based detection, various nanostructured SERS substrates has also been studied for the diagnosis of UTI targeting both bacterial[258,265-267] and genomic[268,269] detection pathways. However, very minimal focus has been made towards the pathogen detection targeting UTI based on optoplasmonic metal nanotwins.

In view of the background, the present work reports the development of an optoplasmonic nanobiosensors for the POC detection of UTI in human urine. For this purpose, initially we employ a chemical synthesis method wherein a solid and transparent optoplasmonic substrate composed of a glass surface has been coated with an array of Au NP nanotwins – Au NTs, having a very specific 'gap' between the twin NPs with the help of the dithiol linkers. The glass surface with a Plasmonic response is then functionalized with the oligonucleotides with specific capture capabilities of MTCC–42 species of EC. The optoplasmonic surfaces thus prepared are then employed for the detection of different concentrations of EC in both aqueous and urine samples. The attachment of the pathogens on the optoplasmonic surface leads to the deviation in the LSPR response of which in turn has been correlated to the concentration of the pathogens present in the analyte. Subsequently, a proof-of-concept POCT prototype has been developed by integrating the optoplasmonic sensor with a plane polarized optical source on one side and a visible spectral photodetector to the other in a transmission mode. The setup helps in transducing the variations in the LSPR response due to the change in the local refractive index of the optoplasmonic surface with the attachment of the pathogens. Concisely, the methodology reported here elucidates an accurate, specific, portable, economic, and high-precision methodology for the real–time POCT of UTI at the patients' site. The proposed methodology is more versatile in a sense that the sensor can be made specific to any other pathogens by simply changing the design of the aptamer.

3.2. Materials and methods

3.2.1 Materials

Analytical grade acetone, ethanol, ammonium hydroxide, hydrogen peroxide, gold (III) chloride, tris (2–carboxyethyl) phosphine (TCEP), trisodium citrate, tris–HCl buffer, tris–EDTA (TE) buffer, (3-Aminopropyl) triethoxysilane (APTES), 1, 10–alkanedithiol (C_{10}), sodium hydroxide (NaOH) and bovine serum albumin (BSA) were procured from Sigma-Aldrich. Nuclease free (NF) water was purchased from HiMedia. All bacterial strains were Indian isolates, purchased from MTCC (Microbial Type Culture Collection), Chandigarh, India. Molecular grade Luria Bertani broth, Miller (REF M1245–500G; LOT 0000459138), agar powder of bacteriological drade (REF GRM026-500G; LOT 0000361577) were purchased from HiMedia. 5'–Thiolated DNA Aptamers were procured from IDT (Integrated DNA Technologies, USA).

3.2.2 Methods

I. Pre-cleaning of glass

Glass substrates were first cut into small slices of ~ 0.9 cm × 2 cm size. All the sliced glass substrates were first soaked into soap solution for ~30 min, then sonicated for next ~30 min and washed thoroughly with distilled water for 4–5 times. After that, the sliced glass substrates were then dipped in acetone at 70˚ C for ~15 min. The acetone treated glass slices were then transferred to ethanol solution and kept at 80˚C for ~15 min and washed thoroughly with distilled water for 3–4 times. The cleaned glass slices were then dipped into a pre-heated mixture of 5:1:1 of distilled water, 27% ammonium hydroxide, 30% hydrogen peroxide at 80˚ C for ~30 min or until the bubbles vanished. Finally, the glass slides were washed with DI water for 5 times and stored in a closed vessel containing DI water for further use.

II. Preparation of samples and solutions

The lyophilized DNA aptamer was reconstituted in NF water to the final concentration of 100 µM and was stored at -20°C. The 70 bases ssDNA library contained 36 randomized bases (N36) flanked by 17 bases primer binding sites (PBS). Aptamers were further diluted in binding buffer (TE buffer) to prepare the working solution of 1 µM.

The working solution of 100 µM of tris (2–carboxyethyl) phosphine (TCEP) was prepared in Tris–HCl buffer. Further, the working solution of tris–HCl buffer used was 20 mM prepared in NF water. The working solution of tris–EDTA (TE) used was 1X, prepared using NF water.

The working solution of gold (III) chloride was made to 0.25 mM using NF water while the same for trisodium citrate was made to 38.8 mM using NF water. Gold nanoparticles were prepared according to procedure reported elsewhere[149]. Briefly, 10 mL of the working solution

of gold (III) chloride solution was heated at 120°C to bring to boil. After that the solution was stirred at 1030 rpm and subsequently 1 mL of the working solution of tri-sodium citrate was added and stirred for another ~30 min with heating. When the color of the solution turns wine red, the heating was switched off and the solution was left to cool with stirring. The solution was then stored at 4°C for further use. Thereafter, the working solution of 3–aminopropyl triethoxysilane (APTES) is then made to 0.5% using NF water while the same for 1, 10–alkanedithiol (C_{10}) was made to 1 mM using ethanol. The solution of bovine serum albumin (BSA) used was 1 mg/mL, prepared in NF water.

All bacterial strains in the present invention were Indian isolates, purchased from MTCC (Microbial Type Culture Collection), Chandigarh, India and were used as target cells for ssDNA aptamer selection by cell-SELEX. All bacterial strains *Escherichia coli* (MTCC–42), *Enterococcus faecalis* (MTCC–3159), *Klebsiella pneumoniae* (MTCC–7028) and *Streptococcus aureus* (MTCC–9542) were grown in Luria-Bertani (LB) medium at 37°C to an OD_{600} of 0.4 (equivalent to ~10^8 cells/ml). For bacterial binding/testing assay development, cells were centrifuged at 8000 rpm for 3 min and washed twice with 1X PBS and re-suspended in assay buffer.

3.2.3. Preparation of sensor

I. Immobilization of isolated gold nanoparticles (Au NP) on glass substrate

In order to prepare Au NP coated glass substrate, the previously cleaned glass substrates were first immersed into 0.5% aqueous solution of APTES and kept at 60˚C for ~1 h. The APTES coated glass substrates were then washed with DI water two times and then sonicated in DI water for ~5 min. After that, the sonicated APTES coated glass substrates were cleaned thoroughly with ample DI water and dipped into the 1:5 dilute solution of prepared Au NP for ~ 6 h. The Au NP coated glass substrates were then washed properly with sufficient DI water for 5 times and stored for further use.

II. Synthesis of gold nanotwins (Au NTs) on glass substrate

In order to prepare Au NTs on the glass substrates, the Au NP coated glass substrates were dipped into 1 mM solution of C_{10} for ~ 1 h after washing once with ethanol. Thereafter, the C_{10} immobilized Au NP coated glass substrates were washed thoroughly with DI water for at least 8 times and then dipped in 1 mM solution of NaOH for ~ 4 h to remove the base APTES left after the attachment of Au NPs. The NaOH treated glass substrates were then washed properly with DI for 5 times and again dipped in 1:5 diluted solution of Au NP for ~ 12 h to prepare Au NTs and then washed thrice with NF water for further attachment of Apt. The prepared Au NP and Au NT coated glass substrates were stored in NF water for further use.

3.2.4. Simulation framework

Near field enhancement of the isolated and dimeric gold nanoparticles has been simulated using finite element analysis tool of COMSOL Multiphysics™ 5.5. COMSOL Multiphysics is based on Finite Element Method (FEM). Like other numerical schemes, FEM is deployed to solve complex engineering problem that involves coupled physics and spans over irregular spatial region. COMSOL Multiphysics provides physics based default meshing option, wherein a preset algorithm is used for creating unstructured grids that consisted of triangles, quadrilaterals, tetrahedral, hexahedral, and prisms shaped meshes. For this work, the physics based meshing option was considered with minimum and maximum mesh element size of 0.36 nm and 8.4 nm, respectively. For the solution, we employed available direct PARDISO (Parallel Direct Sparse Solver) solver with coupled physics wherein all the set of linear equations are solved with a standard non-iterative numerical scheme like Gaussian elimination or LU decomposition.

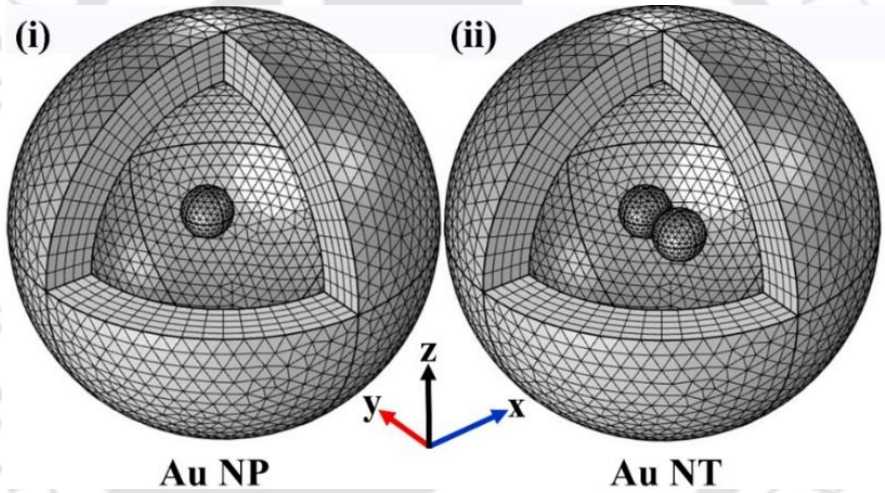

Figure 3.1: Shows the geometry of (i) Au NP and (ii) Au NT used in the simulation.

Boundary Conditions

For the present study, Electromagnetic wave frequency domain physics of Wave Optics module of COMSOL Multiphysics has been used. The isolated gold nanoparticles have been represented as one 3D sphere of 15 nm radius and the dimeric structure of gold nanoparticles has been represented as two 3D spheres of 15 nm radius with ~ 1.5 nm gap, as shown in **Figure 3.1**. An outer 3D sphere of 120 nm radius with 50 nm layer represents the perfectly matched layer (PML) used to truncate the physical domain and to avoid the internal reflections which represents the physical system in infinite space domain. The surrounding medium is taken as air and the gold material was taken from the material library considering experimental values

of Johnson and Christy. Here, the electromagnetic wave equation has been solved for scattered field, E_{sca} as given in eq (3.1).

$$\nabla \times \left[\frac{1}{\mu_r} \left(\nabla \times E_{sca} \right) \right] - k_0^2 \left[\varepsilon_r - \frac{j\sigma}{\omega \varepsilon_0} \right] E_{sca} = 0 \tag{3.1}$$

where, k_0 is the wavenumber in free space, μ_r is the relative permeability of the medium, ε_r is the relative permittivity of the medium, σ is the electrical conductivity, and ω is the angular frequency. A plane wave E_b, given in eq (3.2), polarized along *y*-axis and propagating along *z*-axis has been used for solving the scattered field of Maxwell's wave equations.

$$E_b = E_0 e^{-\frac{2\pi i}{\lambda} z} \hat{y} \tag{3.2}$$

where, E_0 is the amplitude of the incident electric field taken as 1 V/m, and λ is the wavelength which is taken as 532 nm in the present study.

3.3. Characterization

3.3.1. Instruments

For the present study, the instruments used were UV-Vis spectrophotometer (Shimadzu, UV–2600 230 V EN), field emission scanning electron microscopy (FESEM Sigma 300), transmission electron microscopy (TEM, JEOL, JEM 2100), Raman spectroscopy (Horiba Scientific, LabRAM HR Evolution), hot plate cum magnetic stirrer (Tarsons, Digital Spinot), weighing machine (Sartorius, BSA224S–CW), desiccator (Tarsons), vacuum pump (Toshmiwal), deep freezer (Haier), orbital incubator shaker (A.R ENTERPRISES, AR–109–1), laminar air flow (Cleanair CAH 900; CE 3199).

3.3.2. Characterization of Au NPs and Au NTs

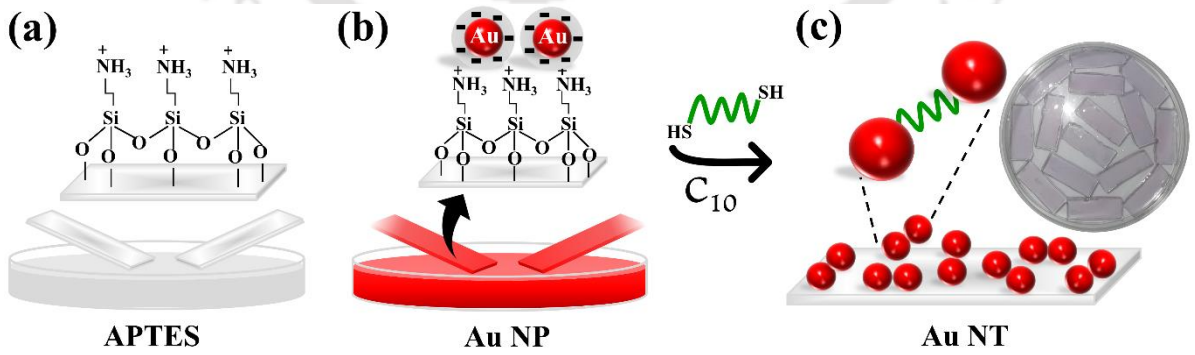

Figure 3.2: Schematic diagram of the preparation process of Au NP and Au NT coated glass substrates. Plot shows (a) APTES immobilized glass substrate, (b) Au NP coated glass substrate, and (c) Au NT coated glass substrate.

Figure 3.2 shows the schematic diagram of the preparation steps of the required glass substrates. **Figure 3.2(a)** shows the APTES coated glass substrate, **Figure 3.2(b)** shows the preparation of Au NP coated glass substrates and **Figure 3.2(c)** shows the further preparation

step for the synthesis of Au NT coated glass substrates. The inset of the figure shows the prepared Au NT coated glass substrate with a tinge of wine red coloration and adequate transparency. Importantly, it may be noted here that the same procedure can be utilized for the coatings of Au NTs on the flexible surfaces too such as polydimethylsiloxane (PDMS) polymer.

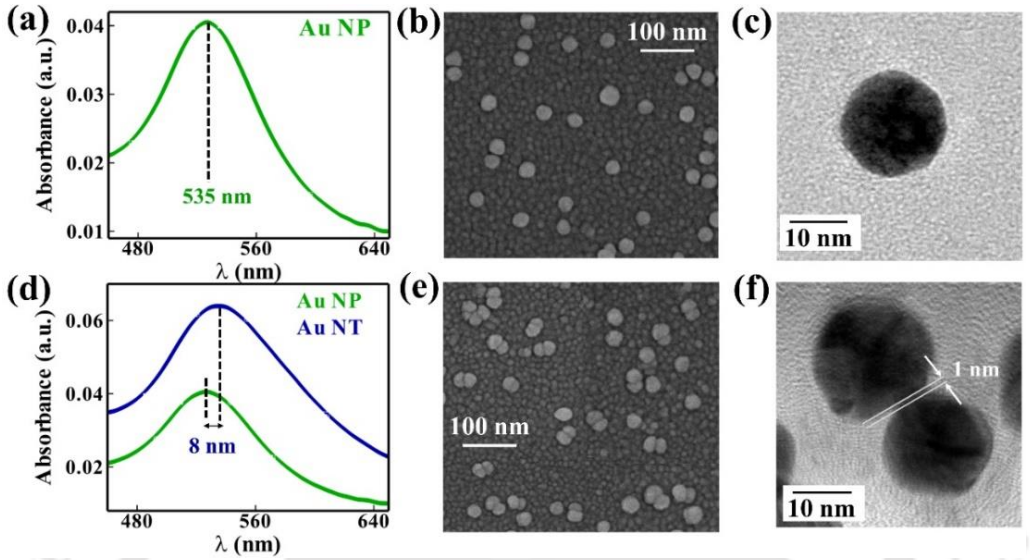

Figure 3.3: Plot (a) shows the UV–Vis spectroscopic spectrum for Au NP coated glass substrate, (b) shows FESEM image of the Au NP coated glass substrate and (c) shows the TEM image of the Au NP, (d) shows the shift in the UV–Vis spectrum after the formation of Au NTs. Plot (e) shows the FESEM image of the Au NT coated glass substrate and (f) shows the TEM characterization of the interparticle spacing between Au NTs.

The prepared glass substrates were characterized using UV–Vis spectroscopy, FESEM, and TEM and the results are shown in **Figure 3.3**. **Figure 3.3(a)** shows the UV–Vis characterization of the attachment of Au NP on the glass substrates. UV–Vis of the prepared glass substrates was obtained by immersing the required glass substrate in a cuvette filled with NF water with bare glass substrate immersed in NF water filled another cuvette as the reference. The UV–Vis spectrum shows the characteristic peak of gold nanoparticles at ~ 535 nm, which confirms the attachment of Au NP on glass substrate. **Figure 3.3(b)** shows the Au NP on the glass substrate, as obtained in FESEM which shows the distribution of isolated Au NP on the glass substrate. **Figure 3.3(c)** shows the TEM image of the prepared Au NP which shows that the size of the Au NP used is ~ 10–15 nm. **Figure 3.3(d)** shows the UV–Vis characterization of the glass substrates coated with the Au NTs. The figure shows the characteristic UV–Vis spectrum of the Au NP at ~ 535 nm, which confirms the attachment of the Au NPs on the glass substrate. Further, on the preparation of the Au NTs via C_{10} linking, the UV–Vis spectrum shows a red shift of 8 nm with increase in absorbance as a result of the controlled aggregation of two Au NP and enhanced plasmonic property of the Au NT coated glass substrate[270].

Figure 3.3(e) shows the FESEM image of the Au NT coated glass substrate. It could be noted that the FESEM image shows that the substrate also contains a few isolated Au NPs along with twinned ones, with the number of Au NTs higher than Au NPs. **Figure 3.3(f)** shows the TEM image of the Au NT structure as obtained by sonicating the Au NTs coated glass substrate in NF water for ~ 3 min. The figure shows the twinning of the Au NPs in the Au NTs. The figure also shows that the gap between the two Au NPs is ~ 1 nm, which lies in the classical regime of plasmonic enhancement[235].

3.3.3. Characterization of plasmonic property

The Plasmonic enhancement of the Au NP and Au NT coated glass substrates has been characterized by Surface Enhanced Raman Spectroscopy (SERS) technique, as shown in **Figure 3.4**. The Au NP and Au NT coated substrates were incubated with 10^{-6} M concentration of Rhodamine 6G (R6G) for ~ 12 h and then vacuum dried, before the SERS examination was performed.

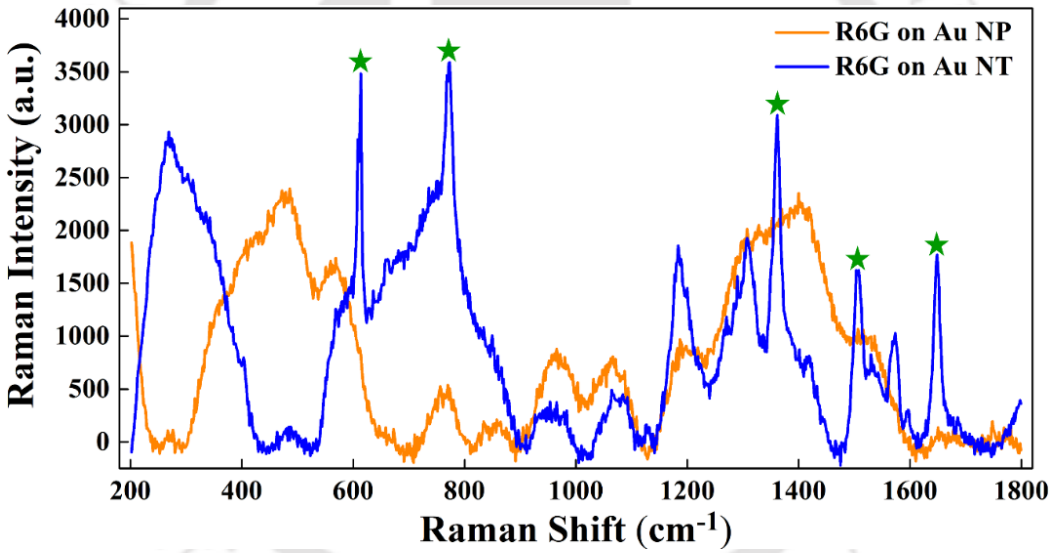

Figure 3.4: Plots comparing SERS enhancement of rhodamine 6G molecule adsorbed on Au NP (orange line) and on Au NT coated glass substrate (blue line).

Figure 3.4 shows the characteristic SERS spectra of the R6G adsorbed on Au NP (orange line) and on Au NT (blue line) coated glass substrates, respectively. The characteristic peaks of R6G observed are marked with asterisk[271] at C–C–C ring vibrations at ~ 661 cm^{-1}, C–H vibrations at ~773 cm^{-1}, and aromatic C–C stretching vibrations at ~1361, ~1509, and ~1647 cm^{-1}. Evidently, the characteristic spectral peaks of R6G were found to be more evolved in the Au NT coated glass substrate than in the Au NP one. The SERS enhancement factor ratio of Au NT to Au NP substrate at 773 cm^{-1} has been found to be ~ 7, which suggests that the Au NT coated glass substrate could show a seven-fold enhancement in the signals compared to Au

NP coated substrate. The experimental enhancement factor (EF_e) due to the SERS effect has been evaluated using equation eq (3.3)[271],

$$EF_e = \left(\frac{I_{SERS} \times C_{SERS}}{I_{RAMAN} \times C_{RAMAN}} \right) \tag{3.3}$$

Here, I_{SERS} and I_{RAMAN} are the signal intensities of SERS and Raman analysis, respectively and C_{SERS} and C_{RAMAN} are the concentration of R6G considered for the SERS and Raman study, respectively. As per the earlier reports[271], the plasmonic Au NTs are expected to generate augmented signals due to plasmonic coupling of similar Au NPs. Importantly, the plots also suggest that, apart from the enhancement in the Plasmonic signals, the peaks of R6G on Au NT coated glass substrate have been more prominent and sharper in compared with the Au NP coated glass substrate.

In order to further investigate on the phenomenon, we performed simulations with Au NP and Au NT, as shown in **Figure 3.5**. We solved the Maxwell's electromagnetic wave equation in commercial software, COMSOL Multiphysics™, considering spherical Au NP surrounded by air medium. The detailed description of the simulation is given in section 3.2.4. **Figure 3.5(a)** shows that the theoretical electric field enhancement factor – EF_t around the isolated Au NP is found to be in order of 10^2. Here, EF_t is calculated[272] using eq (3.4),

$$EF_t = \left(\frac{E_{\max}}{E_0} \right)^4 \tag{3.4}$$

where $E_{\max}$ is the maximum electric field obtained from the simulation, and E_0 is the applied electric field which is 1 V/m for the present study.

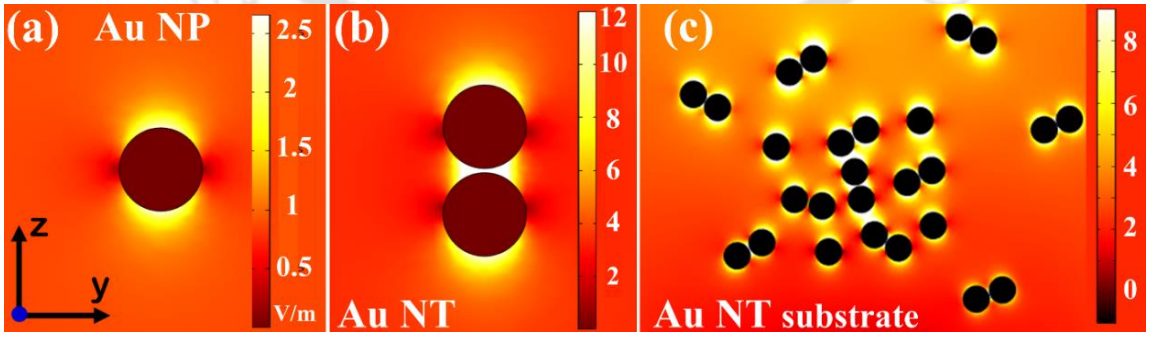

Figure 3.5: Shows the electric field enhancement obtained in COMSOL simulation for (a) Au NP, (b) Au NT, and (c) Au NT substrate.

Figure 3.5(b) shows that the EF_t found in Au NT is in order of 10^5, which is significantly higher than the EF_t of the isolated Au NP. In addition, it can be intuitively argued that, on the Au NT coated glass substrate, presence of randomly arranged numerous twins and isolated

nanoparticles (e.g., Figure 3.3(e)) could lead to mutual inter and intra particle coupling of the signals engendering the plasmonic enhancement observed during the experiments, as could be seen in **Figure 3.5(c)**. The **Figure 3.5** also suggests that the maximum electric field enhancement is at the gap between the Au NTs. However, when R6G is allowed to adsorb on the glass substrates, we expect that the molecules may spread uniformly throughout the substrate rather mounting specifically to the interparticle gap. Thus, experimentally the SERS enhancement could be less, as deduced from **Figure 3.4** and **Figure 3.5(c)**. Importantly, **Figure 3.4** shows that the Raman peaks of R6G adsorbed on Au NTs are significantly intensified as compared to Au NPs, and ascertains the potential of utilizing Au NTs for the detection of molecule or pathogens at a very low concentrations[241]. Thus, we carry forward an extensive study on the detection of MTCC–42 EC to diagnose UTI utilizing the aptamer specific to MTCC–42 EC immobilized on Au NT coated glass substrate.

3.3.4. Preparation and characterization of BSA–Apt–AuNP and BSA–Apt–AuNT substrates

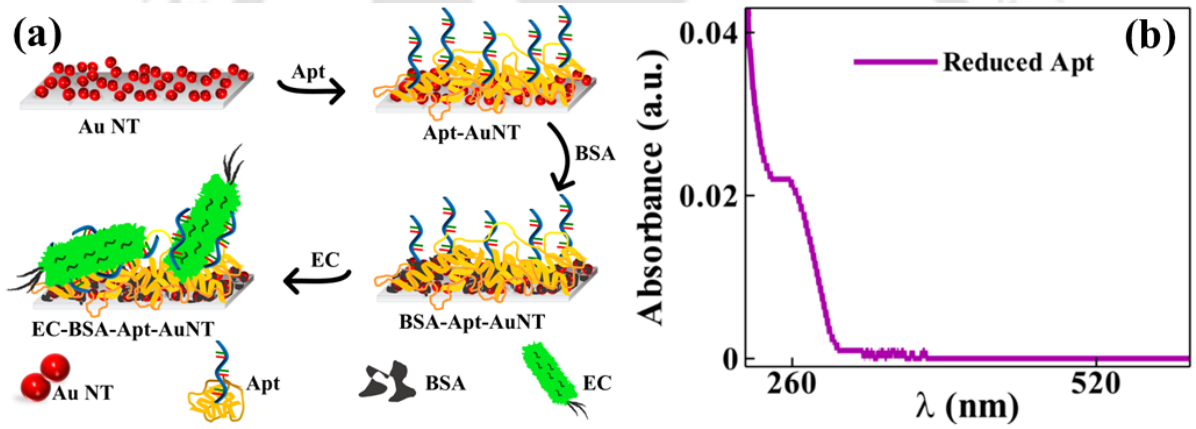

Figure 3.6: (a) Schematic representation of preparation of the Apt, and BSA immobilization steps for the synthesis of BSA–Apt–AuNT coated glass substrates and the attachment of EC on BSA–Apt–AuNT substrates, (b) UV–Vis spectroscopic characterization of reduced Apt.

Figure 3.6(a) schematically shows the steps of preparation of BSA–Apt–AuNT coated glass substrates for the detection of EC. Initially, the Au NT coated glass substrates were immobilized with aptamer (Apt) specific to EC. For this purpose, the purchased thiolated aptamer specific to MTCC–42 species of EC was reduced by mixing 50 µL of 1 µM aptamer solution with 50 µL of 100 µM TCEP solution and kept aside for ~ 2 h at room temperature, with gentle mixing in between. The reduction of the aptamer was confirmed by UV–Vis spectrophotometer, as shown in **Figure 3.6(b)**. The figure shows the UV-Vis spectra obtained by adding 100 µL of the TCEP–Apt mixture kept for 2 h in room temperature for reduction with NF water. The reduction of the aptamer was confirmed by the appearance of peak at ~ 260 nm, as reported elsewhere[273]. In order to attach the reduced Apt, 30 µL of the reduced

oligonucleotides were dropped on the required Au NT coated glass substrate and left undisturbed for ~17 h at room temperature to prepare Apt-AuNT substrates. Thereafter, the aptamer immobilized substrates were washed twice with NF water and stored in NF water for further use. The Apt–AuNT coated glass substrates were then dipped into 1 mg/mL solution of BSA for ~ 2 h to synthesize BSA–Apt–AuNT, which prevent any non-specific binding to the substrates during the experiments. These steps were repeated similarly for the preparation of BSA–Apt–AuNP substrates. The prepared BSA–Apt–AuNP and BSA–Apt–AuNT coated glass substrates were characterized step-by-step using UV-Visible spectroscopy and Raman spectroscopy as discussed in Figures 3.7 and Figure 3.8, respectively.

Figure 3.7(a) shows the UV–Vis spectrophotometric characterization of the Au NP coated glass substrate, immobilization of Apt on Au NP glass substrate and attachment of BSA on Apt–AuNP coated glass substrate. The figure shows the characteristic Au NP spectrum at ~525 nm, red shift of ~ 2 nm on the immobilization of Apt on the Au NP coated glass substrate[274] with further red shift of ~ 2 nm on the attachment of BSA[275] on Apt linked Au NP glass substrate, which confirms the synthesis of BSA–Apt–AuNP. Similarly, **Figure 3.7(b)** shows the UV–Vis spectra for the pristine Au NP at ~525 nm, red shift of ~8 nm on the formation of Au NTs, and subsequent red shift of ~ 3 nm and ~ 6 nm on the immobilization of Apt[274] and BSA[275], respectively, which confirms the synthesis of BSA–Apt–AuNT.

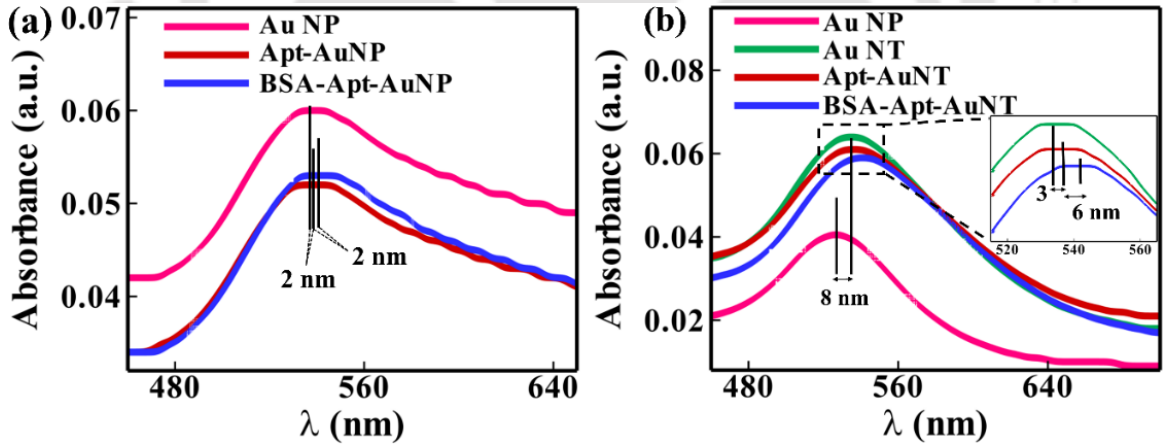

Figure 3.7: Shows UV–Vis spectroscopic characterization (a) BSA–Apt–AuNP, and (b) BSA–Apt–AuNT coated glass.

Further, the synthesis of BSA–Apt–AuNP and BSA–Apt–AuNT was characterized step-by-step using Raman Spectroscopy. **Figure 3.8** shows the characteristic Raman spectra obtained in various steps of synthesis. **Figure 3.8(a)** shows the Raman spectra for various step of Au NT synthesis via C_{10} linker. The Raman spectra of the pristine C_{10} linker shows the characteristic peaks[276] of trans vibration of –(C–S) at ~ 732 cm^{-1}, free –(S–H) group vibration at ~ 2570 cm^{-1}, gauche vibration of –(C–C) bond at ~ 1085 cm^{-1}, and the symmetric and

asymmetric vibrations of various –(C–H) bonds at ~ 1436 cm^{-1} and ~2800 – 3000 cm^{-1}. The bands can be significantly found in further steps, after the attachment of C_{10} to isolated Au NP (Au–C_{10}) and on subsequent attachment of second step of linking of Au NP (Au–C_{10}–Au) to form Au NT. Evidently, it can be realized from the figure that the intensity of the free –(S–H) group vibration band at ~ 2570 cm^{-1} is maximum for pristine C_{10} and it further decreases on the attachment of first (Au-C_{10}) and second (Au–C_{10}–Au) Au NP. This is due to decrease in the number of free –(S–H) group vibration bands on subsequent immobilization of Au NP. Thus, it shows the formation of the Au NT nanostructures.

Figure 3.8(b) shows the characterization of immobilization of (i) Apt on the surface of Au NP and attachment of (ii) BSA on Apt linked Au NP. The immobilization of Apt on Au NP is confirmed by marking the –(Au–S) bond at ~ 280-330 cm^{-1}, and other characteristic peaks of Apt[277,278] include: ring deformation of cytosine at ~ 600 cm^{-1}, antisymmetric stretching and vibrations of phosphate group ~ 1010-1089 cm^{-1} and –(N–C) vibration of adenine/guanine ~ 1305 cm^{-1}, ring modes of adenine/guanine at ~ 1320 cm^{-1}, backbone at ~ 1419 cm^{-1} , ring modes of thymine/cytosine at ~ 1575 cm^{-1} and –(C=O) stretching of thymine/ guanine/cytosine at ~ 1671 cm^{-1}. The attachment of BSA on the Apt–Au NP is confirmed by the spectra[279]: –(S–S) bridges at ~ 500-600 cm^{-1}, amide III bands at ~ 1200-1300 cm^{-1}, amide II at ~ 1550-1590 cm^{-1}, and amide I bands at ~ 1600-1700 cm^{-1}. The three different amide bands – amide I, amide II, and amide III signify the characteristic signature of different vibrations of bonds comprising the peptide[280].

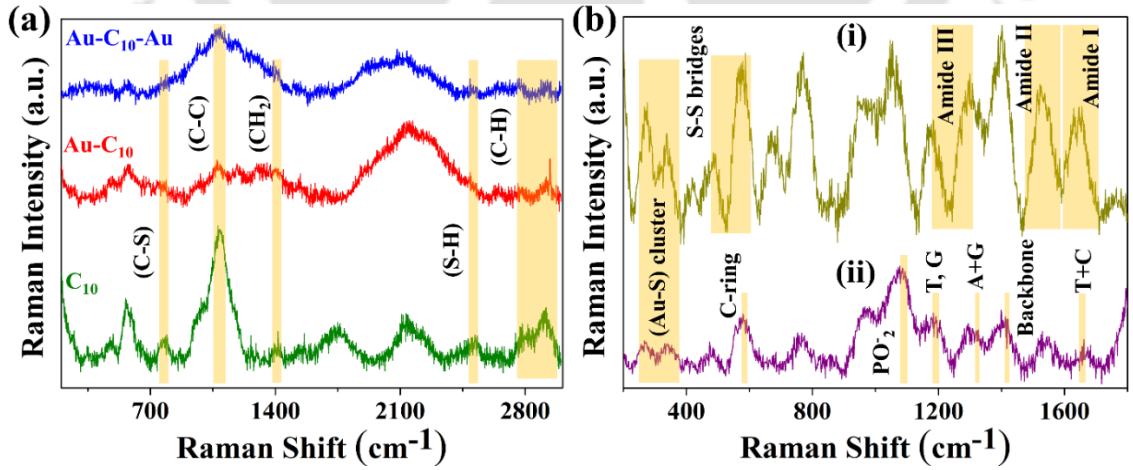

Figure 3.8: Shows Raman Spectroscopic characterization of (a) Au NT preparation, (b) immobilization of (i) Apt on Au NP and (ii) BSA on Apt attached Au NP substrates.

Amide I signifies the secondary structures of the peptide governed by the backbone conformation and the hydrogen bonding pattern. It is due to stretching vibrations of the C=O groups of the peptide. Amide II defines the parallel or antiparallel β- sheet structure of the peptide and is highly influenced by the side-chain vibrations. It is due to N–H bend and C–N

stretch. Amide III provides additional structural information to amide I like α-helix, random coil or β-sheet nature of the peptide. It is due to N–H bend and C–H stretch.

3.4. Results and Discussion

3.4.1. Utilization of plasmonic Au NT substrates for UTI detection

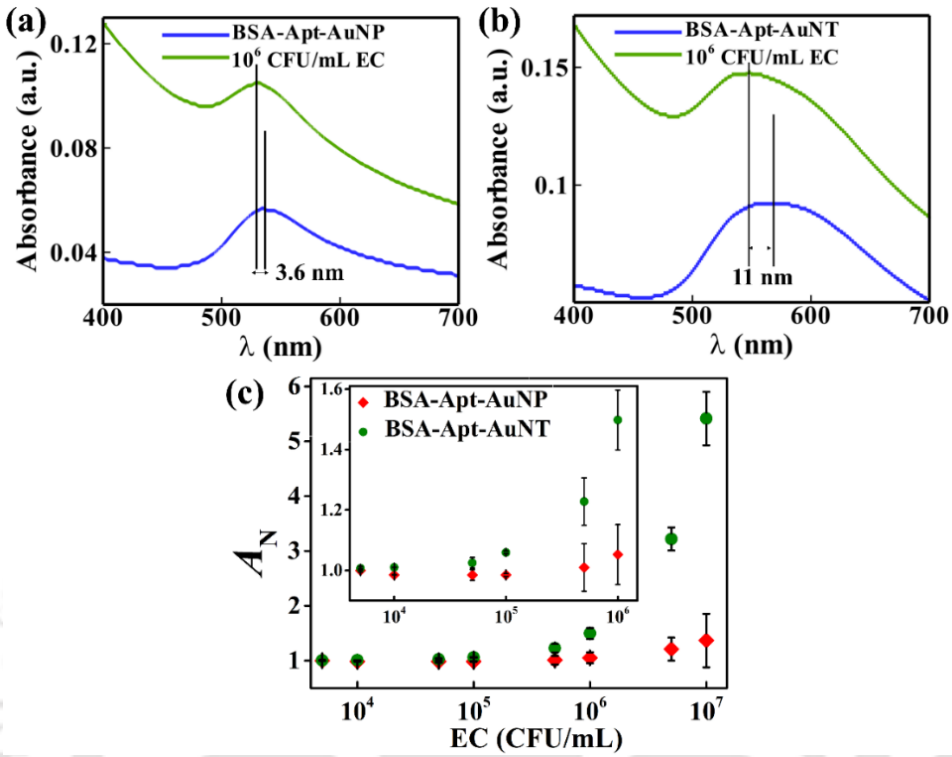

Figure 3.9: Plot show UV-Vis absorption spectra for the interaction of 10^6 CFU/mL EC with (a) BSA–Apt–AuNP, and (b) BSA–Apt–AuNT. Plot (c) shows the calibration curve for the interaction of various concentrations of EC–10^7 CFU/mL, 5×10^6 CFU/mL, 10^6 CFU/mL, 5×10^5 CFU/mL, 10^5 CFU/mL, 5×10^4 CFU/mL, 10^4 CFU/mL, 5×10^3 CFU/mL, with BSA–Apt–AuNT and BSA–Apt–AuNP substrates.

The prepared BSA–Apt–AuNT glass substrates have been utilized further to detect various concentrations of EC targeting the point-of-care detection of UTI in human urine. In this study, the detection of EC has been done first with the cultured EC bacterium diluted in NF water and then with EC spiked in healthy urine samples. For this purpose, the prepared BSA–Apt–AuNP substrate was taken in a cuvette filled with NF water while the uncoated glass substrate taken in another cuvette filled with NF water as the reference for the baseline spectrum in a UV–Vis spectrophotometer, as shown in **Figure 3.9(a)**. Subsequently, the diluted solution of 400 µL 10^6 CFU/mL EC in 1 mL of NF water was added to the cuvette containing BSA–Apt–AuNP substrate then again UV–Vis spectra was obtained to monitor the change in LSPR of the prepared BSA–Apt–AuNP substrate, as shown in **Figure 3.9(a)**. Similar experiments were performed with BSA-Apt-AuNT substrate, as shown in **Figure 3.9(b)**, in order to compare the enhancements in the signals due to the use of nanotwins. The plots suggest that on the addition

of EC to the BSA–Apt–AuNT substrate, a significant increase in normalized absorbance (A_N) along with a concurrent blue shift ($\Delta\lambda$) have been observed, as compared to the BSA–Apt–AuNP surface.

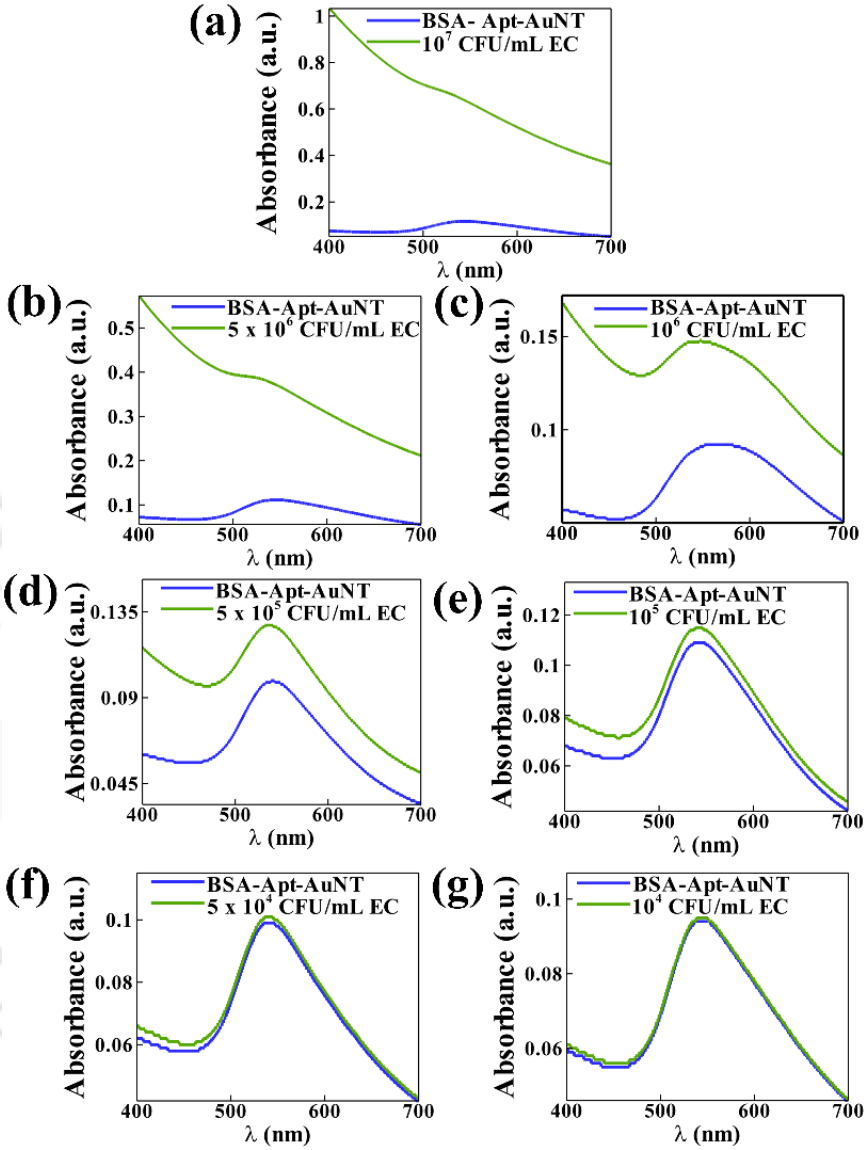

Figure 3.10: Shows the change in absorbance and wavelength shift due to interaction of different concentrations of EC with BSA–Apt–AuNT.

The reasons for such observations could be hypothesized to the change in the local electronic environment of the Au NTs. On the addition of EC, the randomly coiled aptamers on the surface of Au NTs, owing to absence of strong intramolecular base pairing, forms a well characterized tertiary structure to bind specifically to the added EC in the analyte[281,282]. The interaction of the aptamer with the EC causes a change in the overall polarization of the EC–BSA–Apt–AuNT system due to alteration of net charge transfer to the AuNTs upon binding[281,283]. This causes the spectrum of the BSA–Apt–AuNTs to shift to lower wavelength. Also, since the size of EC is very large as compared to the AuNTs, a single cell of EC could

interact with a high number of Apt–AuNT which causes an enrichment in the local density of hotspots, which could be accounted for increased absorbance in this case[284]. The LSPR variation observed for different concentrations of EC – 10^7, 5×10^6, 10^6, 5×10^5, 10^5, 5×10^4, 10^4, and 5×10^3, with BSA–Apt–AuNT surfaces have been summarized in **Figure 3.10**. **Figure 3.10** shows the change in the absorbance and the wavelength shift on the interaction of different concentrations of EC with BSA–Apt–AuNT substrates, it could be observed from the figure that with lowering the concentration of EC, the change in the LSPR response diminishes, which has been marked a s a tool to detect different concentration of EC present in the analyte of interest.

Figure 3.9(c) shows the calibration curve for the variation in LSPR obtained for different concentrations of EC – from 10^7 to 5×10^3 CFU/mL with both BSA–Apt–Au NP and BSA–Apt–Au NT coated glass substrates. The calibration curve depicts the variations in the normalized absorbance (A_N) with the concentration of EC. A_N was calculated using eq (3.5),

$$A_N = \frac{A_I}{A_0} \tag{3.5}$$

where A_I is the maximum absorbance of the UV–Vis spectrum obtained for the BSA–Apt–Au NP or BSA–Apt–Au NT coated glass substrate on the addition of respective EC concentration and A_0 is the maximum absorbance of the UV–Vis spectrum of the corresponding glass substrate with NF water. The figure suggests that the BSA–Apt–AuNT substrate shows better resolution as compared to BSA–Apt–AuNP surface to distinguish EC concentrations in the limit of concern for the UTI diagnosis, which is ~10^5 to ~10^6 CFU/mL. However, the enhancement in the absorbance is not much significant in the lower ranges, which could be attributed to less LSPR effect due to lower number of attachments of EC with the Apt in the substrate. In the clinical range for UTI, the enhancement in the absorbance of the proposed sensor is found to be ~10% higher for 10^5 CFU/mL, ~20% higher for 5×10^5 CFU/mL, ~40% higher for 10^6 CFU/mL, ~165% higher for 5×10^6 CFU/mL, and ~296% higher for 10^7 CFU/mL. Thus, it could be concluded that the enhancement in the plasmonic property of the BSA–Apt–AuNT coated glass substrate is capable of suitably enhancing the A_N of the glass substrate to detect EC concentrations as compared to BSA–Apt–AuNP coated glass substrate, and can surely improve the diagnosis of UTI in the limit of concern at early stages.

3.4.2. Interference study

Following the detection, an interference study has also been done to validate the specificity of the proposed BSA–Apt–AuNT coated glass substrates towards MTCC–42 EC species. The

specificity of the prepared sensor substrate means the capability of the prepared sensor to sense EC in presence of other bacterial species in the analyte. It is validated by exposing the sensor to non-specific bacterial species. For this purpose, the interference of three other bacterial species namely, *Staphylococcus aureus* (SA), *Enterococcus Faecalis* (EF), and *Klebsiella pneumonia* (KP) has been experimented. **Figure 3.11** shows the interaction of different bacterial species with BSA–Apt–AuNT surface. **Figure 3.11(a)** shows that on the addition of 400 µL of 10^6 CFU/mL EC, an increase in absorbance (green curve) along with concurrent blue shift, as found previously in **Figure 3.9**.

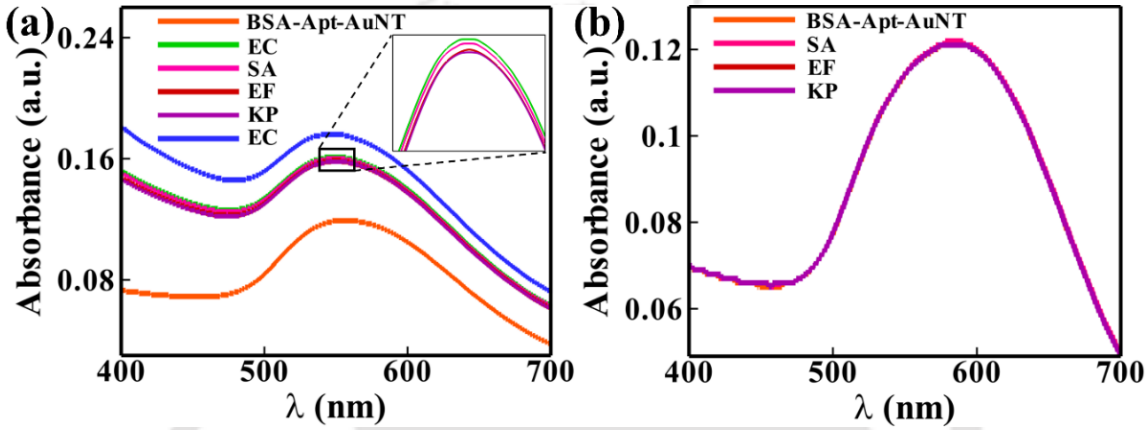

Figure 3.11: Plot (a), with the help of UV–Vis spectroscopy depicts the selectivity of the sensor – the UV–Vis spectroscopic absorbance changes on the addition of EC (green curve) unlike on the addition of equal volume of SA, EF, and KP with further change in absorbance on subsequent addition of equal volume of EC (blue line). Plot (b) shows UV–Vis spectroscopy of BSA–Apt–AuNT glass substrate before and after additions of SA, EF, and KP, successively.

However, on subsequent addition of 10^6 CFU/mL of SA, EF, KP one after the other, no such LSPR shift or variation in absorbance has been observed. Interestingly, on further addition of the equal volume of EC, an additional enhancement in the absorbance (blue curve) with simultaneous blue shift of the spectrum has been observed. Thus, the figure confirms that a significant blue-shift of the peak and increase in the intensity of absorbance could only be observed after the addition of EC and does not show any such LSPR variation in the presence of other bacterial species used for the study. It proves that the prepared BSA–Apt–AuNT substrate is highly specific towards EC. **Figure 3.11(b)** shows that on the addition of 10^6 CFU/mL of SA, EF and KP subsequently, no change in absorbance or shift in wavelength is observed, which shows that the BSA–Apt–AuNT does not show any plasmonic response in the absence of EC. Therefore, the above experiments help in concluding that the proposed sensing technique can faithfully detect EC, even in the presence of the other interfering pathogens.

3.4.3. Detection of UTI using urine sample

The prepared BSA–Apt–AuNT substrates have also been verified for the detection of EC in the human urine samples. For this, urine sample of healthy volunteers, who was not positive to UTI, was collected and then the cultured EC is spiked in the urine solution to prepare different concentrations of EC. UV–Vis spectroscopic analysis of the detection of EC in urine samples was done similar to the EC detection in aqueous sample as explained in section 3.4.1. Initially, the UV–Vis spectra of the BSA–Apt–AuNT substrate was obtained by immersing the substrate in NF water, as shown in **Figure 3.12(a)**. After that, the diluted solution of 400 µL 10^6 CFU/mL EC in 1 mL of urine sample was added to the cuvette containing BSA–Apt–Au NT coated glass substrate and again UV–Vis spectra was obtained to monitor the change in LSPR, as shown in **Figure 3.12(a)**.

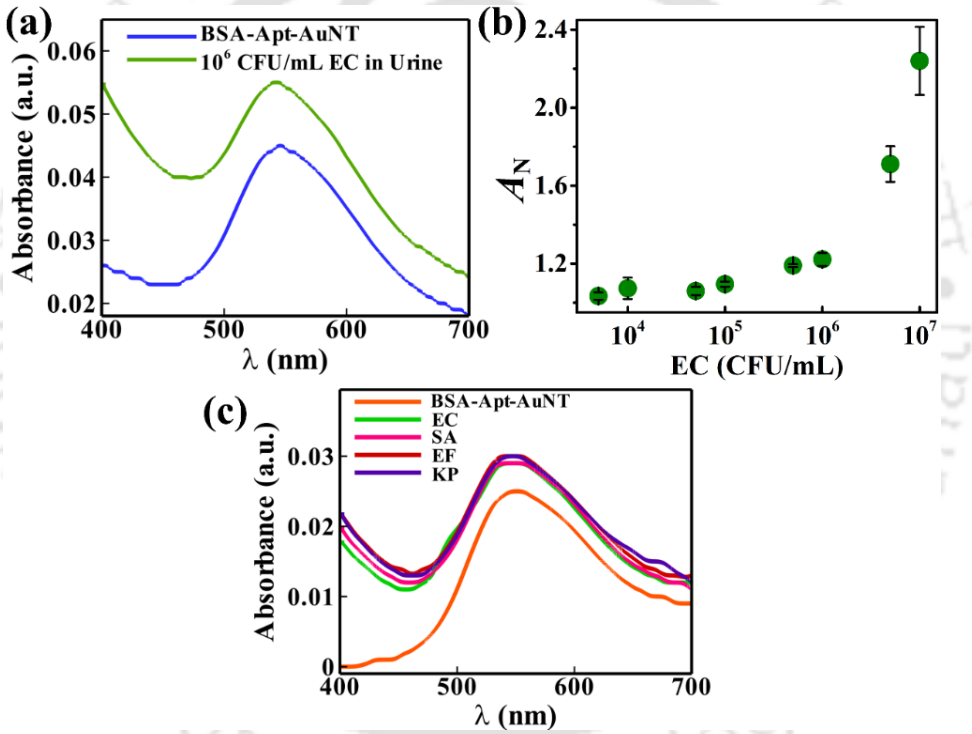

Figure 3.12: Plot (a) shows the LSPR change on the interaction of 10^6 CFU/mL EC in urine with BSA-Apt-AuNT substrate. Plot (b) shows the calibration curve for different concentrations of EC prepared in urine sample. Plot (c) shows the effect of addition of non-specific targets- SA, EF, and KP spiked in urine sample after the addition of EC on BSA-Apt-AuNT substrate.

It could be observed from the figure that the change in the LSPR is similar to that observed for the aqueous EC detection described in Figure 3.9. Figure 3.12(b) shows the calibration curve obtained for the response of the prepared BSA–Apt–Au NT substrates for different concentrations of EC spiked in urine samples. The calibration curve is prepared by analyzing five sets of experiments and averaging it for each different concentrations of EC spiked in urine sample.

Besides this, a check on the interference of foreign species like SA, EF, and KP was also performed, as shown in **Figure 3.12(c)**. For this study, all the bacterial species' solutions were prepared in the urine sample collected from the volunteer. At first, UV-Vis spectra was obtained for the interaction of 10^6 CFU/mL concentration of EC with BSA-Apt-AuNT substrate, as shown in the **Figure 3.12(c)**. Subsequently, 10^6 CFU/mL concentration of SA, EF, and KP were added one after the other and the UV–Vis spectra were recorded. The figure suggests that a change in the LSPR response is observed on the addition of EC. However, no such change is observed on further addition of any other pathogen like SA, EF, and KP, similar to the observations reported in the Figure 3.11(a). Thus, the above results elucidate that the developed plasmonic substrate is competent to specifically detect EC in the human urine samples even in the presence of other bacterial species.

3.4.4. Point–of–Care–Testing (POCT) of UTI

After establishing the proof-of-concept, we have developed an electronic transduction set up for the Point-of-Care-Testing (POCT) of UTI using the patient's urine sample. The electronic arrangement comprises of, (i) commonly available plane polarized optical source, which is a laser of 650 nm; and (ii) an optical detection unit, which is a silicon photodetector (TSL2561) with spectral range 400 nm to 800 nm for visible light recognition and effective 10-bit dynamic range suitable for explicit measurement of the intensity in the specified wavelength range, as shown in **Figure 3.13**.

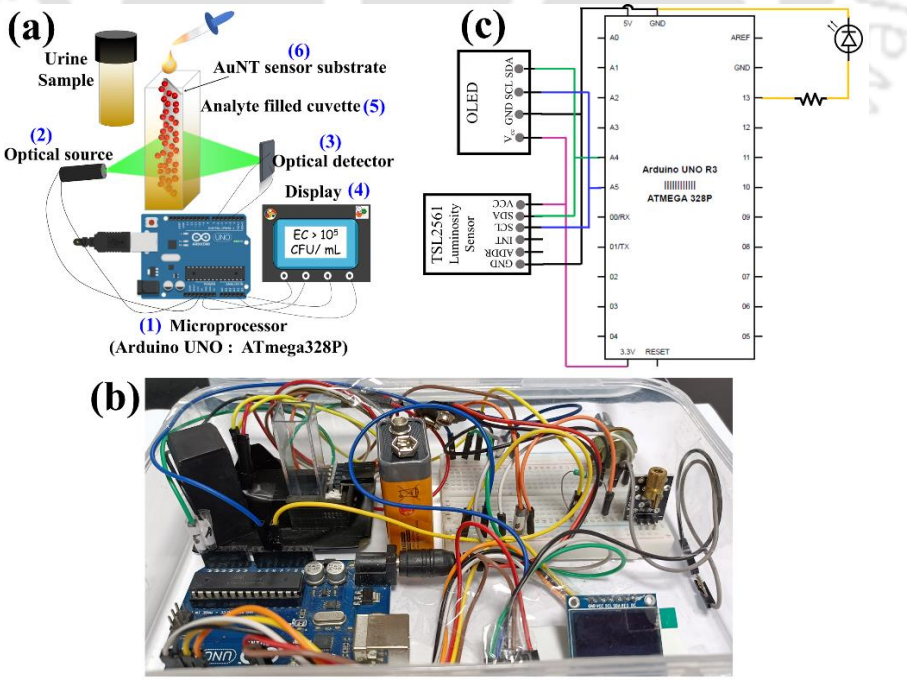

Figure 3.13: (a) Shows schematic representation of the device setup with its associated components, such as Arduino UNO (1), optical source (2), photo-detector (3), a digital display unit (4), cuvette (5), and AuNT sensor substrate (6), image (b) shows the developed prototype of the device, image (c) shows the circuit diagram of the proposed device prototype.

Figure 3.13(a) schematically shows the electronic arrangement of the developed POCT unit. The prototype consists of a disposable cuvette to hold the BSA–Apt–AuNT glass substrate for sensing purpose. The output signal of the photodetector is processed using an Arduino UNO based microcontroller unit and an organic light emitting diode (OLED) display is integrated to indicate the sensor readings. **Figure 3.13(b)** shows an image of the developed prototype of the device. The circuit diagram of the developed device prototype is given in **Figure 3.13(c)**.

Figure 3.14 shows the results of the variations in LSPR property of the BSA–Apt–AuNT coated glass substrate on interaction with different concentrations of EC for both testing in aqueous solution and with healthy urine samples spiked with different concentrations of EC. **Figure 3.14(a)** shows the change in the normalized intensity (I_N) obtained at the photodiode after the interaction of the BSA–Apt–AuNT substrate with different concentrations of aqueous solution of EC. The normalized intensity (I_N) was evaluated using eq (3.6),

$$I_N = \frac{I_i}{I_0} \tag{3.6}$$

where I_N is the normalized intensity at the photodetector, I_i is the intensity of the BSA–Apt–AuNT substrate with diluted aqueous solution of 400 µL of EC in 1 mL of NF water and I_0 represents the intensity of the same BSA–Apt–Au NP–AuNT substrate kept in the cuvette filled with 1 mL of NF water.

Figure 3.14(b) shows the similar experiment with the urine samples spiked with different concentrations of EC. Interestingly, both the results show a monotonic decrease in I_N with decreasing concentrations of EC in the respective analyte, which is in line with the results obtained in UV-Vis spectrophotometer, as discussed before. Conclusively, the results show that the proposed sensing technique is potentially capable of distinguishing various concentrations of EC, which could be used for the low-cost and portable POCT of UTI.

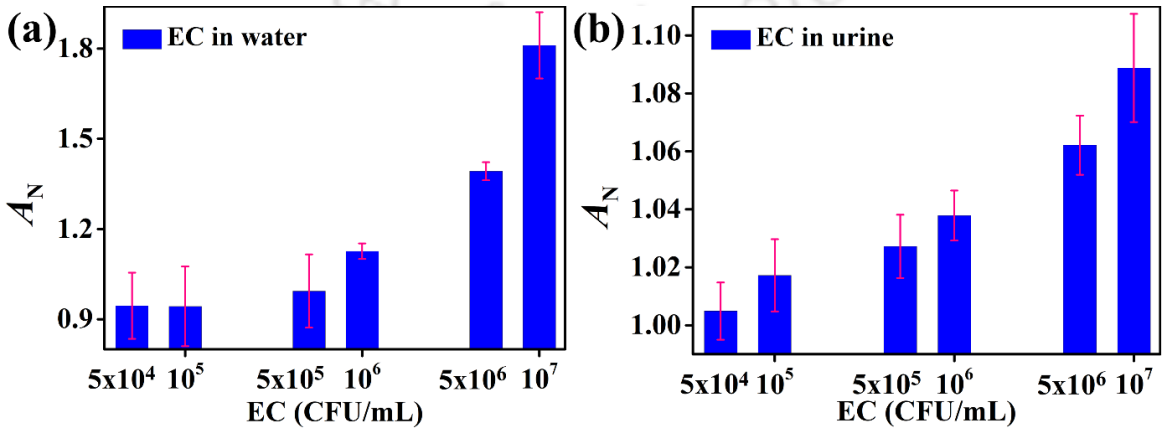

Figure 3.14: Shows the normalized intensity against different concentrations of EC in (a) aqueous solution and (b) urine sample.

3.5. Conclusions

In summary, the study focuses on the fabrication of an Au NT coated plasmonic glass substrate, which can further be utilized for the sensitive and specific point-of-care detection of the pathogen *Escherichia Coli*, as a measure to diagnose UTI. The study unveils that, decorating the Au NTs on the glass substrate, helps in a significant enhancement of its plasmonic response as compared to the isolated Au NP coated substrates, hence is suitable for high-precision sensing of pathogens. In order to selectively and specifically capture the pathogens, the Au NT coated plasmonic substrates are further attached with the aptamers that are specific to capture a target strain. Subsequently, in presence of the target pathogen, the change in the local refractive index around the Apt–Au NT coated plasmonic substrate causes enhancement in the absorbance as well as spectral shift towards the lower wavelength regime. The study shows that the interaction between the Apt–Au NT coated plasmonic substrate and the pathogen can be correlated to the enhancement of the absorbance as well as the Plasmonic shift. This sensor principle has been employed as the selective, sensitive, and specific detection of *Escherichia Coli* in human urine. In order to verify the specificity, an interference study has been performed to see the changes in LSPR of the Apt–Au NT coated substrate in the presence of other pathogens named *Staphylococcus aureus*, *Enterococcus Faecalis*, and *Klebsiella pneumonia*. The study proves the specificity of the developed substrates towards *Escherichia Coli*. The sensor has further been integrated to a point-of-care device wherein the Au NT-aptamer coated plasmonic substrate is placed in a cuvette filled with diluted analyte before illuminating the same with a plane polarized light source from one side while the transduced signal is measured with a photodetector from the other side of the nanobiosensor. The signal is then processed using a microcontroller unit to quantify the concentration of the pathogen in the analyte.

Concisely, the study shows the fabrication of a highly sensitive and specific nanobiosensor, which can be integrated to a proof–of–concept prototype for the point-of-care detection of UTI. The proposed methodology is versatile in a sense that one can employ the same methodology to capture any other pathogen simply by changing the aptamer, which is to be made specific to the target pathogen. Further, the same device can also be employed to detect pathogens in the water with some modifications.

Chapter 4

Quantification of Cholesterol and Tri–Glycerides Employing SERS of Silver Shelled Gold Nanorods

ABSTRACT

We report the synthesis of bimetallic plasmonic nanostructure of silver shelled gold nanorods (Ag–Au NRs) which in turn has been employed for the selective detection of (Cho) and tri–glycerides (TG) employing Surface Enhanced Raman Spectroscopy (SERS) enhanced by the synthesized nanostructures. Briefly, gold nanorods (Au NRs) was synthesized employing seed mediated growth method followed by creating a shell of silver via reduction of $AgNO_3$ onto synthesized gold nanorods. The silver shelled gold nanorod shows augmented Surface Enhanced Raman Spectroscopy (SERS) property owing to plasmonic hybridisation of Localized Surface Plasmon Resonance (LSPR) spectra of silver and gold. The enhanced SERS property was utilized for selective quantification of Cho and TG. For capturing the SERS enhancement two specific Raman reporters, DTNB and 4ATP, were chemically attached on the surface of Ag–Au NRs to synthesize SERS nanoprobes, before the attachment of the bioreceptors –cholesterol oxidase (ChOx) and lipase (Lp) to form ChOx–DTNB–Ag–Au NRs and Lp–4ATP–Ag–Au NRs, which were used later for the quantification of various concentrations of Cho and TG. Solution based liquid Raman spectroscopic study was performed to mitigate zone specific Raman effect which is common for solid substrates. The change in SERS spectra of the specific Raman reporters were systematically recorded in reference to the blank sample. Further, the Raman spectrum was utilized for the preparing the calibration curve for both the Cho and TG. Additionally, various interference studies taking ascorbic acid, glucose, sodium ion, and potassium ion were performed to justify excellent selectivity of the proposed method.

4.1. Introduction

In the intricate realm of human biochemistry, cholesterol and triglycerides play a pivotal role in maintaining the optimal physiological functioning of the body. These lipid biomolecules are essential for assessing and managing cardiovascular health[285,286]. Cholesterol serves as a key component for the formation of cell membrane, a precursor for synthesis of steroid hormones, predecessor for secretion of Vitamin D – crucial for calcium absorption and bone health, and Bile Acid – necessary for the digestion and absorption of fats[287]. Equally, triglycerides cater as energy source of the body by storing excess energy in the adipose tissues, fulfil energy requirement of the cells by transforming into fatty acids, and are responsible for transporting fat-soluble vitamins A, D, E, K through the bloodstream[288].

Predominantly cholesterol is synthesized in liver via *de novo* synthesis. Being insoluble in water, the bipolar biomolecules such as High Density Lipoprotein (HDL) and Low Density Lipoprotein (LDL) transport cholesterol throughout the body[289]. LDL carries cholesterol from liver to the cells for utilization in various metabolic functions. The cells release the surplus cholesterol into the bloodstream which is reclaimed by HDL and transport to liver for elimination. An imbalance between the LDL and HDL elevates the cholesterol accumulation in the blood causing plaque formation in the arterial walls[290,291]. Left untreated, the plaque accumulation can cause adverse cardiovascular diseases like hypertension, reduced blood flow, formation of blood clots, ischemia, peripheral artery disease and among others[292,293]. Conversely, triglyceride is primarily consumed via dietary intake. Once ingested, triglycerides are converted into fatty acids and glycerol during digestion which is then absorbed in the bloodstream and transported systemically with packaged inside lipoproteins especially Very Low Density Lipoprotein (VLDL)[294,295]. The excess and unutilized triglycerides are stored in the adipose tissues for future use. An elevated level of triglyceride level leads to hypertriglyceridemia causing various fatalities like atherosclerosis and coronary artery disease, pancreatitis, metabolic syndrome, type 2 diabetes, fatty liver and among others[296,297]. Therefore, the timely detection of any abnormality and monitoring of cholesterol and triglyceride levels in the blood is highly sought for.

Conventionally, Blood Lipid Profile testing is the gold standard for the identification of cholesterol and triglyceride levels in the blood[298]. According to National Lipid Association and the National Cholesterol Education Program (NCEP), the prescribed cholesterol level in blood is < 200 mg/dL for adults and < 170 mg/dL for children[299]. For triglycerides in blood, the recommended level is < 150 mg/dL for adults and < 90 mg/dL for children[300]. Although the blood profile test is widely accepted, various technological advancements have emerged to

improve the efficiency and efficacy of the test and contribute to a more patient-friendly diagnostic approach. Considering this, numerous researches have been made for enzymatic detection of cholesterol and triglycerides viz electrochemical sensors[301-303] employing voltametric/amperometry based sensing using carbonaceous materials[304-306] or nanostructures[307,308], colorimetric and plasmonic sensing using gold or silver nanostructures[302,309], chemiresistive sensors[310], semiconductor devices biosensors[311,312]. Therefore, the new innovations for advancing the blood lipid test and making it less invasive by incorporating cutting-edge approaches that can surpass current standards is fervently pursued.

Surface Enhanced Raman Spectroscopy (SERS) is a pioneering, non–destructive and state–of–art analytical technique that has been widely accepted for transformative approach to molecular characterization[313-315]. The localization of electric field in the vicinity of the plasmonic metal nanostructures owing to the characteristics of Localized Surface Plasmon Resonance (LSPR) creates “hotspots” of electron density surrounding the metal nanostructures[316-319]. These hotspots serve as the source for intense spectral recognition in SERS, thus surpassing the limitations of Raman Spectroscopy[320,321]. It has revolutionized the nanoscale light-matter interaction based biosensing approaches surpassing diffraction limits and enhancing the near field intensity[322-324]. Several studies have been reported for designing the highly SERS active metal nanostructures targeting label free single cell/molecule detection for precise and novel biosensing purposes[325-327].

In view of the above background, we focus on the development of a SERS based multiplexing principle for the simultaneous detection of cholesterol and triglycerides. Herein, we have synthesized a highly SERS active bimetallic nanostructure – the silver shelled gold nanorods (Ag–Au NRs). The plasmonic spectral hybridization of silver and gold produces significantly augmented spectral resolutions as compared to pristine silver or gold nanorods. Subsequently, the Ag–Au NRs were linked to two different Raman active molecules and immobilized with cholesterol oxidase and lipase for concurrent detection of different concentrations of cholesterol and triglycerides. The SERS examinations and the selectivity test with different interfering agents proves the proposed methodology to a reliable approach for biosensing applications.

4.2. Materials and methods

4.2.1 Materials

Analytical grade gold (III) chloride ($AuCl_3$), sulphuric acid (H_2SO_4), ascorbic acid (AA), silver nitrate ($AgNO_3$), cetyltrimethylammonium bromide (CTAB), trisodium citrate dihydrate ($Na_3C_6H_5O_7.2H_2O$), sodium hydroxide (NaOH), 5,5′–dithiobis–(2–nitrobenzoic acid) (DTNB), 4–aminothiophenol (4ATP), 1–ethyl–3–(3–dimethylaminopropyl)carbodiimide (EDC), N–hydroxysuccinimide (NHS), cholesterol oxidase (sp. *Streptomyces*) (ChOx), cholesterol (Cho), lipase (sp. *Candida*) (Lp), glyceryl trioleate (TG), triton X–100, isopropanol (IPA), tris–HCl buffer, phosphate buffered saline (PBS), 2–(N–morpholino) ethanesulfonic acid (MES) buffer, and bovine serum albumin (BSA) were purchased from Sigma Aldrich. All solutions are prepared in deionized water (DI) unless stated otherwise.

4.2.2 Instruments

For the present study the instruments used were UV-Visible spectrophotometer (Shimadzu, UV–2600 230 V EN), field emission scanning electron microscopy (FESEM Sigma 300), transmission electron microscopy (TEM, JEOL, JEM 2100 at the acceleration voltage of 200 kV), Raman spectroscopy (Horiba Scientific, LabRAM HR Evolution), attenuated total reflection based Fourier transform infrared spectroscopy (FTIR), hot plate cum magnetic stirrer (Tarsons, Digital Spinot), weighing machine (Sartorius, BSA224S–CW), desiccator (Tarsons), vacuum pump (Toshmiwal), deep freezer (Haier).

4.2.3 Methods

I. Synthesis of gold nanorods (Au NRs)

Au NRs was synthesized using seed mediated growth method as reported elsewhere[328,329] and described below:

Preparation of seed:

For the preparation of seed, 7.5 mL of 0.1 M CTAB solution was incubated at 30˚ C water bath for ~15 min. After that 100 µL of 24 mM $AuCl_3$ was added and stirred at 200 rpm for 5 min to form a clear solution. Subsequently, 600 µL of freshly prepared 0.01 M $NaBH_4$ was added to the stirring solution at 800 rpm and left undisturbed for 2 min. The appearance of brownish color of the solution marks the synthesis of seeds. The seed solution is then allowed to stir at 150 rpm for ~ 45 min before further use.

Synthesis of Au NRs:

For the preparation of Au NRs from the seed, 510 µL of 24 mM $AuCl_3$, 500 µL of 0.5 M H_2SO_4, and 200 µL of 0.1 M AA, and 150 µL of 0.1 M $AgNO_3$ were added successively to the stirring solution of 25 mL 0.1 M CTAB at 500 rpm kept at 30˚C water bath. The solution should be transparent after the addition of AA and then only $AgNO_3$ should be added. After that, the stirring was stopped and 60 µL of the seed solution was added and the solution was kept undisturbed at 30˚ C water bath for ~12 h. The formation of bluish green colored solution marks the synthesis of the Au NRs and the solution was then centrifuged at 25000 rpm for 25 min and redispersed in 25 mL of DI water for further use. Note that the color of the Au NRs formed may vary for different concentration of $AgNO_3$ used which signifies different aspect ratio of the Au NRs synthesized.

II. Synthesis of Ag-Au NRs

To prepare Ag-Au NRs[330] core shell nanostructures, the as synthesized Au NRs was centrifuged two times and redispersed in equal volume of 0.08 M CTAB. Afterwards, to 1 mL Au NRs solution, 90 µL 0.01 M $AgNO_3$, 80 µL 0.1 M AA, and 200 µL 0.1 M NaOH was added successively and kept in a water bath with temperature maintained at ~ 65˚ C for ~ 4 h. The synthesized Ag-Au NRs nanostructures were then centrifuged at 10000 rpm for 10 min and redispersed in equal volume of DI for further use.

III. Preparation of DTNB-Ag-Au NRs and 4ATP-Ag-Au NRs SERS active nanomaterials

SERS active nanomaterials were prepared by adding 10 µL of 20 mM DTNB or 10 µL of 20 mM 4ATP solution, prepared in ethanol, to 1 mL of the Ag-Au NRs and left undisturbed for ~ 5 h at room temperature in dark for the immobilization of DTNB or 4ATP to the Ag-Au NRs nanostructures. The DTNB-Ag-Au NRs and 4ATP-Ag-Au NRs nanostructures was then washed by centrifuging at 10000 rpm for 10 min and redispersed in DI water.

IV. Preparation of ChOx working solution

The working solution of 1 mg/mL ChOx was prepared in 50 mM PBS buffer solution, pH 7.4.

V. Preparation of Lp working solution

The working solution of 1 mg/mL Lp was prepared in 50 mM MES buffer solution, pH 6.

VI. Preparation of ChOx-DTNB- Ag-Au NRs and Lp-4ATP- Ag-Au NRs

For preparing ChOx-DTNB-Ag-Au NRs, DTNB-Ag-Au NRs was first immobilized with EDC-NHS[331]. For EDC-NHS immobilization, 50 µL of 50 mM EDC and 50 µL of 100 mM NHS prepared in 100 mM MES buffer with pH 6 were added to 1 mL of DTNB- Ag-Au NRs

solution successively and kept undisturbed for ~ 40 min. Subsequently, 9 µL of 1 mg/mL ChOx was added to the EDC-NHS immobilized DTNB-Ag-Au NRs and left undisturbed for ~ 20 h at RT to form ChOx-DTNB- Ag-Au NRs, and kept at 4˚ C for further use.

For preparing Lp-4ATP- Ag-Au NRs[332], 1 mg/mL Lp was at first prepared in 50 mM MES buffer with pH 6. To this solution ~ 1.9 mg EDC and ~ 2.8 mg NHS was added successively and stirred at 150 rpm for ~ 15 min. Subsequently, 5 µL of this solution was added to 1 mL of 4ATP-Ag-Au NRs and left undisturbed for ~ 4 h at RT and kept at 4˚ C for further use.

VII. Preparation of cholesterol (Cho) solution

A stock solution of 30 mg/mL Cho was prepared by mixing 60 mg of Cho with 1 mL of Triton X-100 and stirred at 500 rpm at 95˚C until the solution become transparent. To this solution, 1 mL of IPA was added and stirred for ~ 2 min and allowed to cool to RT before preparing working solutions. The stock solution is then stored at 4˚C in dark. The working solutions of Cho was prepared by diluting the stock solution with DI to the desired concentrations.

VIII. Preparation of Glyceryl Trioleate (TG) working solution

A stock solution of 50 mg/mL TG was prepared by mixing 550 µL of TG to stirring solution of 2.46 mL Triton X–100 to form a homogeneous solution. After that, 5 mL of 50 mM Tris–HCl with pH 8.5 was added and stirred for ~ 10 min. To this mixture, 2 mL of DI water was added and stirred for ~ 15 min. The solution formed would be milky white in color. The stock solution was kept at 4˚C in dark for further use. The working solutions of TG were prepared by diluting the stock solution in DI water to the required concentrations.

4.2.4. Simulation Framework

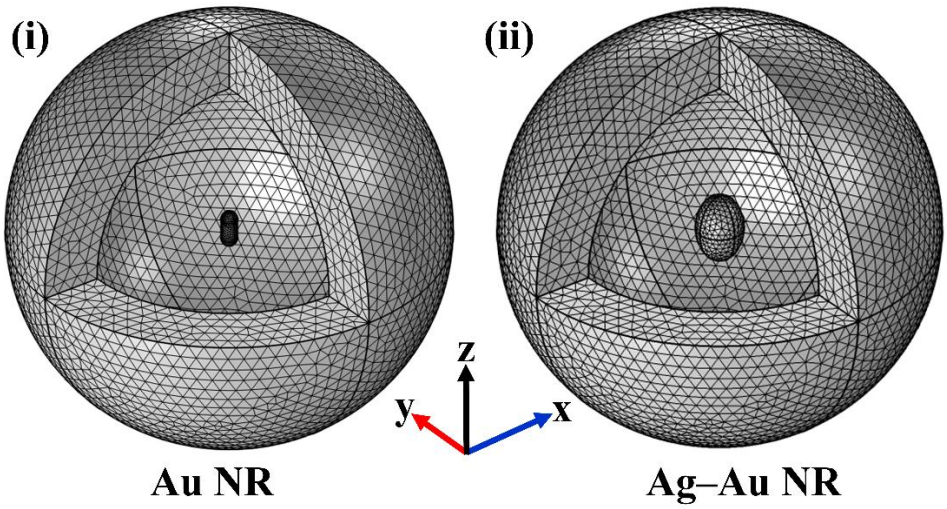

Figure 4.1: Shows the 3D geometry of (i) Au NR and (ii) Ag–Au NR used in the simulation.

Plasmonic enhancement of Au NR and Ag–Au NR has been simulated using finite element method (FEM) based analysis tool of COMSOL Multiphysics^{TM} 5.5. Here, FEM is deployed to solve complex engineering problem that involves coupled physics and spans over irregular spatial region. COMSOL Multiphysics provides physics-based default meshing option, wherein a preset algorithm is used for creating unstructured grids that consisted of triangles, quadrilaterals, tetrahedral, hexahedral, and prisms shaped meshes. For this work, the physics based meshing option was considered with minimum and maximum mesh element size of 0.36 nm and 8.4 nm, respectively. For the solution, we employed available direct PARDISO (Parallel Direct Sparse Solver) solver with coupled physics wherein all the set of linear equations are solved with a standard non-iterative numerical scheme like Gaussian elimination or LU decomposition.

Boundary Conditions

For the present study, Electromagnetic wave frequency domain physics of Wave Optics module of COMSOL Multiphysics has been used. The 3D geometry of the Au NR and Ag–Au NR are shown in **Figure 4.1**. The 3D geometry of the Au NR was designed by performing union operation on a cylinder of height 18 nm and radius 7 nm with two 3D spheres of radius 7 nm. The consolidated geometry depicts the experimental Au NR dimensions of length 32 nm and diameter of 14 nm, as discussed later in section 4.3.1. To represent the experimental Ag–Au NR geometry, an ellipsoid shell of a–semiaxis of 20 nm, b–semiaxis of 20 nm, and c–semiaxis of 30 nm has been over the Au NR structure to depict the uneven silver shell formation over Au NR as obtained in the experimental results discussed in section 4.3.2. An outer 3D sphere of 180 nm radius with 50 nm layer represents the perfectly matched layer (PML) used to truncate the physical domain and to avoid the internal reflections which represents the physical system in infinite space domain. The surrounding medium is taken as water with refractive index of 1.33, and the gold and silver material were taken from the material library considering experimental values of Johnson and Christy.

Here, the electromagnetic wave equation has been solved for scattered field, E_{sca} as given in eq (4.1).

$$\nabla\times\left[\frac{1}{\mu_r}\left(\nabla\times E_{sca}\right)\right]-k_0^2\left[\varepsilon_r-\frac{j\sigma}{\omega\varepsilon_0}\right]E_{sca}=0 \tag{4.1}$$

where, k_0 is the wavenumber in free space, μ_r is the relative permeability of the medium, ε_r is the relative permittivity of the medium, σ is the electrical conductivity, and ω is the angular

frequency. A plane wave E_b, given in eq (4.2), polarized and propagating along z–axis has been used for solving the scattered field of Maxwell's wave equations.

$$E_b = E_0 e^{-\frac{2\pi i}{\lambda} z} \hat{z} \tag{4.2}$$

where, E_0 is the amplitude of the incident electric field taken as 1 V/m, and λ is the wavelength of excitation.

4.3. Results and Discussion

4.3.1. Characterization of Au NRs

Figure 4.2 schematically shows the protocol for SERS based detection of cholesterol and triglycerides. Herein, the strong plasmonic field enhancement property of bimetallic nanostructures of silver capped gold nanorods has been utilized for the biosensing application. At first, Au NRs of aspect ratio of ~ 2 was synthesized using seed medicated growth method, as described earlier in section 4.2.3.

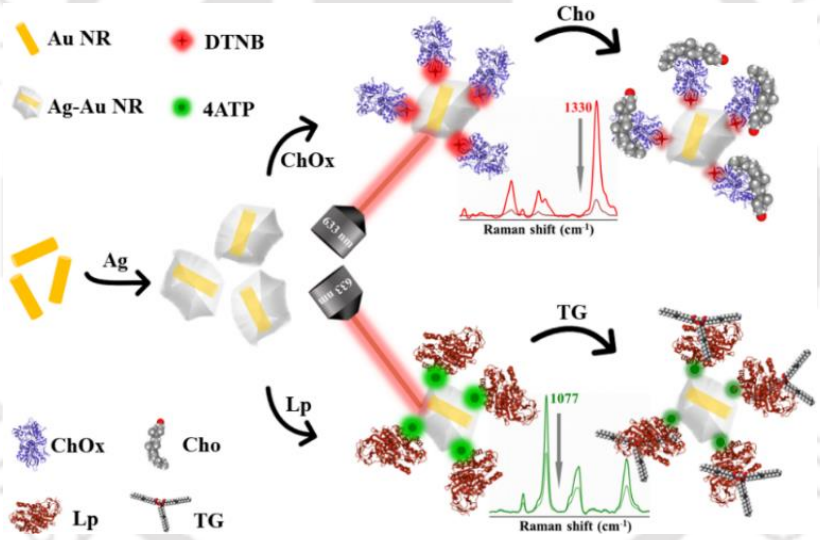

Figure 4.2: Schematic representation of the protocol used for the SERS based detection of cholesterol and triglycerides.

Figure 4.3 shows the morphological characterizations of the synthesized Au NRs. **Figure 4.3(a)** shows the UV–Vis spectroscopic characterization of the Au NRs illustrating two characteristic LSPR peaks of Au NRs – transverse peak at ~ 518 nm and longitudinal peak at ~ 645 nm. For this, 200 µL of the Au NRs was dispersed in 800 µL of DI water and the spectrum was observed in UV–Vis spectrophotometer. **Figure 4.3(b)** shows the FETEM imaging of the Au NRs showing the average diameter of ~ 14 nm and average length of ~ 32 nm. For FETEM characterization, initially, 10 µL of the synthesized Au NRs was diluted with 50 µL of DI water and was sonicated for ~5 min. The diluted sample was then dropcasted on a TEM grid and dried overnight in a vacuum desiccator before examination. The average diameter and length

of the Au NRs were examined using ImageJ software. Approximately 50 Au NRs were selected from the FETEM image shown in Figure 4.3(b) to calculate the average. **Figure 4.3(c)** shows the selected area electron diffraction (SAED) pattern of the Au NRs. The High–Resolution Transmission Emission Microscopy (HRTEM) image of the synthesized Au NRs in figure 4.3(b) and the ring appearance of the diffraction pattern (DP) recorded shows the merger of the field of many single crystals of the single crystalline Au NRs.

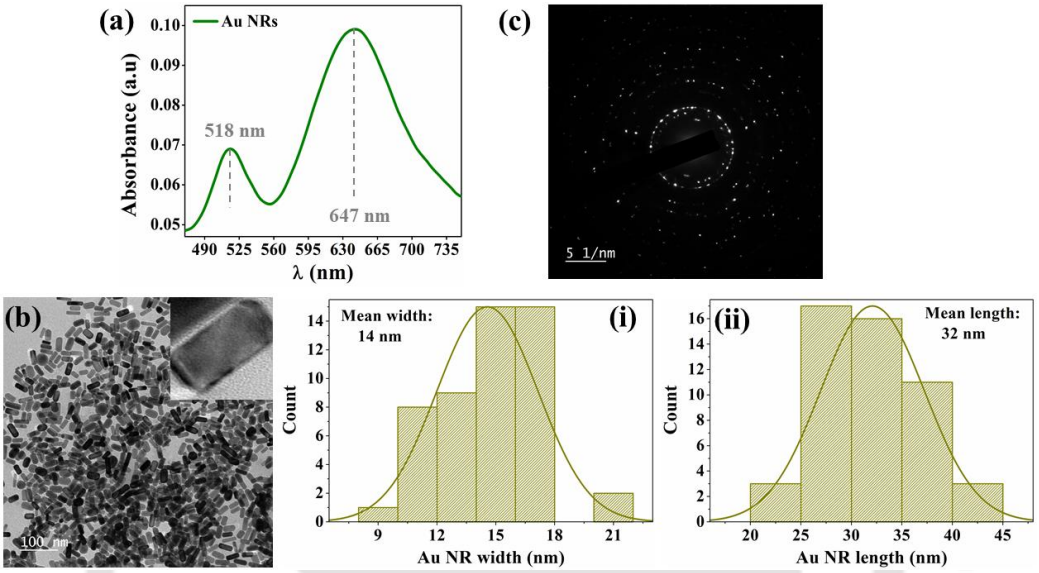

Figure 4.3: Shows (a) UV–Vis spectrum of the synthesized Au NRs, (b) FETEM imaging of the Au NRs showing average diameter of ~14 nm (i) and length ~32 nm (ii), HRTEM image of the synthesized Au NRs at the inset, and (c) SAED pattern of the synthesized Au NRs.

4.3.2. Characterization of Ag-Au NRs

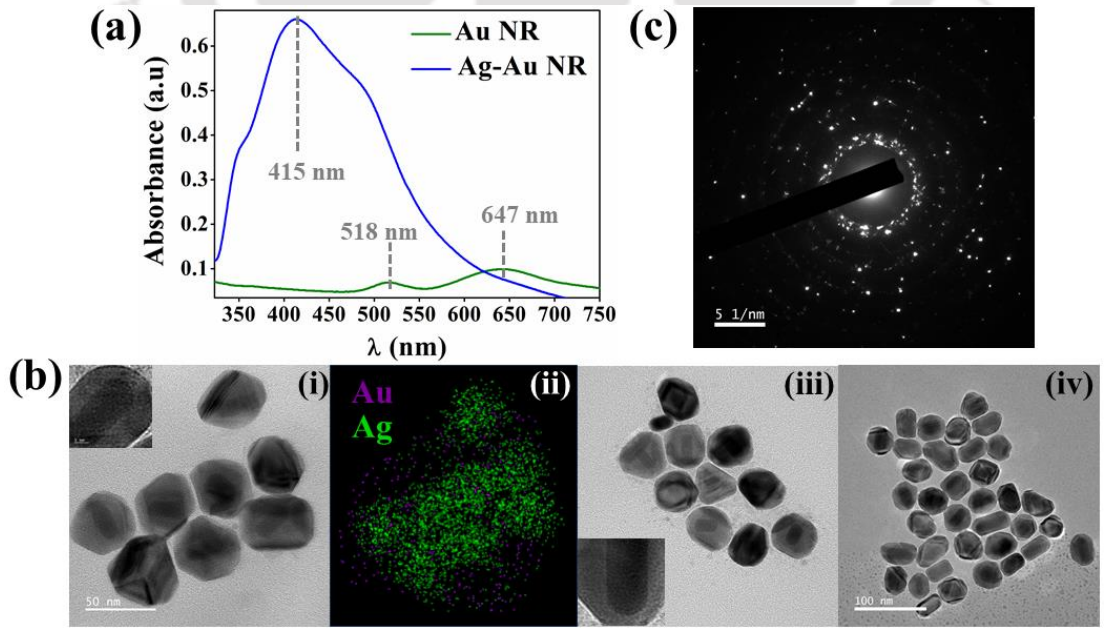

Figure 4.4: Shows (a) UV–Vis spectrum of the Ag–Au NRs as compared to Au NRs, (b) (i),(iii) and (iv) FETEM images of the synthesized Ag–Au NRs, inset shows the HRTEM images depicting

formation of the shell over Au NRs, (b)(ii) the elemental mapping of Ag and Au of (b)(i), and (c) SAED pattern of the synthesized Ag–Au NRs.

The synthesized Au NRs was then used for the synthesis of Ag–Au NRs. The synthesis protocol for Ag–Au NRs is given in section 4.2.3. **Figure 4.4** shows the morphological characterizations of the synthesized Ag–Au NRs. **Figure 4.4(a)** shows the UV–Vis spectroscopic peaks of Ag–Au NRs and Au NRs. The figure shows that the UV–Vis spectrum of Ag–Au NRs is significantly blue shifted to ~415 nm as compared to Au NRs which confirms the formation of Ag shell over Au NRs as the characteristic LSPR spectrum of silver lies within that specific domain[330]. The FETEM and the HRTEM (at inset) images in **Figure 4.4(b) (i), (iii),** and **(iv)** depict the single crystalline morphology of the synthesized Ag–Au NRs, and **Figure 4.4(b) (ii)** shows the elemental mapping of Ag and Au of the FETEM image shown in Figure 4.4(b)(i) which confirms the formation of Ag shell over Au NRs. The images illustrate the fully-grown Ag shell enveloping the Au NRs. **Figure 4.4(c)** shows the SAED pattern of Ag–Au NRs. The diffused grains and the circular DP appeared owing to the recording if the DP in the field of many single crystals of the Ag–Au NRs. The sample preparation for all the characterization is similar to Au NRs, as described earlier.

4.3.3. Characterization of DTNB–Ag–Au NRs and 4ATP–Ag–Au NRs SERS active nanomaterials

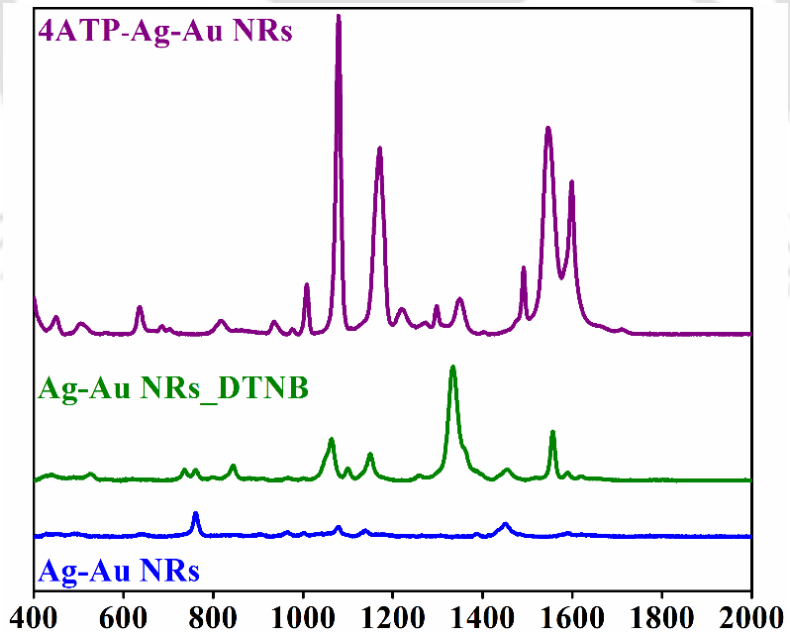

Figure 4.5: Shows characteristic Raman spectroscopic bands of DTNB–Ag–Au NRs and 4ATP–Ag–Au NRs as compared to pristine Ag–Au NRs.

The synthesized Ag–Au NRs were utilized for the preparation of SERS active nanomaterials for the biosensing application discussed later. For that purpose, two SERS active molecules– DTNB and 4ATP were immobilized on Ag–Au NRs via gold thiol coordination

bonding, separately. The preparation of DTNB–Ag–Au NRs and 4ATP–Ag–Au NRs SERS active nanomaterials is given in section 4.2.3. The immobilization of DTNB/4ATP on Ag–Au NRs were confirmed by the presence of characteristic molecular vibrational peaks of DTNB[333,334] and 4ATP[335,336] on Ag–Au NRs compared to pristine Ag–Au NRs as observed in Raman spectroscopy and shown in Figure 4.5. For the SERS measurement, 1 mL of the DTNB–Ag–Au NRs or 4ATP–Ag–Au NRs was taken in a cuvette and SERS was performed with 633 nm laser in liquid mode. The acquisition time, accumulation time, gratings and ND filter were set to 90 s, 4 s, 600 gr/mm, and 100%, respectively. The characteristic Raman bands of DTNB and 4ATP after immobilization on Ag–Au NRs are tabulated in **Table 4.1**.

Table 4.1. Table showing characteristic Raman bands of DTNB and 4ATP

DTNB–Ag–Au NRs		4ATP–Ag–Au NRs	
Raman band (cm^{-1})	**Assignment**	**Raman band (cm^{-1})**	**Assignment**
847	Scissoring vibration of NO_2 group	**1009**	C–C ring deformation
1063	Succinimidyl N-C-O stretching overlapped with aromatic ring modes	**1077** **1178**	C–C, C–S stretching C–H bending
1152	C–H deformation modes	**1350**	C–N stretching
1333	Symmetric NO_2 group	**1492, 1545**	C–H bending and C–C vibration
1558	C–C stretching on aromatic ring	**1598**	NH_2 bending

The plasmonic enhancement of the synthesized Au NR and Ag–Au NR was also numerically simulated using COMSOL Multiphysics™ based numerical simulation. Here, the near field enhancement of Au NR and Ag–Au NR was solved using Maxwell's Electromagnetic wave equation considering water as the surrounding medium. The details of the simulation framework are discussed in section 4.2.4.

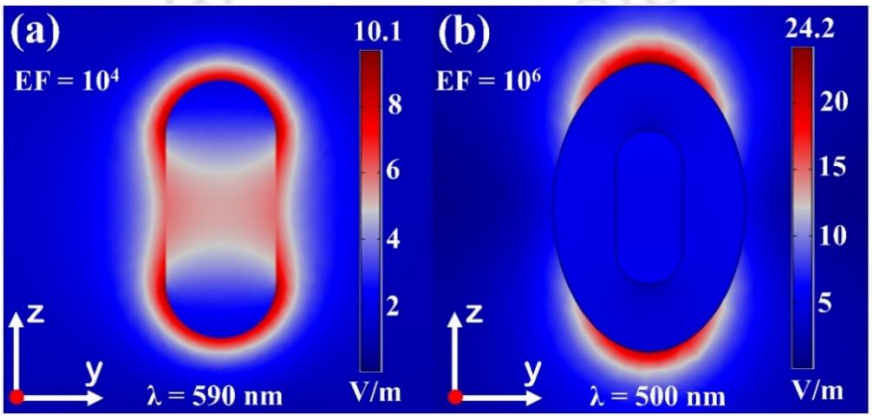

Figure 4.6: Shows simulation result for near field enhancement of (a) Au NR and (b) Ag-Au NR.

The electric field enhancement obtained from the simulation results are shown in **Figure 4.6**. The theoretical electric field enhancement EF_t is calculated using eq (4.3),

$$EF_t = \left(\frac{E_{\max}}{E_0} \right)^4 \tag{4.3}$$

where $E_{\max}$ is the maximum electric field obtained from the simulation, and E_0 is the applied electric field which is 1 V/m for the present study. **Figure 4.6(a)** shows the near field enhancement in an isolated Au NR which depict the EF_t in the order of ~10^4. Whereas the EF_t for Ag–Au NR was found to be in order of ~10^6, as shown in **Figure 4.6(b)**. The simulation results demonstrate the enhancement in the near field localization of the Ag–Au NR as compared to Au NR as also depicted in the SERS characterization. Therefore, further experiments were carried out utilizing Ag–Au NRs for the biosensing application discussed later.

4.3.4. Plasmonic property of DTNB–Ag–Au NRs and 4ATP–Ag–Au NRs

To validate the enhanced LSPR property of the bimetallic Ag–Au NRs nanostructure in comparison to Au NRs, plasmonic enhancement factor for both Ag–Au NRs and pristine Au NRs were examined using SERS, as shown in **Figure 4.7**. For this, 10 µL of 20 mM DTNB (or 20 mM 4ATP) was added to 1 mL of Ag–Au NRs and Au NRs, separately and left undisturbed for ~ 6 h. Afterwards, the solutions were centrifuged to separate the nanoparticles and suspended in DI water. For the SERS examination, 1 mL of DTNB (or 4ATP) immobilized Ag–Au NRs and Au NRs were used and the characterization was performed with 633 nm laser in liquid mode with the acquisition time, accumulation time, gratings and ND filter was set to 90 s, 4 s, 600 gr/mm, and 100 %, respectively.

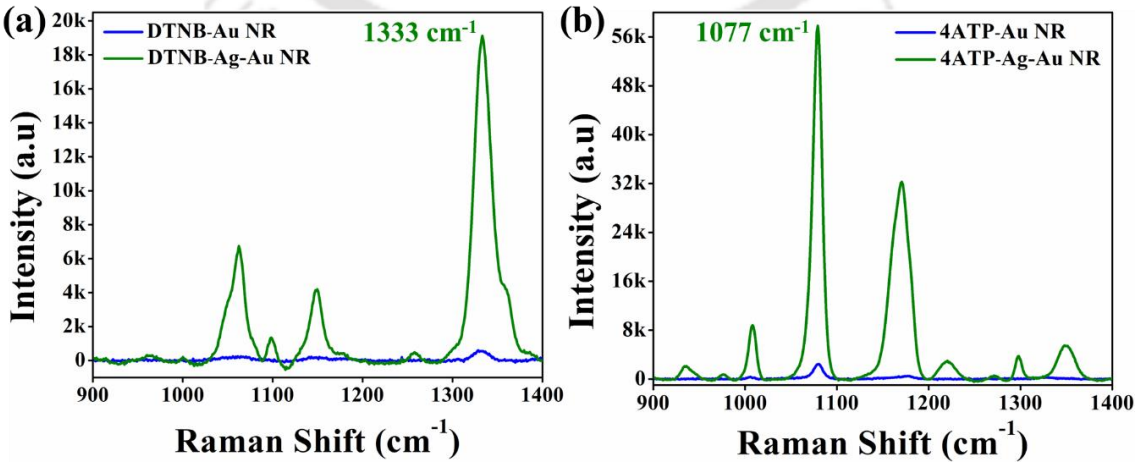

Figure 4.7: Shows the enhancement in SERS spectral peaks of DTNB–Ag–Au NRs and 4ATP–Ag–Au NRs compared to DTNB–Au NRs and 4ATP–Au NRs, respectively.

Figure 4.7(a) and **Figure 4.7(b)** show the spectral enhancement observed in the Raman bands of DTNB and 4ATP, respectively, after immobilizing on Ag–Au NRs and Au NRs. It could be inferred from the figures that the apex spectral peaks of DTNB at 1333 cm^{-1} and 4ATP at 1077 cm^{-1} show approximately 20 fold and more than 50 fold augmentation, respectively, on Ag–Au NRs in comparison to Au NRs. Earlier studies report that the combination of plasmonic metal nanostructures like Ag and Au show strong enrichment of electric field around the nanostructures – the LSPR property, owing to synergistic hybridization of the plasmonic bands of the two metals[337,338], as compared to Ag or Au in isolation. Therefore, one can infer that the remarkable plasmonic characteristics of Ag–Au NRs could be employed for sensitive detection of various biomolecules.

4.3.5. Biosensing of Cho and TG

Subsequently, the Ag–Au NRs were employed for the detection of cholesterol and triglycerides. At first, DTNB–Ag–Au NRs and 4ATP–Ag–Au NRs were immobilized with cholesterol oxidase enzyme (ChOx) for cholesterol detection and lipase enzyme (Lp) for triglycerides detection, respectively utilizing EDC-NHS bioconjugation chemistry. The detailed enzyme immobilization procedure is discussed in section 4.2.3 and shown schematically in **Figure 4.8**. The immobilization of ChOx and Lp was characterized with UV–Vis spectrophotometer and FTIR analysis, as could be depicted from **Figure 4.9** and **Figure 4.10**, respectively. UV-Vis spectroscopic characterization was carried out by diluting 200 µL of Ag–Au NRs (or ChOx–DTNB–Ag–Au NRs or Lp–4ATP–Ag–Au NRs) to 800 µL of DI water.

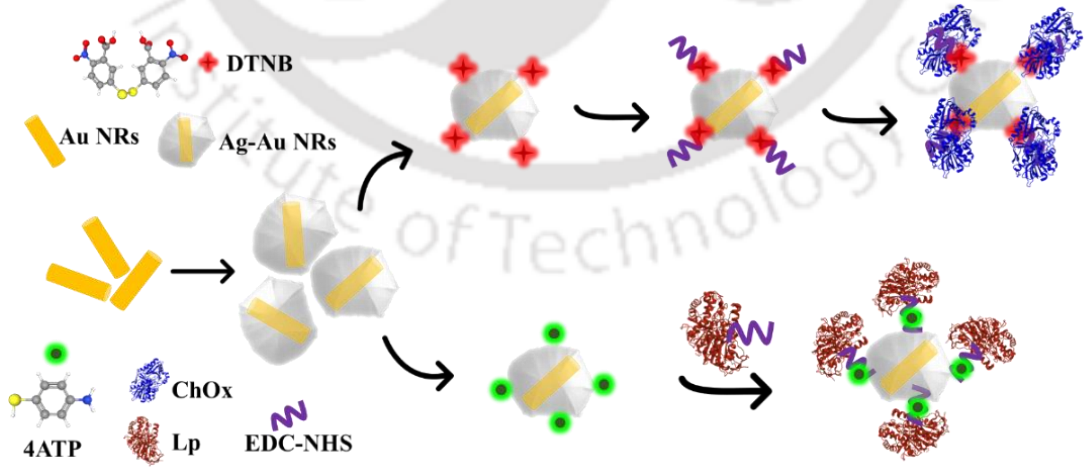

Figure 4.8: Schematic showing the immobilization of ChOx and Lp on DTNB–Ag–Au NRs and 4ATP–Ag–Au NRs.

Figure 4.9(a) and **Figure 4.9(b)** show the UV–Vis spectra of the Ag–Au NRs after the immobilization of ChOx and Lp, respectively. The figures show that the UV–Vis spectrum of

Ag–Au NRs are red shifted by ~11 nm and ~9 nm after the immobilization of ChOx and Lp, respectively, which confirms the attachment of the corresponding enzymes with the Ag–Au NRs nanostructures. The reason for such observations could be attributed to the change in the local refractive index surrounding the Ag–Au NRs after the immobilization of the enzymes which shifted the LSPR spectrum of the nanostructures to the longer wavelength[339,340].

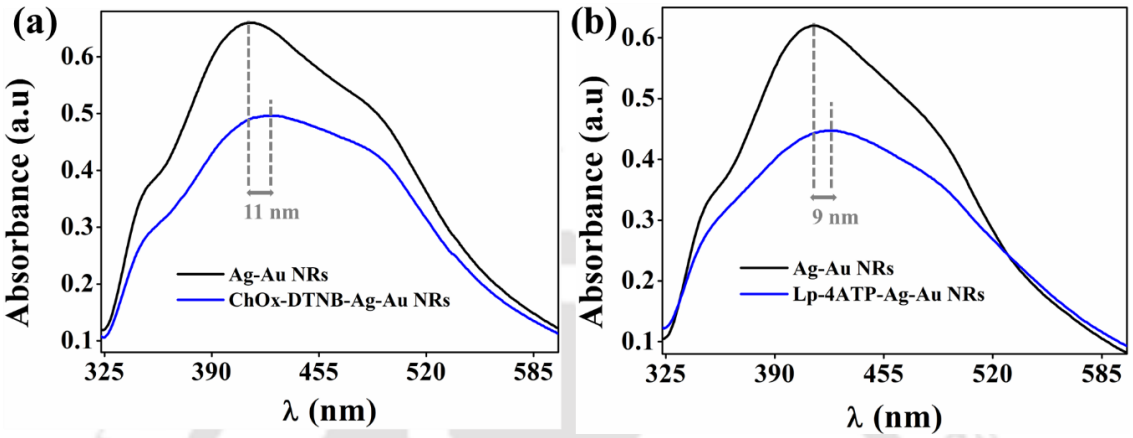

Figure 4.9: Plots of UV–Vis spectroscopic characterization of the immobilization of (a) ChOx and (b) Lp on Ag–Au NRs.

Figure 4.10(a) and **Figure 4.10(b)** show the FTIR analysis of the immobilization of ChOx and Lp on Ag–Au NRs, respectively. For the FTIR analysis, 500 µL of each sample was centrifuged and the pallets were redispersed in 50 µL of DI water before the characterization to obtain distinguishable peaks. Baseline correction was performed with DI water before examining the other samples. The characteristic vibrational peaks obtained after the attachment of the enzymes are tabulated in Table 4.2. The appearance of intense characteristic peaks of amide bands of the enzyme – Amide A, Amide I, Amide II, Amide III, after the immobilization of the ChOx and Lp on Ag–Au NRs confirms the attachment of the enzymes on Ag–Au NRs.

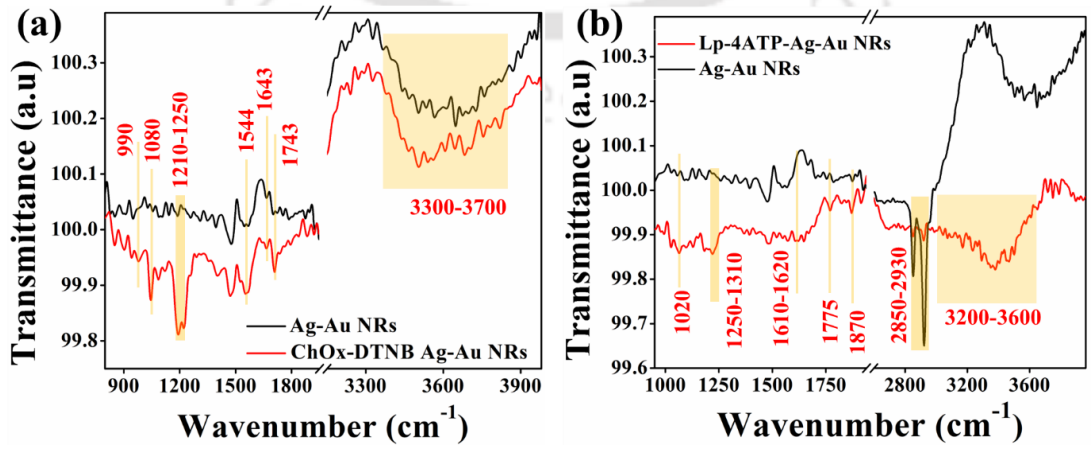

Figure 4.10. Plots of FTIR analysis showing the immobilization of ChOx (a) and Lp (b) on Ag–Au NRs.

For the biosensing application for detection of total cholesterol and triglycerides, SERS analysis was employed to observe the interaction of different of Cho and TG with ChOx–DTNB–Ag–Au NRs and Lp–4ATP–Ag–Au NRs. As per clinical reports[299], the desirable level of total cholesterol in blood should be less than 2 mg/mL for adults and 1.7 mg/mL for children. An elevated level exceeding 2.4 mg/mL is abnormal. For TG[341], the desirable level is 1.5 mg/mL for adults and 0.9 mg/mL for children. TG level higher than 2 mg/mL is a case of hypertriglyceridemia. Therefore, considering the clinical range of Cho and TG, different concentrations – 0.5 mg/mL, 1 mg/mL, 1.5 mg/mL, 2 mg/mL, 2.5 mg/mL, and 3 mg/mL, were prepared following the protocol stated in section 4.3.2. All the analyte solutions were prepared in PBS buffer to emulate blood serum. For the reaction of Cho (or TG) with ChOx–DTNB–Ag–Au NRs (or Lp–4ATP–Ag–Au NRs), 25 µL of different concentrations of ChO (or TG) was added to six different glass vials containing 1 mL of ChOx–DTNB–Ag–Au NRs (or Lp–4ATP–Ag–Au NRs) and was allowed to incubate in a water bath maintained at ~ 40°C for ~ 30 minutes. After the reaction, the solutions were allowed to cool to room temperature before SERS examination was performed. For the SERS study of total Cho (or TG), at first, 800 µL of ChOx–DTNB–Ag–Au NRs (or Lp–4ATP–Ag–Au NRs) was taken in a cuvette and SERS was performed in liquid mode. After that, 800 µL of ChOx–DTNB–Ag–Au NRs (or Lp–4ATP–Ag–Au NRs) reacted with different concentrations of Cho (or TG) were analyzed sequentially.

Table 4.2: FTIR peaks of enzyme immobilization

Chox–DTNB–Ag–Au NRs[342]		**Lp–4ATP–Ag–Au NRs[332]**	
FTIR peak (cm^{-1})	**Assignment**	**FTIR peak (cm^{-1})**	**Assignment**
990	P–O–C, C–O vibration	**1020**	C–N stretching
1080	PO_2^- stretching	**1250-1310**	Amide III, C–O stretching
1210-1250	Amide III	**1610-1620**	C–C stretching
1544	Amide II	**1775, 1870**	Amide I, C–O stretching
1643	Amide I	**2850-2930**	C–C vibration
1743	C=O stretching	**3200-3600**	O–H, N–H vibration, Amide A
3300-3700	O–H, N–H vibration, Amide A		

Figure 4.11 shows the SERS based biosensing of Cho and TG. **Figure 4.11(a)** show the change in the SERS intensity of ChOx–DTNB–Ag–Au NRs after reaction with different concentrations of Cho. The figure illustrates that the SERS intensity of ChOx–DTNB–Ag–Au NRs increases gradually after reaction with increasing concentrations of Cho with a shift in the Raman band towards higher wavenumber by ~ 1.5 cm^{-1} as shown in **Figure 4.11(c)**. Here,

Raman band at 1333 cm^{-1} has been considered for the study because it exhibits pronounced Raman intensity and substantial responsiveness with different concentrations of Cho.

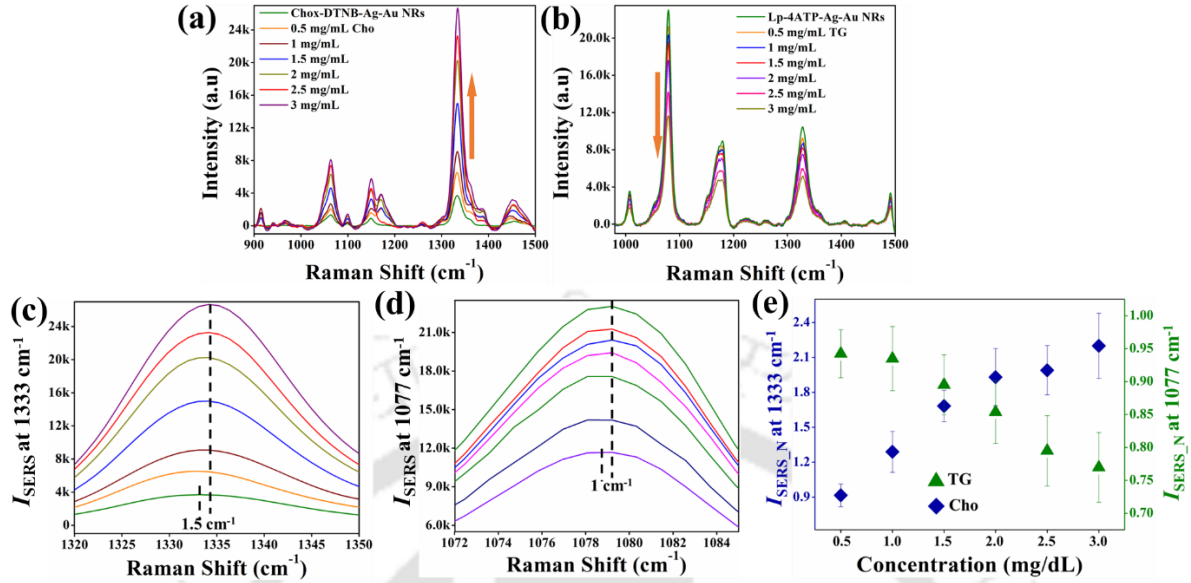

Figure 4.11. Shows change in SERS intensity of (a) ChOx–DTNB–Ag–Au NRs and (b) Lp–4ATP–Ag–Au NRs with different concentrations of Cho and TG, respectively. The figure shows the shift in the wavenumber after the reaction of (c) Cho with ChOx–DTNB–Ag–Au NRs and (d) TG with Lp–4ATP–Ag–Au NRs, and (e) shows the calibration plot for the detection of Cho and TG.

Similarly, **Figure 4.11(b)** and **Figure 4.11(d)** show the gradual decrease in SERS spectral intensity of Lp–4ATP–Ag–Au NRs with increasing concentrations of TG and a shift of Raman band at 1077 cm^{-1} by ~1 cm^{-1} towards the higher wavenumber. The reason for such concentration induced frequency shift could be attributed to the bonding of Cho to ChOx–DTNB–Ag–Au NRs and TG to Lp–4ATP–Ag–Au NRs, respectively. The formation of enzyme substrate complex induces a stress due to conjunction and creates a tension load on the adsorbed DTNB or 4ATP causing tensile deformation of the corresponding bands. Also, the bonding of Cho to ChOx and TG to Lp promotes an alteration of the electron cloud distribution causing a change in the polarizability of the DTNB–Ag–Au NR and Lp–Ag–Au NR system. This persuades a simultaneous effect on the charge transfer from Ag–Au NR to DTNB/4ATP which could be a probable reason for the variation in SERS intensities for the two cases[343,344]. **Figure 4.11(e)** shows the calibration graph for different concentrations of Cho and TG. The calibration graph is prepared by plotting the normalized SERS intensity (I_{SERS_N}) at 1333 cm^{-1} for bonding of Cho to ChOx–DTNB–Ag–Au NRs and at 1077 cm^{-1} for bonding of and TG to Lp–4ATP–Ag–Au NRs at different concentrations of Cho and TG, respectively, with the SERS intensity of ChOx–DTNB–Ag–Au NRs and Lp–4ATP–Ag–Au NRs, respectively, before reaction. The

plot shows a linear trend in the variation of SERS intensities with different concentrations of Cho and TG.

4.3.6. Interference study

Further, an interference study was performed to validate the specificity of the SERS based sensing technique for detection of cholesterol and triglycerides using ChOx–DTNB–Ag–Au NRs and Lp–4ATP–Ag–Au NRs, respectively. For the validation study, the following four major interfering agents present in blood and hindering the detection of cholesterol and triglycerides were used: viz ascorbic acid (AA), D–Glucose (D–Glu), sodium ion (NaCl), and potassium ion (KCl). The experimental procedure for testing the effect of the listed interfering agent was similar to that used for testing different concentrations of Cho and TG. Here, 25 µL of 2mg/mL of Cho, 0.02 mg/ AA, 1.1 mg/mL of D–Glu, 3.34 mg/mL of NaCl, and 0.25 mg/mL of KCl were added to five different glass vials containing 1 mL of ChOx–DTNB–Ag–Au NRs each and was allowed to incubate inside a water bath of ~ 40°C and for ~ 30 min. All the solutions were in PBS buffer. The glass vials were cooled to room temperature before the SERS examination was done. At first, SERS spectra of 800 µL of ChOx–DTNB–Ag–Au NRs was obtained and was considered as the baseline.

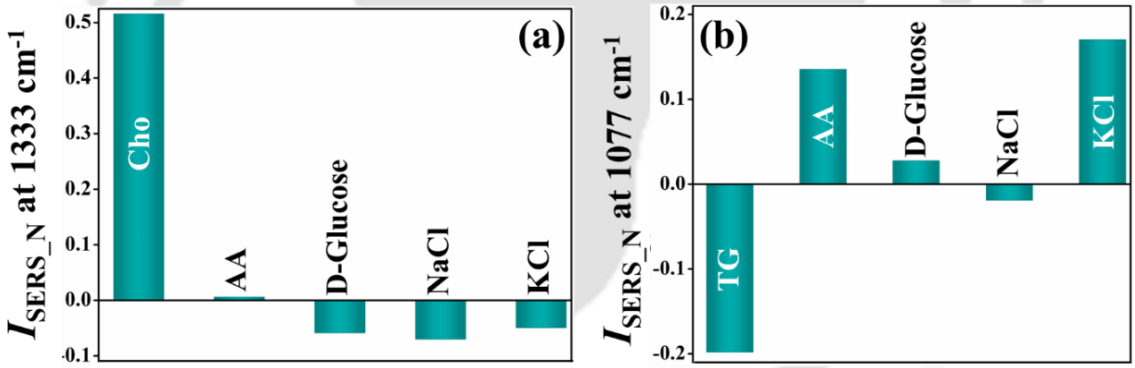

Figure 4.12: Plot showing validation study for (a) Cho with ChOx–DTNB–Ag–Au NRs and (b) Lp with Lp–4ATP–Ag–Au NRs.

After that, SERS spectra of each of Cho, AA, D–Glu, NaCl, and KCl reacted with ChOx–DTNB–Ag–Au NRs were obtained, individually. For validation study for Lp–4ATP–Ag–Au NRs, the experiments were repeated with 2mg/mL of TG was used instead of 2mg/mL of Cho, else remains same. The change in the SERS intensity of ChOx–DTNB–Ag–Au NRs and Lp–4ATP–Ag–Au NRs before and after the reaction was normalized, similar to Figure 4.11, to prepare the validation plots, as shown in **Figure 4.12**. **Figure 4.12(a)** shows the validation study for ChOx–DTNB–Ag–Au NRs with Cho, AA, D–Glu, NaCl, and KCl. The figure illustrates that only in the presence of Cho, the normalized SERS intensity (I_{SERS_N}) increases. For all other cases, either no change or an opposite trend is observed. Similar observations

could also be inferred for Lp–4ATP–Ag–Au NRs, as shown in **Figure 4.12(b)**. The plots show a decrease in normalized SERS intensity only for TG and for other interfering agents, either a minimal or opposite trend in change in SERS intensity was observed. Therefore, the plots in **Figure 4.11** and **Figure 4.12** demonstrate that the SERS based detection of Cho and TG has the potential to serve as a pivotal technique for multiplexed identification of lipid profile.

4.4. Conclusions

In summary, the study focuses on the development of a sensing technique utilizing SERS of plasmonic bimetallic nanostructures. Herein, silver shelled gold nanorods (Ag–Au NRs) have been synthesized by the reduction of silver nitrate on top of gold nanorods. The bimetallic nanostructures show enhanced LSPR characteristic as compared to pristine silver and gold nanostructures owing to plasmonic spectral hybridization of gold and silver. These nanostructures demonstrate ~20 fold and more than ~50 fold enhancement in the SERS spectral peaks of DTNB and 4ATP, respectively, as compared to its gold nanorods counterparts. Further, the enriched SERS characteristics of the synthesized bimetallic nanostructures were employed for the detection of cholesterol and triglycerides. At first, the Ag–Au NRs were linked with DTNB and 4ATP, separately, to prepare the SERS nanoprobes. Later, these DTNB–Ag–Au NRs and 4ATP–Ag–Au NRs were immobilized with cholesterol oxidase and lipase enzyme, respectively, employing EDC–NHS coupling chemistry. These enzyme-modified nanostructures were then utilized to observe the variation in SERS spectral peaks of DTNB and 4ATP when reacted with different concentrations of cholesterol and triglycerides, respectively. The SERS intensities before and after the interaction of the cholesterol or triglycerides with its corresponding enzymes immobilized on the bimetallic nanoprobes were monitored and normalized to quantify various concentrations of cholesterol or triglycerides, respectively. Interference study with ascorbic acid, glucose, sodium, and potassium ion showed the selectivity and specificity of the sensor.

Chapter 5

Pathways to Community Transmission of COVID–19 Due to Rapid Evaporation of Respiratory *Virulets*

ABSTRACT

The motions of virus laden respiratory microdroplets – '*virulets*' and their evaporation driven miniaturization in the open air are found to have significant impact on the community transmission of COVID–19 pandemic. In this direction, we simulate the motions of such droplets expelled from nose and/or mouth of a human being deploying the efficacies of computational fluid dynamics. The framework employs the physics for a laminar flow coupled with a droplet tracing model to track the motions of microdroplets while the sneezing or coughing have been emulated employing a time-periodic Gaussian velocity distribution function. An analytical model has also been developed to incorporate the influence of temperature (T) and relative humidity (RH) on the rate of evaporation and subsequent miniaturization of the on-the-fly virulets. Subsequently, the study considers virulets of different size range to follow the motions and perform an infectivity analysis. In that attempt, a force field analysis has been included considering the gravity, drag, and inertial force to unleash some of the finer features of virulet trajectories leading to the droplet and airborne transmissions of the virus. The study elucidates that virulets of lower size range (1–50 μm) tend to form a bioaerosol and facilitate an airborne transmission with a very less viral load while the virulets of significantly larger dimensions (300–500 μm) are more prone to droplet transmission as they settle faster under gravity towards the surfaces. Importantly, the rapidly evaporating virulets of intermediate size range with considerable viral loading are found to be more prone to the airborne transmission owing to on–the–fly bioaerosol formation. The study unveils the potency of such droplets to become airborne under suitable T and RH. Subsequently, the rate of evaporation and miniaturization of such droplets in the different cities across the globe with the variations in the T and RH have been mapped to the extent of community spreading of COVID–19 during first and second waves. The results corroborate that these parameters can be faithfully employed to predict the future waves of the pandemic.

5.1. Introduction

The recent outbreak of the deadly Severe–Acute–Respiratory–Syndrome Coronavirus 2 (SARS–CoV–2) pandemic has severely affected the health and economic conditions of the countries across the globe [345,346]. The use of face masks, maintenance of a healthy hand or face hygiene, and the use of a strict physical distancing protocol have become important practices for every individual to minimize the spreading of this highly contagious disease[347,348]. Importantly, it has now been scientifically established [349] that the pandemic spreads more rapidly through the micro/nanoscale airborne respiratory droplets, which emerge during the coughing, sneezing, breathing, or quite/loud speeches of an infected individual[350,351]. This is because the viruses of ~100 nm diameter create a finely dispersed suspension with the mucosal fluid of respiratory tracts[352] and a forceful breathing of air shears through the mucosal–air interface to generate the finely dispersed colloidal bioaerosol[353]. The size distribution of the colloidal microdroplets loaded with viruses is found to be in the range of 500 nm to a few hundred microns under varied conditions[354]. In that, the smaller ones have the tendency to spread the airborne infections while the bigger ones settle on the surfaces under gravity to spread the droplet-borne infections.

About a century ago, Flügge[355] in his seminal contribution demonstrated the concept of droplet transmission of infectious diseases such as malaria, tuberculosis and cholera, which has been instrumental in the advocacy of Mikulicz–Radecki's for the surgical gauze masks[356]. In another path breaking contribution, Wells classified the airborne transmission after dichotomizing the respiratory droplets into larger and smaller varieties for tuberculosis[357]. Importantly, transmission of other contagious diseases like tuberculosis, pneumonic plague, bronchitis, chicken pox, measles, or influenza also follow a similar transmission mechanism [350,351,358,359]. The droplet mode of transmission is possible when the virus loaded respiratory mucosal droplets are transported from the infected person directly to the exposed person or due to an indirect mode like a contact with the fomites of the infected person[360]. On the other hand, the airborne mode spreads through the exposure of virus-containing respiratory droplets in air for a longer distance and for a longer period of time[360]. According to a recent report, the SARS–CoV–2 laden mucosal droplets oozing out from an individual forming bioaerosol[360] are among the prime reasons behind the community spread of the virus. The virus laden droplets then find the way to the healthy host through the angiotensin converting enzyme 2−ACE2 receptor protein located abundantly in the mucosae of conjunctiva and nose-epithelia causing serious respiratory disorders[361].

Interestingly, such fluid mechanical events are also a very engaging from the perspectives of micro/nano droplet formation at the air–mucus interface and their transport through air[362]. For example, smaller droplets may float in air for a longer duration while even a mild air movement may transport the droplets further than usual[363]. Likewise, a smaller droplet may feel a much lesser gravitational pull while a bigger one may immediately precipitate after ensuing out of the nasal or mouth cavity. Importantly, the variation in the environmental temperature (*T*) and relative humidity (*RH*) in different geographical regions can play major roles in redefining the dynamics of the on the ejected droplets owing to the rapid evaporation and subsequent miniaturization. The dynamic change in the droplet diameter with these environmental parameters may transform a gravity bound bigger droplet into an air bound floating droplet. Such miniaturized droplets are benefitted of deficit pull from gravity and can easily travel to longer distances packed with infectious viruses, which may trigger the community spread of the disease, as discussed in this article.

However, thus far, all the analyses and inferences related to the droplet and airborne modes of transmissions have been rather ad–hoc owing to a few important scientific and technological limitations: (i) the dynamic experimental imaging of the suspended coronavirus nanoparticle inside a moving droplet is a challenging task to achieve[364] ; (ii) formation and transport of the mesoscale droplets of different size ranges from the nasal or mouth cavities are very difficult to characterize morphologically even with the state–of–art capacity of high-speed and high-resolution imaging[365]; (iii) the complexity is further elevated while tracking the viruses inside such droplet transport[366]; (iv) the relative humidity, temperature, level of pollutants, speed, and currents in air play crucial roles in the transport of the droplets[367]; and (v) size and angle of nose outlets, height of an individual, and the force of breathing, sneezing, and coughing are some of the parameters, which are very diverse across the globe[368]. Certainly, a deeper scientific analysis and understanding of the fluid dynamics of the trajectory of the sneezed or coughed droplets is crucial to establish a framework related to the physical distancing norms.

In this direction, one of the major scientific tools to explore the finer features of such a problem has been the computational fluid dynamics (CFD).[369] A number of prior seminal contributions have focused on exploiting the capacities of CFD to unearth the details of the respiratory droplet motion[370]. For example, Gupta et al.[371] has performed a benchmark to explore the probability distribution function mimicking the cough jets ejected by patients. Mittal et al. has summarized the generation mechanism of respiratory droplets and its parabolic flow physics governing the transmission of COVID–19[372]. Xie et al. has reported a wide study of flow dynamics of respiratory droplets considering the turbulent flow of the cough jet

considering effect of evaporation, relative humidity, air speed in a stagnant airflow for both water droplet and saline droplets[373]. Further, the effect of turbulence on the dispersion and deposition of the droplets in cough jets[374] and its exposure to a close contact[375] has been explored in stagnant airflow condition. The transmission of the respiratory droplets has also been analyzed in various closed environments like elevator, supermarkets, classrooms equipped with partition, indoor conditions like an air–conditioned room or ventilated room, Intensive Care Units (ICU) as reported in various studies[373,376-380].

Apart from focusing only on the flow dynamics, the effects of various external factors affecting transmission of respiratory droplets have also been explored broadly. The effects of atmospheric pollution[381], viability of the 2 m of physical distancing norm[361,367,382], flow dynamics of a turbulent dry cough jet/puff having contagious pathogen[383], drying time of the respiratory droplets[364,384], the effect of evaporation time of droplets on infection transmission [385-387], and the effect of relative humidity and breakup of cough droplets on transmission intensity[367,388] have also been explored widely. A very recent study uncover the flow dynamics of the ejected cough or sneeze droplets considering the movement of head while sneezing[368]. The detailed study of Pendar[389] show a comprehensive examination of mild cough to intense sneezes considering various initial velocity, size distributions, injection angles of saliva micro–droplets and mouth–opening area along with different environmental factors that drive the transmission airflow inside a room. Also, Zhao et.al. has showed that the droplets can travel three times farther in a wide range of temperature and humidity combination[390]. All these factors significantly characterize the aerosol based transmission of the disease attributing the second wave of COVID–19[391].

The present study focusses on a rather unexplored topic wherein the viral loading and infection potency of the respiratory droplets has been explored in detail to assess the risk of community transmission of SARS–CoV–2 infection. These respiratory droplets are the colloidal microdroplets of biofluid infused viral bodies – the sneeze or cough *virulets* which atomize into tiny bioaerosol to carry the loaded viruses faraway. Here, the spatiotemporal trajectories of the exhaled virus loaded droplets having various diameter have been simulated employing a complete set of fluid momentum equation and coupled fluid particle tracing physics. Moreover, the analyses of fluid flow fields and relative contributions of gravitational, drag, and inertial forces are quantitatively reported to strengthen the fundamental understanding of *virulet* dynamics. Furthermore, the effect of several sneezing or coughing frequencies and outdoor breeze conditions on the enhancement of dispersion of droplet transmission has also been reported. Effect of droplet size and their on-the-fly miniaturization

due to evaporation has been considered to explore the effect of *T* and *RH* on transmission of the infectious disease. Based on the miniaturization of the flying droplets, a simple evaporation model has been proposed and the study is also extended to compare the rate of evaporation of the droplets and number of confirmed COVID –19 cases from different regions across the globe. In the process, the study unveils a strong relationship of the transmission of the disease in airborne mode with the rapidly evaporating microdroplets. Exciting observations in terms of fluid dynamics, flow patterns of the droplets, risk of infection, and associated effects are also investigated in detail.

5.2. Theory

5.2.1 Problem formulation

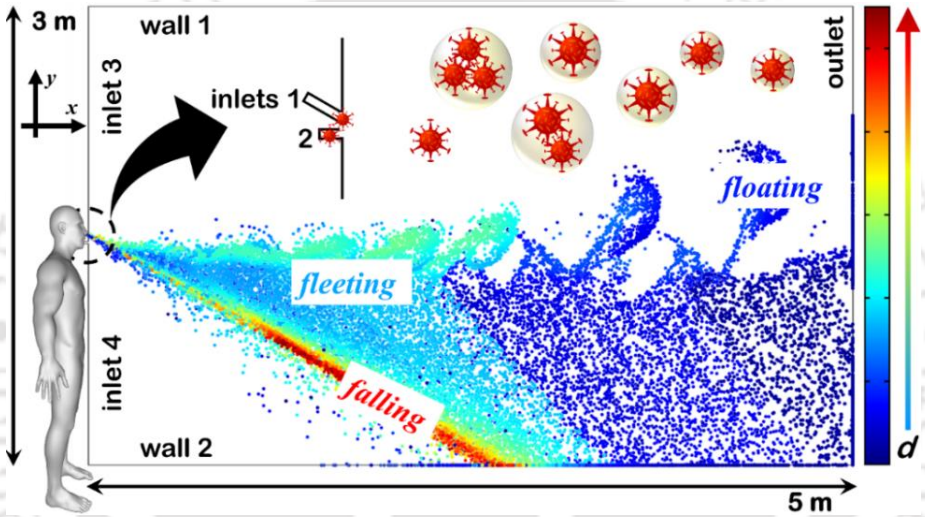

Figure 5.1. Schematically shows the 2D geometry considered for the simulation study with the dimensions and axes. The nose and mouth openings are indicated as inlets 1 and 2, respectively while inlets 3 and 4 show the open-air inlets. The walls 1 and 2, at the top and bottom show the upper boundary and ground of the solution space, respectively while the outlet in the geometry is shown towards the right side. The respiratory virulets of varied diameter *d* have been indicated by different color code. The inset schematically shows the SARS–CoV–2 loaded respiratory droplets expelled from an infected person.

Figure 5.1 schematically shows the motion of respiratory droplets, ejected from an individual in the open–air. The rectangular section in the figure shows the solution space, representing aerial premise of 3 m height (*h*) and 5 m length (*l*) in the proximity of the individual. The respiratory droplets enter into the solution space from the inlets 1 and 2, which emulate the nose and mouth openings, respectively. In this regard, inlets 3 and 4 show the open-air inlets. The walls 1 and 2 represent the top and bottom boundaries, respectively, while the outlet is assumed to be far away from the individual at a distance of 5 m, to study the extent of air-borne transmission. The openings for the nose and mouth are placed at a certain height

emulating the average height of an individual. The nose inlet has been tilted by an angle of 27˚, which represents a downward motion while sneezing, as shown in the inset of the figure.

For the numerical modeling, a two-dimensional (2D) Cartesian coordinate system has been employed, which considers the effect of external airflow from inlets 3 and 4, on the motion of the expelled respiratory droplets of varied diameter (d). The fluid (air), in this model is assumed to be isothermal, Newtonian and incompressible. Further, for the droplets, the effect of evaporation has not been considered in the simulation. Additionally, the effect of the evaporated droplets has been incorporated by considering droplets of varying sizes. The horizontal and vertical directions are represented as *x* and *y*, respectively. A bold variable represents a vector and a variable in italics represent a scalar quantity. The scalar variables placed in parenthesis of a vector indicate the components along the *x* and *y* directions. The velocity vectors of the fluid and droplets are symbolized as $\mathbf{u}_f$ (*u*, *v*) and $\mathbf{u}_d$ (*u*, *v*). The governing equations for the fluid flow are solved using the following continuity and Naiver-Stokes equations,

$$\nabla \cdot \mathbf{u}_f = 0, \tag{5.1}$$

$$\frac{D\mathbf{u}_f}{Dt} = -\nabla p_f + \mu_f \nabla^2 \mathbf{u}_f + \rho_f \mathbf{g} \tag{5.2}$$

Where ∇, D, p_f, μ_f, ρ_f, and g are the gradient operator, material derivative, air pressure, dynamic viscosity of air, density of air, and acceleration due to gravity vector, respectively. The motion of the droplets along with the external airflow has been modeled with the help of the following conservation of momentum equation,

$$\frac{\mathrm{d}\left(m_d \mathbf{u}_d\right)}{\mathrm{d}t} = \mathbf{F}_d^D + \mathbf{F}_d^g, \tag{5.3}$$

where, m_d is the mass of the droplet, $\mathbf{F}_d^D$ is the drag force, and $\mathbf{F}_d^g$ is the gravitational force experienced by the droplet. It has been observed that the sudden expelling of cough or sneeze droplets causes a transient high Reynolds number flow, which is impulsive in nature[371]. However, the velocity of the droplets decreases with time and during its passage it merges to a low Reynolds number laminar flow[392]. Hence, for this study, Stokes' drag[393], as shown in eq. 5.4, has been employed for the droplets because the droplet Reynolds number for different range are : 0.07 (1–50 μm), 1.50 (60–80 μm), and 5.56 (80–200 μm). It is a fact that for 300–500 μm, the Reynolds number is higher than 10. However, the virulets in this range are

significantly dominated by gravity, and do not tend to follow the fluid profile as discussed later.

$$\mathbf{F}_d^D = \left(\frac{18\mu_d}{\rho_d d^2}\right) m_d \mathbf{u}_r . \tag{5.4}$$

Here, the notations, ρ_d , d , and μ_d are density, diameter, and dynamic viscosity of the droplet. Further, $\mathbf{u}_r = \mathbf{u}_d - \mathbf{u}_f$ represents relative velocity of the moving droplet with respect to the velocity of the surrounding air. In addition, the gravitational force for the droplets has been considered employing the following expression,

$$\mathbf{F}_d^g = m_d \frac{\left(\rho_d - \rho_f\right)}{\rho_d} \mathbf{g} . \tag{5.5}$$

5.2.2 Boundary conditions

Table 5.1: Shows the typical values for the parameters employed in the simulations.

Parameter/Expression	Values
Density of air, ρ_f	1 kg/m^3
Dynamic viscosity of fluid, μ_f	1.8×10^{-5} Pa s
Velocities at nose and mouth inlets, $u_{\mathrm{m}}\left(2\pi\sigma^2\right)^{-1/2} e^{-\left[(t-0.3)^2/\left(2s^2\sigma^2\right)\right]}$	u_{m} = 9.2 m/s for sneezing, u_{m} = 6.2 m/s for coughing, $\sigma = 0.1$
Average air inflow, u_0	1-5, 7, 12, 15 m/s
Droplet density, ρ_d	1200 kg/m^3
Droplet diameter, d_d	1 – 500 µm
Dynamic viscosity of droplet, μ_d	10^{-3} Pa s

In order to solve the eqs (5.1) and (5.2), no slip and impermeable, $\mathbf{u}_f = 0$, boundary conditions are enforced on the walls 1 and 2. The sneezing and coughing conditions are emulated using a Gaussian velocity distribution at the inlets corresponding to nose and mouth with maximum speed, u_{m} , same as the speed of the sneezing or coughing, respectively. The **Table 5.1** depicts the function and the typical values that are employed for the simulations in the present study. The velocity boundary condition for the inflows at inlets 3 and 4 has been enforced as $\mathbf{u} = -u_0\mathbf{n}$ Atmospheric pressure boundary condition, $p = p_0$ is maintained at the outlet while the droplets are considered to be immovable after colliding the walls as $\mathbf{u}_d = 0$.

5.3. Numerical simulation and validation

COMSOL^{TM} Multiphysics, a finite element based CFD software, has been utilized for this work to solve the eqs. (5.1) to (5.5) after enforcing the aforesaid boundary conditions. The software employs Galerkin least–square method for the discretization of the equations with the boundary conditions and the fluid–particle–tracing (FPT) module has been employed for the droplet tracking in the surrounding air. In particular, the physics controlled unstructured triangular grids are used as the mesh elements during the simulations. For time marching, a backward difference scheme has been employed with an optimum time step of ~ 10^{-4} s to obtain an accurate solution. Since the solution space is significantly large, 3 m × 5 m, as compared to the size of the droplets, 1–500 μm, a grid independence study is performed to satisfy the adequate mesh required for an accurate numerical solution. **Figure 5.2(a)** shows the grid independence study profiles for different mesh cases listed in **Table 5.2**. The plot shows the maximum x-directional speed profile at a vertical height of y =1.4 m which is intuitive as the mouth and nose remain at an approximately similar distance, in the solution space. The figure shows that the fluid velocity profiles coincide for the meshes 3 and 4, which enable us in achieving the grid-independence before choosing the most accurate mesh, i.e., mesh 4, for the further explorations.

Table 5.2: Shows details of mesh used for the comparison of the mesh independence study.

Details of Mesh	Case 1	Case 2	Case 3	Case 4
Total elements	27044	42498	46936	53226
Mesh size (mm)	12-261	0.06-17.5	0.06-15	0.06-12.5

Figure 5.2(b) shows the comparison on the distance of the droplet fall evaluated from the present simulation study and an analytical calculation. For the simulation, the motion of only one droplet, ejected during sneezing, is considered after considering the inertial and gravity forces and in absence of any drag force. The inertia of the droplet is modeled in terms of a constant velocity, which varies from 1–5 m/s. Subsequently, the distance of the droplet travel has been evaluated from the present simulation before it is compared and contrasted with the analytical projectile range given by,

$$x_f = u_d \sqrt{\frac{2h}{g}} \tag{5.6}$$

Here, x_f is the distance travelled by the droplet in the x–direction, u is the initial x–directional velocity of the droplet, h is the height of the nose inlet from the ground, and g is the acceleration due to gravity. The plot suggests a close match within 1% deviation, even at

different wind speeds. **Figure 5.2(c)** proves the precision of the present work with the previous study. Here, the distance of travel of the droplets ejected during sneezing from the present study are compared with the study reported by Dbouk[279]. The two studies show similar traversal distance of the droplets, which validates the accuracy of the considered FPT model for the present study. Overall, the figure provides the basis for the use of the present computational framework for the further explorations of the droplet motions in the proposed geometry under varied condition.

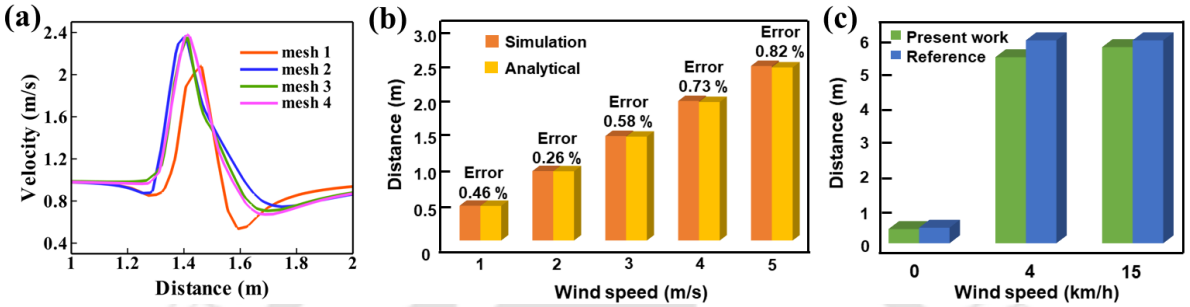

Figure 5.2: Plot (a) shows $\mathbf{u}_f$ along a cutline at x = 0.6 m at the solution space for four different mesh sizes. Plot (b) shows a comparison among droplet fall distance calculated from analytical relation and present numerical setting. Plot (c) shows the validation results of the distance travelled by the particle under certain external wind speed conditions in the present work compared with a report by Dbouk[367] study.

5.4. Results and Discussion

5.4.1. Viral load of sneeze/cough droplets

The respiratory processes like sneezing and coughing eject numerous water droplets with varying sizes ranging from less than 1 µm to 1000 µm in diameter or even larger[365]. These droplets are enriched with various elements like water, microbes, proteins, carbohydrates, or salts, apart from having different disease–causing agents like SARS–CoV–2 virus. Since the focus of this work is to gauge the potency of these droplets in the transmission of viral diseases, these water droplets are termed as '*virulets*' in this script. The viral load (V_L) of a droplet ejected from a SARS–CoV–2 infected patient depends on his/her viral concentration (C_v) in the mucus. For example, asymptomatic to weakly infected patients has $C_v = 10^4$ copies/mL while severely infected patients may have as high as ~10^9 copies/mL[394]. Thus, a droplet ejected from a patient can have varied amount of viral load based on its size and number of virus particles present inside the same. The probability of total viruses loaded inside a virulet for different C_v, can be approximated using Poisson's distribution[395] as,

$$f(n) = e^{-V_L d \frac{(V_L d)^n}{n!}} \tag{5.7}$$

Here, $f(n)$ is the probability of finding n number of viruses inside a virulet of diameter d, and $V_L(d)$ is the viral load,

$$V_L(d) = \frac{\pi}{6}\left(d^3 C_v\right) \tag{5.8}$$

In this study, d has been varied from 1-500 µm to consider the entire range of virulet sizes ejected during the respiratory activities like sneezing and coughing, and the size of the SARS–CoV–2 virus has been considered to be 100 nm diameter, as reported elsewhere[396]. **Figure 5.3(a)** shows the maximum number of viruses (n_{max}) that can coexist in a virulet of size d ranging from 1–500 µm for different C_v ranging from 10^4–10^9 copies/mL. The plots suggest that the n_{max} of an evicted droplet increases progressively with C_v. Considering a specific case, a 100 µm droplet can hold ~10 viruses for $C_v = 10^4$ copies/mL, however, the same droplet can hold ~ 6000 viruses when ejected from a patient with $C_v = 10^9$ copies/mL. In addition, a higher load of virus is expected inside the virulets with a higher d. On the contrary a bigger droplet with more viral load is expected to settle on the surface much faster while the smaller ones with a less viral load have the capacity to become airborne, as discussed later. The plots in the figure indicates that the infection potency of the virulets is less for smaller d (e.g., less than 100 µm) and lower C_v cases. However, such virulets may be of concern when expelled from a highly infected person.

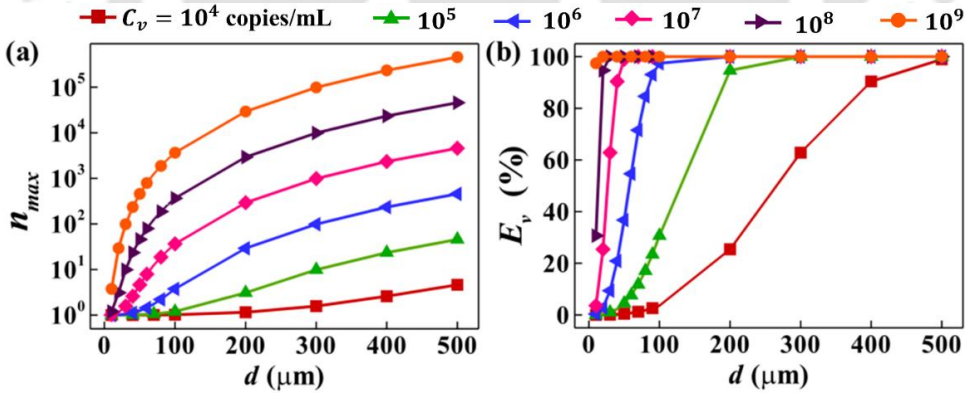

Figure 5.3. Plot (a) shows the maximum number of viruses n_{max} loaded inside a droplet of size d ejected from an infected person, and plot (b) shows the fraction of E_v among the total droplets ejected of size d, for C_v ranging from 10^4 copies/mL to 10^9 copies/mL and d ranging from 1–500 µm.

The other important factor to note here is that all the virulet sneezed or coughed out may not be infectious. **Figure 5.3(b)** shows the fraction of effective number of virulets (E_v) among total number droplets ejected during sneezing or coughing. E_v can be defined as those specific

droplets among all the expelled droplets which are loaded with viruses. Here, the total number of the ejected droplets is the total number of droplets of a specific size d that can be accommodated in 1 mL volume of water. This is because for a particular C_v say 10^4 copies/ mL, the total number of viruses is 10^4 in 1 mL of water. At first 1 mL of water is converted into corresponding number of droplets (N_d) of d keeping the total volume fixed to 1 mL. E_v is the total fraction of all the droplets (N_d) that are loaded with virus (N_v) i.e., virulets. E_v is given as,

$$E_v = \frac{N_v}{N_d} \times 100 \tag{5.9}$$

N_v is calculated by summing the product of N_d and probability of finding *n* number of viruses inside d using Poisson's distribution equation described in eq (5.7).

The plots in the **Figure 5.3** signify that for a lower C_v, a small fraction of the total ejected droplets is loaded with the viruses, whereas for a higher C_v, nearly all the ejected droplets can be filled with significant number of viruses. For example, if 1 mL of water is transformed into its corresponding number of say d of 200 µm, then for $C_v = 10^4$ copies/mL, only ~22% of droplets to host at least one virus. Conversely, for $C_v = 10^9$ copies/mL, each droplet (100%) may carry more than one virus during the ejection. The figure shows that for lower C_v, not all the droplets ejected are infectious. However, the majority of the droplets ejected from high C_v patients are capable of spreading the disease. The plots also help in inferring that although the risk of infection of a healthy exposed person is high from droplets ejected from a higher C_v valued patient owing to higher n_{max} and E_v, the risk is not zero from asymptomatic or weakly infected patients.

5.4.2. Motion of respiratory virulets

In addition to the infection potency of the virulets, the infection risk of an exposed person also depends on the spatial distance of exposure from the infected person, i.e., the spreading distance of the virulets. **Figure 5.1** schematically shows the motion of the virulets ejected during a sneeze in different pathways for d of 1–500 µm – (i) *floating* in air and travelling far away, (ii) *falling* to the ground at a shorter distance, and (iii) *fleeting* virulets travelling to an intermediate distance before sinking. Such different modes of transmission of the virulets are governed by its characteristic flow dynamics. Here, we have numerically simulated the micro virulets ejection of different size ranges through a human sneezing process and its subsequent

spreading in open air, as described in **Figure 5.4**. In order to mimic the initial sneezing airflow, we consider a Gaussian velocity distribution function, as described in the previous section. In accordance with the common sneezing conditions reported by the previous study[397], the time of ejection of the droplets and maximum amplitude of the function are taken as 300 ms and 9.2 m/s, respectively.

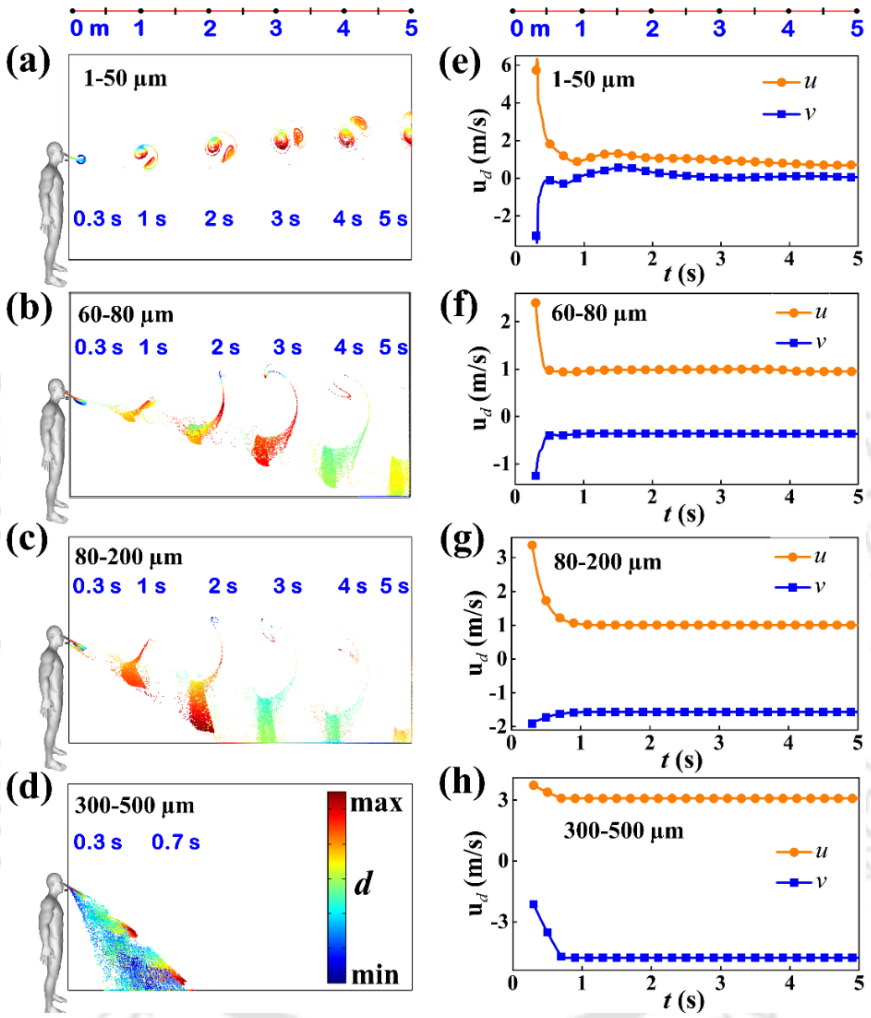

Figure 5.4. Plots (a)–(d) show the flight trajectory and (e)–(h) shows the corresponding velocity profiles of the virulets expelled from the sneeze of a SARS–CoV–2 infected person, taking droplet size ranges of 1–50 µm, 60–80 µm, 80–200 µm, and 300–500 µm, respectively. The color bar in subplot (d) shows the dimension range of the simulated virulets, the terms 'min' and 'max' indicate least virulet diameter and the maximum virulet diameter of that droplet range, as considered in subplots (a) to (d).

For each range, 5000 number of virulets are taken to emulate the actual concentration during a human sneeze, and the same is at par with a previous study[397]. For all the simulation studies, external airflow is maintained at light breeze of 1 m/s, moving from left of the solution space to the right, maintaining a laminar flow. The flow profiles of such systems have been simulated for different sized droplets for a time period of 5 s. A set of four droplet size range is considered to review the landing trajectory and flow velocities at different time period until 5 s. The typical

droplet size ranges taken are, 1–50 µm, 60–80 µm, 80–200 µm, and 300–500 µm, as shown in the **Figure 5.4(a)−5.4(d)**. The color bar in **Figure 5.4(d)** represents the corresponding size of the virulets considered for the study. **Figure 5.4(e)–5.4(h)** shows temporal variations of the *x* and *y*–directional velocities of 1–50 µm, 60–80 µm, 80–200 µm, and 300–500 µm sized virulets, respectively.

Figure 5.4(a) shows the flow trajectory of 1–50 µm sized virulets, which suggests that these virulets are likely to travel a longer distance, larger than 5 m in 5 s time following a re–circulatory flow pattern, as can be found in the image set of **Figure 5.5(a)**. Interestingly, the virulets form trajectories resembling the rotating fluid vortices, when they float in the air. **Figure 5.4(e)** suggest that the *x*–directional velocity, u, of the virulets is maximum at nose inlet (at 0.3 s), which reduces progressively with the time and distance travelled. On the other hand, the *y*–directional velocity of the virulets, v, is towards the ground (less than 0) during the ejection. With the progress in time, the virulets become air bound as v increases with time. The figures together suggest that these tiny virulets drift in forward direction from the inlet and drive upwards during its pathway with increase in v, and do not settle to the ground easily. Therefore, the virulets in this range remain suspended in the air for long time and can transit to a far distance with the airflow. The ejection of fluid into the computation domain develops local counter rotating twin vortices in the nearby space, as shown in **Figure 5.5**.

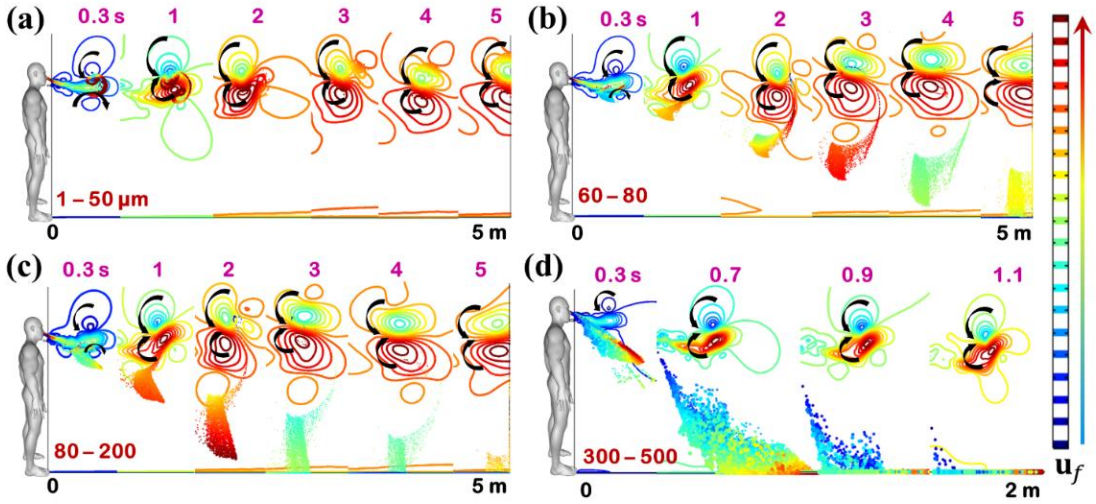

Figure 5.5. Image sets show the velocity contour of the virulets sized (a) 1–50 µm, (b) 60–80 µm, (c) 80–200 µm, (d) 300–500 µm.

Such local wakes infused with virulets are convected further by the laminar flow of the surrounding fluid. However, the virulets to follow the fluid vortices is decided by the forces acting on it– inertia, drag and gravity force. The smaller droplets by virtue of inertia tends to float along with the fluid vortices mimicking the circulations, which lifts the tiny droplets to

travel to long distances, as shown in **Figure 5.5(a)**. The detailed analysis of the forces acting on the virulets are discussed further in the script. **Figure 5.4(b)** shows the trajectory of the 60–80 µm sized virulets and the corresponding temporal variations of the *x*– and *y*–directional velocities are shown in **Figure 5.4(f)**. The **Figure 5.4(b)** suggests that the spreading distance of these virulets after 5 s are relatively smaller than in figure 5.4(a). The figure also shows that the bigger virulets in the range settles on the ground at much shorter distance while the smaller ones can still become air borne within 5 m. Again, the **Figure 5.4(f)** shows a positive v at the downstream indicating an upward drift for the smaller virulets in the range, following the rotation of the fluid vortices, as portrayed in **Figure 5.5(b)**. **Figure 5.5(b)** also illustrates that the bigger virulets in the 60–80 µm range departs from the vortex street, after a while, towards the downstream. This is due to the dominance of gravity on the bigger virulets governs its trajectory with the course of time. Similarly, the motions of 80–200 µm sized virulets, as shown in **Figure 5.4(c),** illustrate that the virulets settles to the ground at a much shorter time as compared to the prior two cases. The corresponding velocity profiles in **Figure 5.4(g)** also suggest a substantial downward motion of the virulets. Unlike the prior two cases, these virulets sheds from vortex Street and moves away to the downstream rapidly, as shown in **Figure 5.5(c)**, whereas the smaller ones followed the fluid vortices. Interestingly, with further increase in the size to 300–500 µm, the virulets settles to the ground within a second of ejection, as can be found in **Figure 5.4(d)**. **Figure 5.5(d)** also shows that the virulets escape the fluid vortices and settles to the ground immediately after ejection from the nose. The corresponding velocity profiles in **Figure 5.4(h)** also confirms the sharp decline in u and v within a short time.

Concisely, the simulations suggest that, with increase in the virulet size from 1–50 µm to 300–500 µm, the settling distance decreases from more than ~ 5 m in 5 s to less than 1.5 m in ~1 s, respectively. The flow trajectory of the virulets ejected during coughing is illustrated in **Figure 5.6**. The simulations help in differentiating the *floating* virulets to be with $d < 70$ µm, *fleeting* to be with $70 \le d \le 200$ µm, and *falling* to be $d > 200$ µm. Remarkably, the simulations suggest that they can travel a much larger distance than the standard protocol of 2 m set for physical distancing and can be one of the major reasons behind the community transmission with the high viral potency. In this regard, one may easily envision that the *floating* virulets may exclusively adopt the airborne mode of disease transmission while the *falling* ones may facilitate droplet or fomites mode of disease transmission. The *fleeting* mode may contribute towards both the modes. The images in the **Figure 5.4** and **Figure 5.6** illustrates that an exposed person at similar height or more than the infected one is vulnerable to the passing

virulets even at a distance of greater than 2 m when the virulets are airborne. However, the children are more susceptible to the virulets even at the close vicinity of the infected person through the falling virulets. Moreover, the *floating* respiratory droplets ejected from an infected child can be sufficiently active to transmit infections to the adults through the air borne recirculation of the virulets.

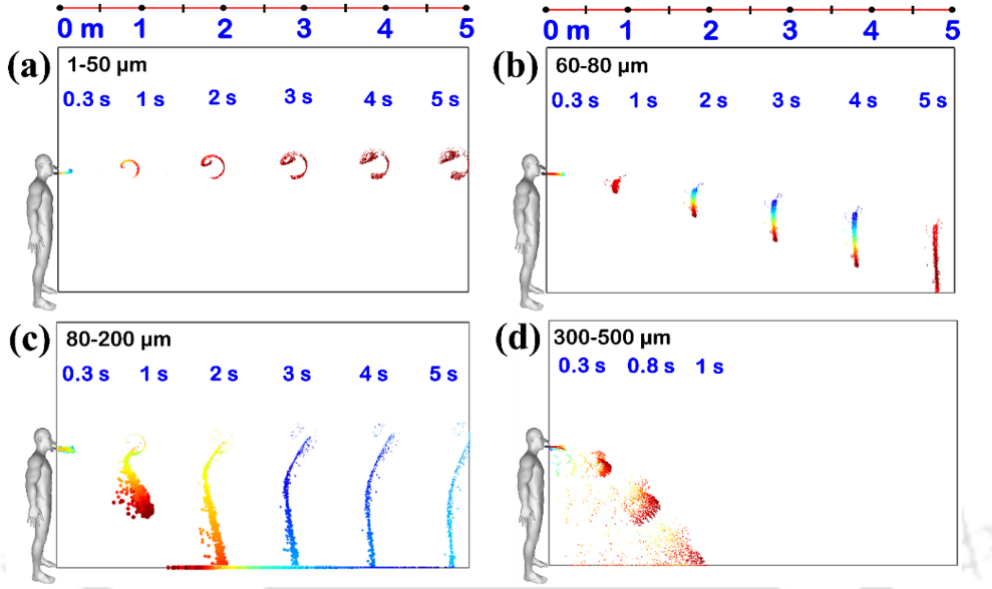

Figure 5.6. Plot shows the flow profiles of the virulets ejected from a human coughing process for *d* ranging from (a) 1–50 µm, (b) 60–80 µm, (c) 80–200 µm, and (d) 300–500 µm.

5.4.3. Analyses of force fields acting on *Virulets*

Detailed understanding of the droplet dynamics coming out of patients' nose or mouth is crucial to foresee the infectivity potential of these virulets. The virulets ejected during a sneeze, form a conical jet near the nose inlet and are mostly affected by the inertia force and thus travel along the direction of the initial velocity. As the virulets travel far from the nose inlet, the droplet velocity, $\mathbf{u}_d$, coupled to the surrounding fluid velocity, $\mathbf{u}_f$, decreases progressively from its maxima, as described earlier. The virulets in this regime experience a swirling flow during the motion due to the shearing of the ejected conical jet in the calm air around the inlet of the solution space[398]. As the particles move further, the size of the virulets determines its destination, as depicted in **Figure 5.7**. The component–wise force analyses along the normal directions of the Cartesian reference frame are done to explore the finer features of virulet dynamics. The trajectory of the virulets is mostly governed by three major factors – ejection inertia, downward gravitational pull, and viscous drag. Since the study is done employing virulets of a varying size range, the contribution of different forces alters with subsequent changes in its trajectories.

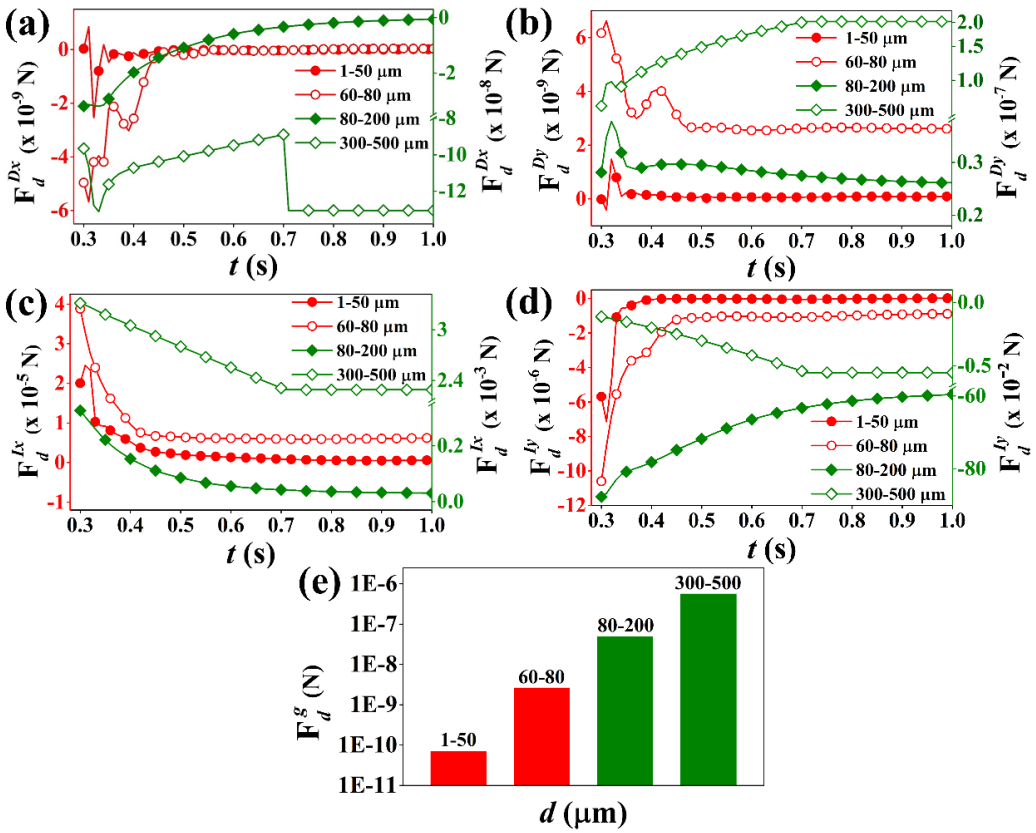

Figure 5.7. Plots (a) to (e) show the *x*–directional drag force ($\mathbf{F}_d^{Dx}$), *y*–directional drag force ($\mathbf{F}_d^{Dy}$), *x*–directional inertia force ($\mathbf{F}_d^{Ix}$), and negative *y*–directional inertia force ($\mathbf{F}_d^{Iy}$), and negative gravitational force ($\mathbf{F}_d^{g}$) acting on the particles of size ranges of 1–50 µm, 60–80 µm, 80–200 µm, 300–500 µm, ejected via sneezing.

Figure 5.7(a) and **Figure 5.7(b)** show drag force acting in horizontal (*x*–axis) and vertical (*y*–axis) directions, respectively, for different sized particles. In addition, **Figure 5.7(c)** and **Figure 5.7(d)** show the inertial forces in horizontal (*x*–axis) and vertical (*y*–axis) directions, respectively. The domination of gravitational pull with size can be substantiated from the **Figure 5.7(e)**. For 1–50 µm sized virulets, on comparing the two *x*-directional forces, i.e., $\mathbf{F}_d^{Dx}$ acting along the negative *x*–direction and $\mathbf{F}_d^{Ix}$ acting along the positive *x*–direction, it can be observed that the inertia of the virulets is relatively much higher than its drag force. Thus, the act of inertia is responsible for the faraway forward motion of these tiny virulets. Comparing all the *y*–directional forces, i.e., $\mathbf{F}_d^{Dy}$ acting in the upward *y*–direction, and $\mathbf{F}_d^{Iy}$ and $\mathbf{F}_d^{g}$ acting along the negative *y*–direction, it can be inferred that the act of gravity is relatively very small due to smaller size and act of inertia is very less due to lesser mass as compared to the drag force. Thus, the effective drag force in positive *y*–direction causes the lift of the virulets in the upward direction. Similar observations can be made for 60–80 µm sized virulets causing the lift and forward motion. However, the effectiveness of the resultant x and y directional forces

for 60–80 µm sized virulets are relatively minor than for 1–50 µm causing them to settle earlier. Comparing the x-directional forces for 80–200 µm and 300–500 µm sized virulets, the inertial force is comparatively smaller than its drag force along the x-direction. Also, the combined force of gravity and inertia along negative *y*–direction is higher than the upward drag force. Due to higher gravitational and inertial act along downward direction, these virulets tend to settle much faster as compared to the 1–50 µm and 60–80 µm sized virulets. Of course, the resultant act of the *x* and *y* directional forces is higher for 300−500 µm sized virulets owing to larger size and mass than for 80–200 µm, which explains the immediate fall of the 300–500 µm sized virulets after ejection as for 80–200 µm virulets.

5.4.4. Effects of multiple ejections and wind flow

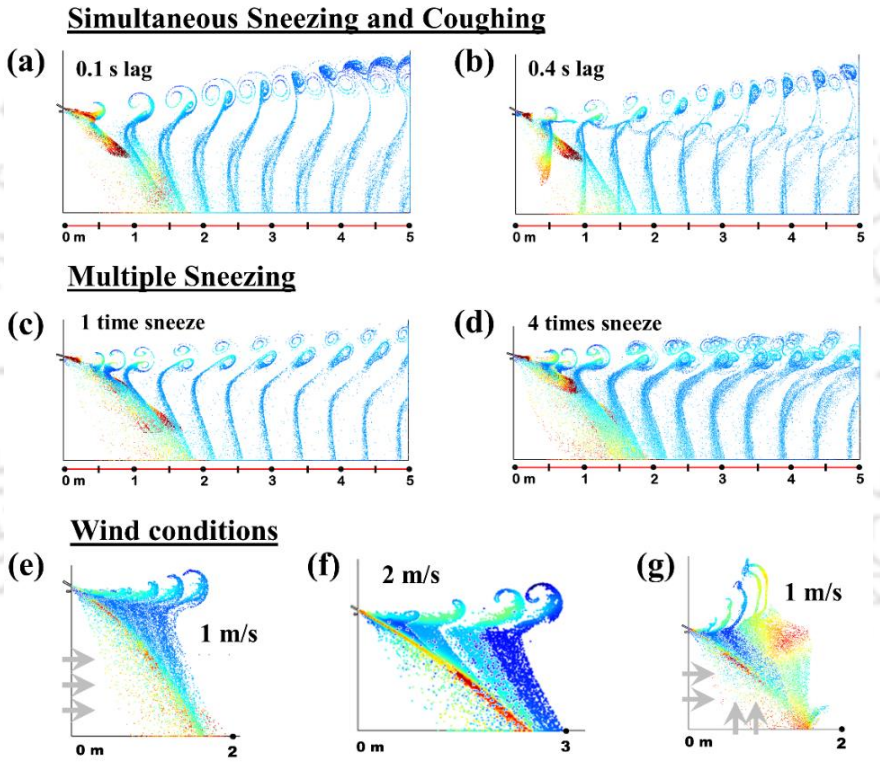

Figure 5.8. Results of different events that enhances the transmission of SARS–CoV–2 virulets, enhancing the community spreading of the disease. Plot (a) shows the spreading of virulets ejected during simultaneous sneezing and coughing from a SARS−CoV−2 infected patient with time lag between the two events be 0.1 s and (b) 0.4 s. Plot (c) shows the distribution of virulets during single sneezing and (d) sneezing for 4 times. The time frames from 0.3 s to 5 s has been combined in one image for all the cases. Plot (e) shows the dispersal of the virulets during external wind conditions of light breeze of 1 m/s from left to right, (f) breeze of 2 m/s blowing from left to right, and (g) light breeze of 1 m/s blowing left to right and bottom to top of the solution space respectively. The time frames from 0.3 s to 1 s have been combined in one image for (e) to (g).

Further, the infectivity risk from the traversing virulets can also augment by frequent medical factors like simultaneous sneezing and coughing by the infected person, heightened coughing or sneezing frequency, or by external influences like a windy day. The effect of these factors on the spreading of the virulets is depicted in **Figure 5.8**. The motion of infected

respiratory virulets in case of simultaneous sneezing and coughing from an infected person is shown in **Figure 5.8(a)** and **Figure 5.8(b)**. A range of 1–500 μm sized droplets, expelled from nose or mouth of an infected person with velocities same as for single sneezing or coughing processes has been considered for the study. It can be easily inferred from the figure that the density of the virulets in the given area is more during simultaneous sneezing and coughing process as compared to single sneezing or single coughing processes with increase in the time lag between the two processes from 0.1 s to 0.4 s, although the trajectory of motion remains the same. More the virulets are expelled by the infected person, more is the risk of spread of the infection.

Another such event of enrichment of infected droplets in a given area could be multiple ejections of the infected respiratory droplets, by an infected person. **Figure 5.8(c)** and **Figure 5.8(d)** highlight the droplet trajectories and the increase in density of the virulets in case of multiple sneezing from single sneeze to four times simultaneous sneezing. It can be depicted from the figure that with the increase in the sneezing frequency, the density of the virulets also increases in the given area. Consequently, anyone, irrespective of the height, exposed to the infected person's vicinity is at higher risk of inhalation of the expelled virulets and thus getting infected with the disease. Additionally, the external wind conditions can also augment the spreading of the virulets. The effect of the external wind speed on the spreading distance of the respiratory virulets is illustrated in **Figure 5.8(e)–5.8(g)**. Two different external wind speed conditions, light breeze (1 m/s) from left to right of the solution space, and angular light breeze (1 m/s) from left to right and bottom to top are considered for the analyses for 1 s time for virulets ranging from 1–500 μm. It can be observed that under light breeze conditions of 1 m/s, **Figure 5.8(e)**, the virulets do not traverse more than 2 m distance in 1 s time whereas it is 3 m for 2 m/s, shown in **Figure 5.8(f)**. In case of angular breeze condition, **Figure 5.8(g)**, the aerial transmission of the ejected virulets is amplified by the external breeze. Consequently, the natural pathways may also play an important role in the community transmission of the disease.

5.4.5. Effect of temperature and relative humidity on *Virulet* evaporation

The spreading of the virulets is a major factor in the community transmission of SARS–CoV–2, and it depends on how remote the respiratory droplets can travel carrying the infection causing agents. The time of fall of the virulets termed as settling time, t_s, decides how long it can survive freely before dropping to the ground. t_s of a virulet can be obtained by balancing the Stroke's friction force with the $\mathbf{F}_d^g$ experienced by the virulets during its flow[387], as given in eq (5.10),

$$t_s = \frac{h}{V_s} \tag{5.10}$$

Here h is the height at which virulets are ejected which is the height of the infected person – 1.5 m in this case, and V_s is the velocity of the virulet of radius R_0 at the time of fall – the settling velocity, given by eq (5.11)

$$V_s = 1.2 \times 10^8 \left(R_0^2 \right) \tag{5.11}$$

Remarkably, t_s of the virulets alters during its flight due to the modification in its size (R_0) owing to surrounding weather conditions such as *T* and *RH*. The variations in *T* and *RH* stimulate the miniaturization of the traversing virulets by virtue of evaporation. Accordingly, from eq (5.10), the reduction in R_0 enhances the t_s and hence the virulets can flow with air for longer time before falling to ground and spread faraway aiding the community transmission of the disease.

Figure 5.9(a) schematically shows the miniaturization of the ejected virulets to the evaporated virulets at *T* = 25℃ and *RH* = 50 %. It can be observed from the figure that the evaporation of the ejected droplets can change from the *falling* to the *floating* ones owing to the evaporation followed by miniaturization of the size. Such miniaturization increases the infection potency because, as discussed in Figure 5.2, the bigger droplets always carry a larger number of viruses, although they tend to settle easily on the surface under gravitational pull. However, if the *T* and *RH* of the surrounding facilitate the floating of such falling virulets due to rapid evaporation, the droplets with more virus loading may become air borne with a more potency towards viral transmission.

Further, the miniaturization of the ejected droplets also depends on the number of viruses loaded inside that droplet. If we assume the complete evaporation of an ejected droplet to be a state at which all the water content of the ejected droplet vanishes, then the miniaturized size of that ejected droplet is equivalent to the diameter corresponding to the total volume of the all the viruses contained in that particular droplet. **Figure 5.9(b)** shows the minimum possible diameter of the virulets after complete evaporation, d_e, for different C_v ranging from 10^6 to 10^9 copies/mL. For example, say for $C_v = 10^6$ copies/mL, a droplet of 100 µm can hold a maximum of 400 viruses, as can be found in Figure 5.2. After complete evaporation, the minimum possible miniaturized droplet size, d_e = 155 nm, which is the equivalent diameter to the volume of 400 number of 100 nm sized viruses loaded inside a 100 µm sized ejected droplet

for $C_v = 10^6$ copies/mL. However, the evaporation and subsequent state of miniaturization of d to d_e depends on t_s, as described in **Figure 5.9(c)**.

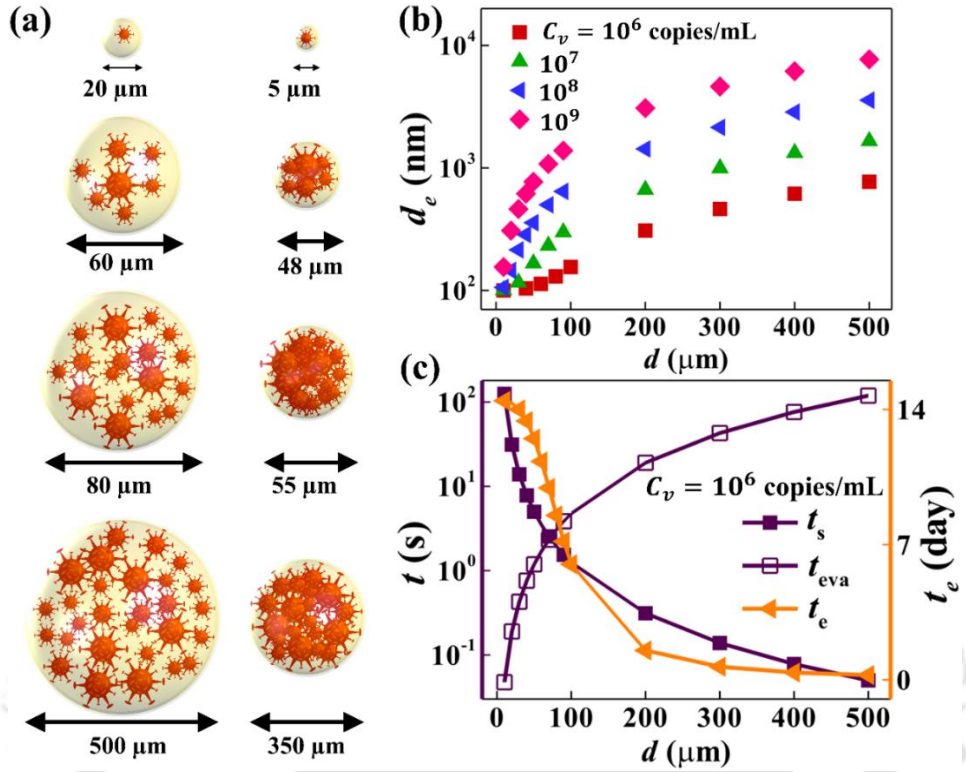

Figure 5.9. Shows the effect of evaporation on the virulets. Plot (a) schematically shows the miniaturization of the virulets at T = 25℃ and RH = 50%. Plot (b) shows the minimum possible d_e that an ejected droplet d can achieve after complete evaporation for different C_v ranging from 10^6 to 10^9 copies/mL. Plot (c) shows the comparison of t_s, t_{eva}, and t_e for $C_v = 10^6$ copies/mL.

Figure 5.9(c) shows a comparison of the evaporation time t_{eva} and the settling time of the miniaturized droplets t_e after evaporation. It can be observed from the plot that for d less than 80 µm, t_s s substantially larger than the t_{eva}. It means that the virulets get adequate time to evaporate before settling to the ground and thus these virulets are capable to reach its d_e at its corresponding t_{eva}. For d ranging from 80 µm to 200 µm, t_s is comparable to t_{eva} and thus the evaporation fate of these virulets to reach d_e depends on the external T and RH conditions. However, for d greater than 200 µm, t_s is much less than t_{eva}, which means that the virulets will not get sufficient time to evaporate much and will settle to the ground immediately after ejection. In addition, t_e is found to be in order of several days as shown in **Figure 5.9(c)**, which emphasize that the evaporated virulets that forms the *floating* miniaturized droplets are the bioaerosols that can suspend and circulate in air for days before falling down. Here, the

evaporated diameter d_e of the ejected droplets d is the final diameter, consisting of only the viruses inside it without any water content. To calculate d_e, the equivalent diameter of the total volume of all the viruses ($n_{\max}$) residing inside d for a particular C_v has been taken, as given in eq (5.12) below,

$$d_e = 2\times\left(\frac{3}{4\pi}\times n_{\max}\times V_{virus}\right)^{\frac{1}{3}} \tag{5.12}$$

where, V_{virus} is the volume of one virus of 100 nm diameter.

The time taken by d to reach d_e is the evaporation time t_{eva} of d and is calculated from eq (5.13) as described elsewhere[387],

$$t_{eva} = \frac{\left(\left(\frac{d}{2}\right)^2 - \left(\frac{d_e}{2}\right)^2\right)}{\theta\left(1-RH\right)} \tag{5.13}$$

where, $\theta = 4.2\times10^{-10}$ is a numerical pre-factor and RH is the relative humidity. For this work, t_{eva} is calculated at room temperature (25˚C) and RH of 50 %.

Seemingly, it is evident from the results shown above that the effect of evaporation plays a significant role in the spreading of the viral infections via virulets, which are also highlighted in the past literature [387]. In a tropical country like India, the climatic conditions relative to T and RH varies across the geography. The western regions experience high temperatures up to T = 50º C whereas the northern regions experience the cold weather throughout the year, and the coastal regions experiences high humidity as compared to the other states. Similarly, the climatic conditions of different countries across the globe also varies during different seasons throughout the year. These variations in the T and RH decides the rate of the evaporation of the virulets in a particular region and at a particular time of the year. Thus, the rate of the miniaturization of the virulets to evolve into bioaerosol also varies with geographic location and seasonal changes.

Figure 5.10 represents schematically the effect of change in the T and RH on the miniaturization of 100 µm sized virulet for various T and RH conditions. The figure shows that for T = 40º C and RH = 10 % the 100 µm can miniaturize to 1.1 µm in just 2 s whereas for T = 40º C and RH = 40 %, the *virulet* evolve to 6.24 µm in 4.5 s. Similarly, for cold conditions, like for T = 10º C and RH = 10 % the virulet evolve to approximately half of its size in 4.5 s and for T = 25º C and RH = 95 %, the miniaturization is minimum i.e. 77.43 µm in 5 s. Thus,

the figure illustrates that the hottest and low to moderate humid conditions suffer fastest bioaerosol formation.

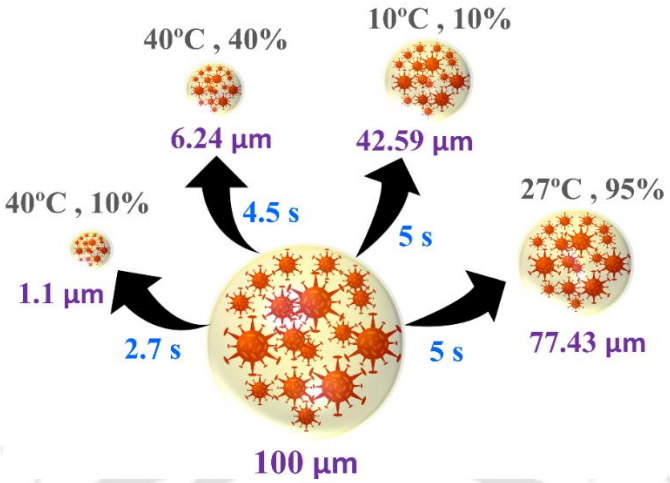

Figure 5.10. Schematically shows the effect of evaporation due to variation in *T* (in °C) and *RH* (in %) conditions on a 100 µm sized virulet.

5.4.6. Comparison of COVID–19 infection and *Virulet* evaporation

The transmission of COVID–19 in a particular region depends on a number of crucial factors like density of population[399], genetic makeup[400] and age of the people[401], metabolic co-morbidities[402], healthcare facilities[403], lifestyle factors of hygiene[404] and diet[405], susceptibility of the exposed person[406], administrative control[407], climatic conditions of the region[408], mutation of the virus[409], vaccination rate[410] and among others. Of all the factors listed one of the major causes of the bioaerosol formation is the meteorological conditions of a location which has been accredited to the occurrence of highly infectious second wave of SARS–CoV–2 pandemic. In view of this, we have voluntarily opted to map the effect of evaporation of the ejected respiratory droplets as an effect of external *T* and *RH* with the trend in the increase in infection rate at different geographical regions.

In this section, we focus on comparing two sets of parameters based on the *T* and *RH* conditions to understand such community transmission of the virulets. In the first set, we investigate the correlation between the evaporation driven rates of miniaturization of virulent $\left(\mathrm{d}m^R/\mathrm{d}t\right)$ with the rate of occurrence of confirmed cases of COVID–19 $\left(\mathrm{d}i^R/\mathrm{d}t\right)$. As a second case study, we show the correlation of evaporation rate (m) and absolute number of confirmed cases (i). The entire comparison analyses are made considering three most COVID-19 infected places, Maharashtra, Karnataka, and Delhi, from India and three major cities across the globe, Los Angeles, São Paulo, and Paris. The study is envisioned to predict the future occurrence of COVID waves based on the *T* and *RH* of the various places across the globe. The data for

number of confirmed cases of COVID infection have been collected from two authentic websites; (i) https://www.covid19india.org/ for Indian regions, and (ii) https://www.worldometers.info/ for the world data. The rate of miniaturization of the virulet in air due to evaporation has been calculated from eq (5.14), given by Williamson and Threadgill[411],

$$\frac{\mathrm{d}d}{\mathrm{d}t} = \frac{-4M_L D_v f}{d\rho_L RT}\Delta P\left(1+0.276R_e^{0.5}S_c^{1/3}\right). \tag{5.14}$$

Here, M_L, ρ_L, T, $D_{v,f}$, R , Δp, Re and Sc are the molecular weight of water, density of water, average absolute temperature, average diffusion coefficient for vapor molecules at T, gas constant, difference between the vapor pressure near d and that in the ambient atmosphere, Reynolds number, and Schmidt number, respectively. The T and RH data for the calculation are collected from the meteorological website, https://www.timeanddate.com/, for the respective date on which confirmed cases has been taken for the study. It may be noted here that the parameters we are exploring in this study are not the only factors for the spreading of the pandemic. There are other multiple scientific, mutational, physiological, environmental, and administrative factors that determine the spreading of the infection. However, despite having the influence of such parameters, we observe a very faithful correlation between $\left(\mathrm{d}i^R/\mathrm{d}t\right)$ and $\left(\mathrm{d}m^R/\mathrm{d}t\right)$.

Figure 5.11(a)–5.11(f) show the case study for three major COVID –19 affected regions in India – Maharashtra, Karnataka, and New Delhi, respectively. **Figure 5.11(a)** shows the rate of miniaturization of the ejected droplets $\left(\mathrm{d}m^R/\mathrm{d}t\right)$ and the rate of change of confirmed COVID–19 cases $\left(\mathrm{d}i^R/\mathrm{d}t\right)$ against different dates counted from June 2020 to June 2021 to study the first and second waves. It should be noted here that the dates considered for the study are in accordance to the rising of first and second COVID–19 waves at that particular location. It is evident from the figure that the trend in $\left(\mathrm{d}m^R/\mathrm{d}t\right)$ matches fairly with $\left(\mathrm{d}i^R/\mathrm{d}t\right)$. The plots also show a time lag between the rate of infection $\left(\mathrm{d}i^R/\mathrm{d}t\right)$ and rate of miniaturization of the droplets $\left(\mathrm{d}m^R/\mathrm{d}t\right)$. Intuitively, one can easily envisage that this lag is correlated to the formation of bioaerosol first and then the spreading of the infection leading to the increase in the cases. In a way, such an observation justifies that the possibility of the formation of bioaerosol due to the variation in T and RH at different times of a year and different regions.

In a different case analysis, **Figure 5.11(b)** shows the comparison of occurrence of COVID–19 cases *i* and the evaporation rate of the droplets *m*. It can be seen from the figure that in this case too, the trend in the increase in COVID–19 infection is comparable with the evaporation rate curve. The dotted curves are the extrapolated arches of the rise in COVID–19 cases in accordance with the evaporation rate calculated from July 2021 to December 2021, as discussed later. **Figure 5.11(c)** and **Figure 5.11(d)** show similar analyses for Karnataka, and **Figure 5.11(e)** and **Figure 5.11(f)** show analyses for Delhi. These cities show a very similar trend of infection profile against evaporation rate and droplet miniaturization. For both Karnataka, shown in **Figure 5.11(c)**, and New Delhi, shown in **Figure 5.11(e)**, the rate of infection $\left(\mathrm{d}i^R/\mathrm{d}t\right)$ follows the rate of miniaturization of the droplets $\left(\mathrm{d}m^R/\mathrm{d}t\right)$ and these observations substantiate that the miniaturization of the virulet size and formation of bioaerosol directs the infection rate in the region. **Figure 5.11(d)** and **Figure 5.11(f)** show a good agreement of COVID–19 cases *i* with the evaporation rate of the droplets *m* for Karnataka and New Delhi. A small deviation is observed for the case of Karnataka and the same might have happened for other causes those have not been considered for the present study.

Now since the results established the faithfulness of the model for the community spreading of the infections during the waves of the pandemic, we attempt to predict the number of COVID–19 cases in the near future. For the prediction algorithm, we follow a higher order polynomial curve fitting analysis of the number of absolute cases *i* vs. days. The data of absolute COVID–19 cases farthest from May 2020 to June 2021 are taken as a reference for developing the polynomial fitting and the same is subsequently extrapolated for the prediction of future COVID–19 cases. The broken line portion in the plots of the **Figure 5.11(b), Figure 5.11(d), Figure 5.11(f), Figure 5.11(h), Figure 5.11(i),** and **Figure 5.11(l)** show the prediction data for upcoming possible COVID–19 cases. The values for the *T* and *RH* from July 2021 to December 2021 are taken as an average of last three years data for that specific region. We also investigated cases of three foreign cities Los Angles, São Paulo, and Paris, since the weather conditions are markedly different in the Indian cities and abroad. The plots suggest that despite a significant demographical change there is a direct correlation of rate of infection $\left(\mathrm{d}i^R/\mathrm{d}t\right)$ with the miniaturization of the droplets $\left(\mathrm{d}m^R/\mathrm{d}t\right)$. Similar correlation is also observed for absolute infection *i* against rate of evaporation *m*.

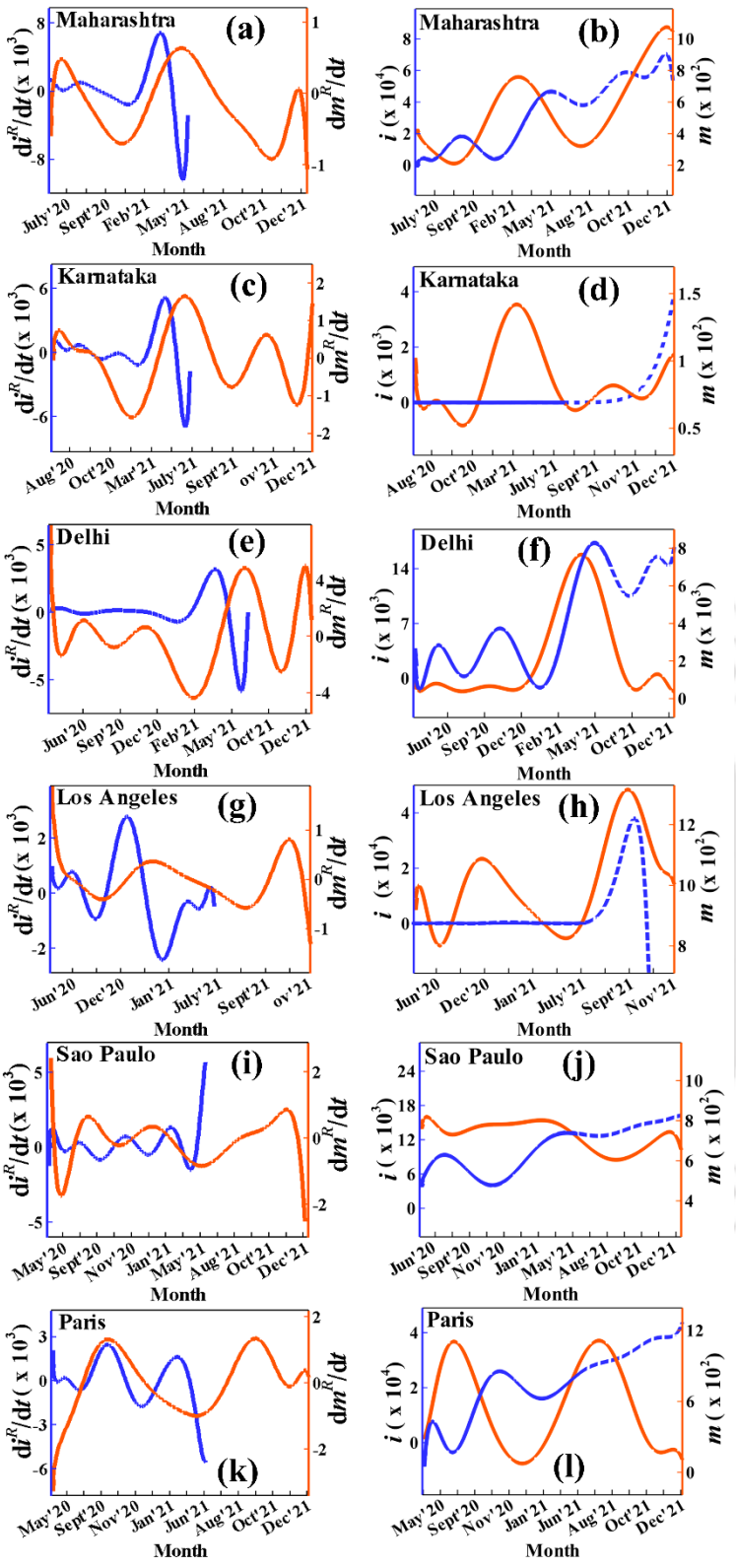

Figure 5.11. Shows the comparison of rate of miniaturization $\left(\mathrm{d}m^R/\mathrm{d}t\right)$ of 100 µm sized virulet with the rate of change of the confirmed COVID–19 cases $\left(\mathrm{d}i^R/\mathrm{d}t\right)$, and the evaporation rate m and confirmed cases i to predict the expected further occurrence of covid cases in near future. Subplots (a) –(f) show the trend for the three most COVID-19 affected regions in India– Maharashtra, Karnataka, and Delhi, respectively and subplots (g)–(l) show three most COVID-19 affected locations in world – Los Angeles, São Paulo, and Paris, respectively.

Figure 5.11(g), Figure 5.11(i), and **Figure 5.11(k)** show comparison of rate of infection $\left(\mathrm{d}i^R/\mathrm{d}t\right)$ with the miniaturization of the droplets $\left(\mathrm{d}m^R/\mathrm{d}t\right)$ for São Paulo, Los Angles, and Paris, respectively. These plots show a close match with occasional deflection, which may be attributed to other pandemic causes. **Figure 5.11(h), Figure 5.11(j),** and **Figure 5.11(l)** show correlation between trend in increase in COVID–19 cases *i* and evaporation rate *m*. In this absolute case analyses too, we find a close mapping between the curves.

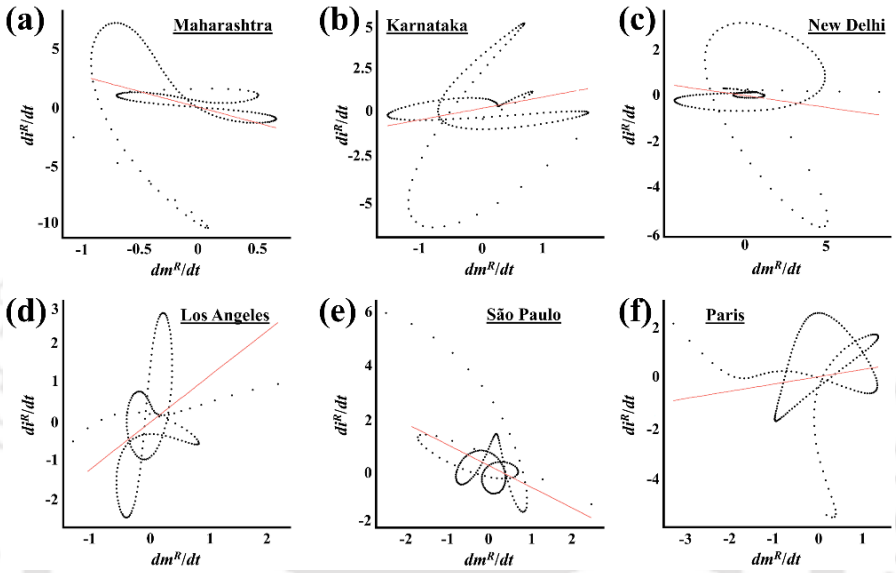

Figure 5.12. The plot shows the non–linear correlation plot of $\left(\mathrm{d}i^R/\mathrm{d}t\right)$ against $\left(\mathrm{d}m^R/\mathrm{d}t\right)$ for the six selected places.

In order to evaluate the degree of correlation between $\left(\mathrm{d}i^R/\mathrm{d}t\right)$ and $\left(\mathrm{d}m^R/\mathrm{d}t\right)$, we plotted the non-linear correlation for all the six places for the entire time period of infection. **Figure 5.12** shows the non-linear correlation plot for the six places. The non-linear correlation was evaluated using the non-linear estimator 'nlcor' package of the R programming language[412]. It implements a heuristic approach to evaluate the non-linear correlation between the two given parameters and returns a *p*-value as a factor to signify the degree of correlation. It identifies piecewise linear correlations of the local regions to estimate the overall non-linear correlation. The correlation estimate (*nlcor* value) and *p*-value obtained for the six selected regions are listed in **Table 5.3**. The correlation plot and Table 5.3 shows that the rate of infection and rate of miniaturization of the *virulets* for all six locations are significantly correlated as the *p*-value is less than the threshold ($p < 0.005$)[413]. Therefore, it is justified to claim that the rate of occurrence of infection cases in a particular location is also a factor of the rate of miniaturization of the ejected *virulets* driven by the geographical conditions of *T* and *RH* of the corresponding location.

Table 5.3: Shows the *nlcor* value and *p*–value for the non–linear correlation of $\left(\mathrm{d}i^R/\mathrm{d}t\right)$ against $\left(\mathrm{d}m^R/\mathrm{d}t\right)$ for the six selected places.

Location	*nlcor* value	*p*–value
Maharashtra	0.363	0.00
Karnataka	0.255	0.00
New Delhi	0.163	0.02
Los Angeles	0.401	0.00
São Paulo	0.469	0.00
Paris	0.158	0.03

The above results enlighten the role of T and RH on the evaporation driven miniaturization of the virulets and its significant correlation with the trend in the occurrence of the infection cases in the six different geographical locations considered in the present study. In view of that, we have done CFD simulations considering T and RH for six different places considered in the study, as shown in **Figure 5.13**, to elucidate the transmission of the miniaturized virulets and to mark the optimal whether conditions that favour the maximal transmission of the virulets to far distances. Here, we simulated the spreading distance of the ejected virulets on certain weather conditions for six different places, as shown in **Figure 5.13**.

The farther reaching virulets can be more potent to spread the infection to more people, however, if the virulets are settling at a shorter distance, the infection risk can be low but not absolutely zero. For the simulations, we kept the *T* of a particular region to be constant to its minimal and maximum limit and varied the *RH* from its lowest to the highest value, as reported on meteorological websites. In the subplots (a)–(l) of **Figure 5.13**, the high–risk *RH* has been marked in red and the low–risk *RH* is marked in green color.

If we consider the case of Maharashtra, it can be seen that for the low T = 25ºC , if RH < 50%, the virulets could float in the air and reach to farther distances in less time as compared to the settling of the virulets as observed for RH > 50%, as shown in **Figure 5.13(a)**.However, with the increase in T = 34ºC, the virulets could float even for larger *RH*, as shown in **Figure 5.13(b)**. Thus, there is a high probability that if the *RH* reaches lower than 50% in Maharashtra at any time of the year, there is a higher possibility of an increase in infectivity ratio. Similarly, in Karnataka, there is a high risk of an increase in infectivity whenever the RH conditions reach below the semi-humid level, as shown in **Figure 5.13(c)** and **Figure 5.13(d)**. Comparatively, if we consider New Delhi, the high–risk *RH* limit in colder days is found to be very lower than in warmer days, as shown in **Figure 5.13(e)** and **Figure 5.13(f)**. Similarly, in Los Angeles, the high–risk *RH* limit is found to be very lower on colder days and it reaches semi–humid conditions with an increase in temperature, as shown in **Figure 5.13(g)** and **Figure 5.13(h)**.

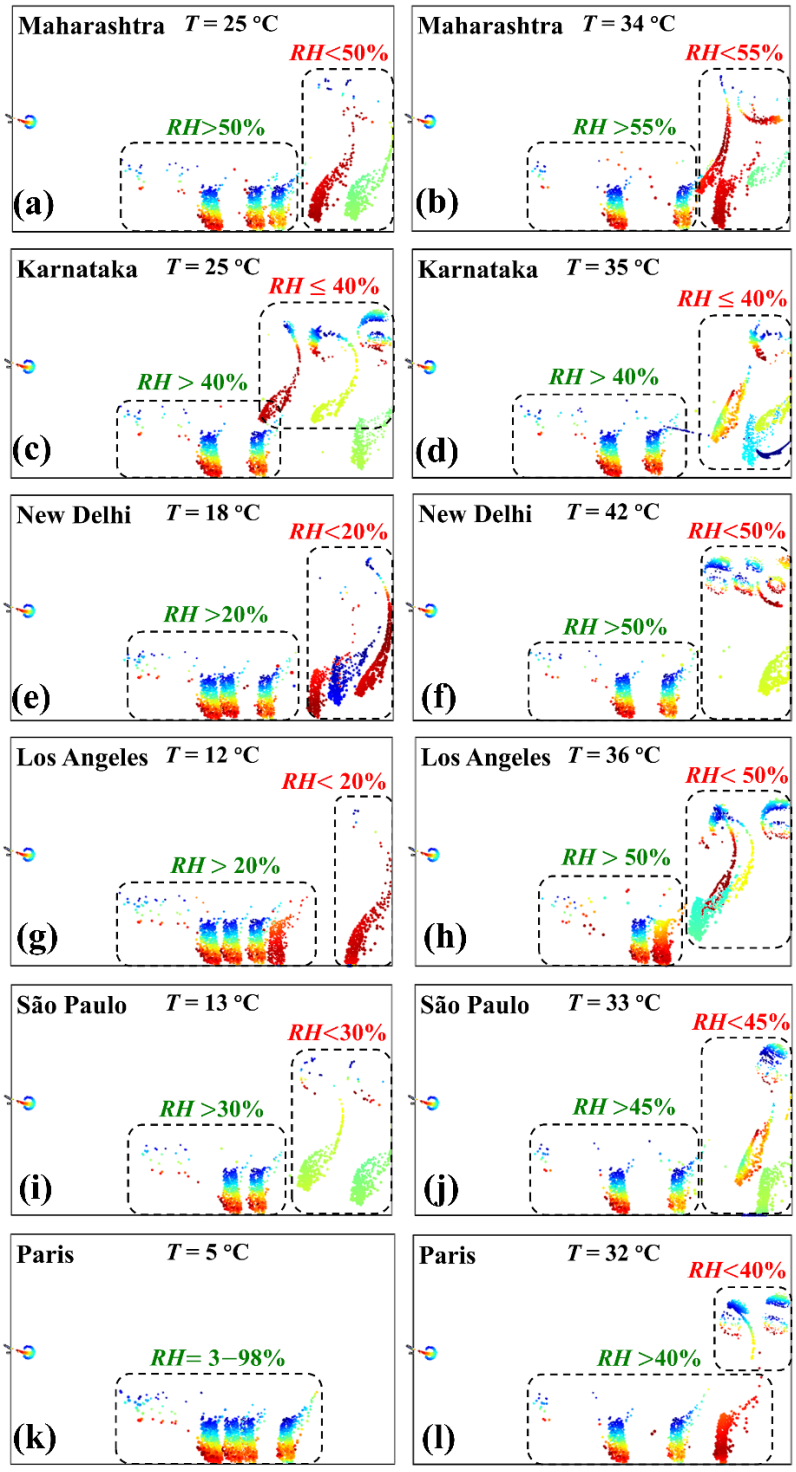

Figure 5.13. The plot shows the high and low–risk weather conditions at which maximum transmission of the virulets is probable at different geographical locations.

In Sao Paulo, the high *RH* limit is found to vary minimally cold and warm, as shown in **Figure 5.13(i)** and **Figure 5.13(j)**. In Paris, it was found that the lower the temperature, the risk level reduces which probably reduces the infectivity ratio, however, the limit increases to the semi-humid limit with an increase in temperature, as shown in **Figure 5.13(k)** and **Figure 5.13(l)**. Conclusively, it can be illustrated from all the subplots in **Figure 5.13** that both cold–dry and

warm–semi humid conditions could be attributed to the major contributor of virulet miniaturization and transmission-based mediator of high infectivity ratio. Though, the risk of infection transmission in other weather patterns at different geographical locations is absolutely not zero. Thus, the present work shows a satisfactory resemblance to the weather patterns for influenza flu transmission as reported in the prior studies[414,415].

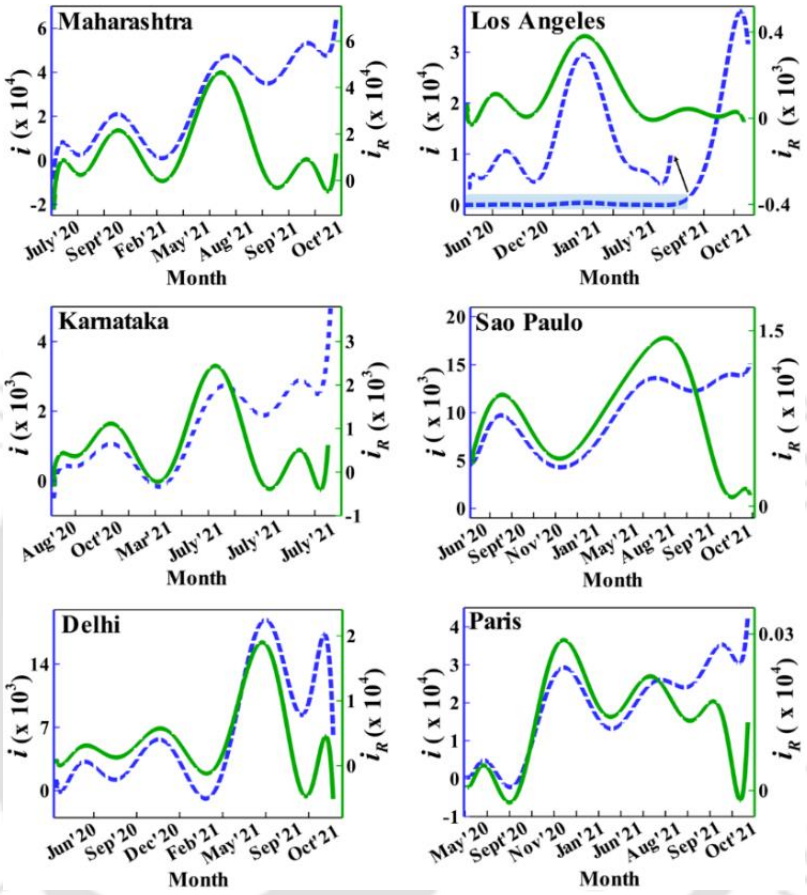

Figure 5.14. The plot shows the similarity between the predicted COVID–19 infection cases (*i*, broken blue line) and the reported COVID–19 infection cases (i_R, solid green line).

Further, we have shown the authenticity of the claimed evaporation model by comparing the predicted COVID–19 infection cases (*i*, showed in the broken blue line in **Figure 5.14**) with the reported COVID–19 infection cases (i_R) for the first and second waves of the infection in the last two years for six different geographical regions. **Figure 5.14** shows the match between the predicted and reported COVID–19 infection cases for the mentioned time period. It can be inferred from the figure that the trend in the occurrence of the reported infection waves in several regions matches well with the COVID–19 infection waves predicted in the present study. The predicted model shows nearly the same number of waves, including both weak and intense peaks, occurring at a similar time of the year as it is reported during the first and second waves of COVID-19 infection. Although, there is a lag in the intensity of the real infection

cases as compared to the predicted one, which may be attributed to other additional carriers of transmission like viral seeding, population susceptibility, person-to-person contact, vaccination rate, face and mask hygiene, and others, which varies over the year and has not been added to the present study as the aim of the work is to understand the effect of *T* and *RH* only, on the miniaturization of the *virulets* and to predict its transmission with CFD study. Hence, witnessing **Figure 5.11–5.14**, it is worth inferring that like with other parameters, evaporation is obviously one of the major factors in the transmission of the COVID–19 via miniaturization of the respiratory *virulets*.

Concisely, despite having multiple deciding factors for COVID-19 community transmission, the present study unveils that T, RH, and subsequent kinetics of droplet evaporation leading to bioaerosol formation can be one of the very effective tools in predicting the future waves of a viral pandemic.

5.5. Conclusions

The present work compiles the various possible fluid dynamical causes of the community transmission of the highly contagious SARS–CoV–2 infections. The detailed calculations of the viral content inside the colloidal biofluid microdroplets of varying sizes, the *virulets*, ejected during the respiratory activities like sneezing and coughing gives an idea of airborne and/or droplet modes of the transmission of the disease. Further, the flow trajectories of the respiratory droplets have been simulated employing the fluid particle tracing physics, to manifest the settling distance of the *virulets* and to understand the role of bioaerosol transmission in the spreading of the disease. In relevance, it is to be mentioned that since the inception of the pandemic a few reports on droplet or bioaerosol transmission are published from last year. Most of the reported articles explore the droplet movement in the air considering only Newton's second law of motion[416,417] neglecting finer features of fluid dynamics, as described in the present study. The flow profiles of the *virulets* shown in Figure 5.4 prove that the prescription of 2 m of physical distance to control the SARS–CoV–2 infections are only applicable to the large *virulets* whereas the bioaerosol is effective enough in spreading the disease to longer distances also. Furthermore, this work explicitly addresses the effect of gravity, drag, and inertial forces on the *virulets* of various sizes, and clearly explains the extent of spread of a *virulet* of interest. Likewise, the events like increased frequency of *virulet* ejection or a windy day which further enhances the spread of the disease are also discussed precisely.

Additionally, the work reveals the influence of geographical conditions on the transmission of the *virulets* at a given location. Here, the effect of *T* and *RH* has been examined [418-420] to measure the rate of bioaerosol generation owing to the effect of evaporation, attributed to the occurrence of the second wave of SARS–CoV–2 infection. In Figure 5.11, reported infection cases of six different locations – Maharashtra, Karnataka, New Delhi, Los Angeles, São Paulo, and Paris have been mapped with the evaporation driven miniaturization rate of the *virulets* of that location for the time period of the first wave of COVID-19 infection. Interestingly, the reported infection waves show a similar trend in occurrence as that of the rate of miniaturization for a given location. To further justify the quantitative relation, in Figure 5.12 and Table 5.2, a non-linear correlation analysis of the curves shows the *p*–value is nearly zero for all the considered locations, which proves the significant relationship between the two. The CFD studies that reported in Figure 5.13 prove that both the cold-dry and warm-semi humid condition enhances the transmission of the *virulets* to long distances, attributed to the increase in infectivity ratio for that location. Importantly, the CFD simulation with varying *T* and *RH* parameters for all the cities predicted a critical *T* and *RH* value that varies from one city to another. This CFD information, can further be used for studying similar disease spreading. We extended the study to predict the future infection waves based on the *T* and *RH* mediated miniaturization of the *virulets* and later matched with the reported infection cases of the second wave of COVID–19 infection. The curves matched well in terms of frequency and time period of occurrence of the second infection wave but with a compromise of the intensity, which could be attributed to the lack of consideration of various other factors of the infection in that region.

In a way, the study establishes the importance of *T* and *RH* of a given location on the spread of the infection. The study also paves the pathway to future research on explaining the most accurate method of bioaerosol formation from sneeze/cough droplets considering the various other environmental conditions and effects of elements of the colloidal microdroplets. It will also help in explaining the most realistic dynamics of bioaerosol motion and subsequent community transmission.

भारतीय प्रौद्योगिकी संस्थान गुवाहाटी
Indian Institute of Technology Guwahati

Chapter 6

Summary and Future scopes

Summary

Conclusively, this thesis highlights the utilization of unique and excellent properties of plasmonic metal nanoparticles and nanoparticle assemblies for ultrasensitive and selective detection of diseases utilizing LSPR and SERS. Additionally, the required mathematical models were developed for deciphering the underlined theory of the as obtained plasmonic signals of the nanostructures synthesized and utilized for the biosensing applications. Also, numerical modelling was performed for interpreting the community transmission of airborne viral diseases. The major challenges faced, assumptions made, and the conclusions drawn from each technical chapter are narrated chapter wise as follows:

The chapter second proposes a methodology of early and non–invasive screening of cervical cancer at patients' sites. Herein, a cervical cancer specific urinal protein–Protein Phosphatase–1–Gamma 2 (PP1Ɣ2), also named Novel Cancer Biomarker (NCB), has been recognized as a potential biomarker for the disease and has been utilized further for the detection of cervical cancer utilizing LSPR based plasmonic nanosensor. The concentration of NCB present in various urine samples depends on stages of cervical cancer, time of sample collection, hydration-dehydration of the patient, and more. Additionally, the urine samples of different patient may have different interfering agents that can lead to further complexity in detection. Development of plasmonic sensing unit for identifying presence of urinary protein NCB from urine sample was a real challenge and that has been optimized in this chapter. For developing the POCT prototype, gold nanoparticles were first immobilized with anti–PP1Ɣ2 antibody and was allowed to interact with PP1Ɣ2 antigen present in the urine samples collected from the patients. The epitope-paratope interaction between antigen and antibody leads to a significant shift in the LSPR response of the gold nanoparticles, which was marked as a tool for the screening of the positive and negative cases of the cervical cancer.

The third chapter focuses on the fabrication of a facile dimeric gold nanoparticle, named as nanotwins, based plasmonic glass substrate and its utilization for the development of a POCT prototype for sensitive and specific detection and quantification of the Escherichia Coli (EC) as a measure to diagnose UTI cases. Fabrication of a plasmonic glass substrate with maximum distribution of Au NTs was a real challenge for the study. With trial and error, the process of plasmonic substrate development and maintaining uniformity in different batches were achieved. Deciphering the mechanism of enhanced sensing efficiency with Au NT surface was

cumbersome and simulations were done to decipher the underlying physics. The prepared nanotwin plasmon substrates are found to produce seven-fold enhancement of the SERS response as compared to the isolated gold nanoparticle substrate. Further, the nanotwin substrates were immobilized with aptamer specific to EC and then allowed to interact with EC present in the analyte, both urine and aqueous media. The enhancement in the absorbance as well as spectral shift towards the lower wavelength was observed as a result of interaction. Also, the proposed nanotwin substrate showed high specificity and selectivity against Staphylococcus aureus, Enterococcus Faecalis, and Klebsiella pneumonia. An electronic set up was made to transduce the change in LSPR signal for the POCT applications.

In the fourth chapter, SERS nanoprobes has been synthesized using bimetallic nanostructures including gold nanorods shelled with silver. Choosing right chemical synthesis procedure for the nano shelled particles were the challenging task of this particular chapter and the same has been achieved by optimizing chemical synthesis process parameters. Obtaining right Raman signal depends on concentration of the plasmonic nanoparticle, amount of laser incidents upon the sample, focusing the laser on the sample rightly, and more. A lot of trials have been done to understand the right parameter for obtaining the Raman signals and thereby enhancing the detection efficiency. This bimetallic nanostructure showed a much enhanced LSPR property when immobilized with Raman reporter molecules like DTNB or 4ATP as compared to gold nanorods counterparts. These SERS nanoprobes were then immobilized with cholesterol oxidase or lipase for the detection of cholesterol or triglycerides utilized SERS intensity. The SERS experiments were carried out in solution phase in a liquid Raman set up, to avoid the site-specific differences that occur in case of solid substrates. The SERS intensities before and after the interaction of the cholesterol or triglycerides with its corresponding enzymes immobilized on the bimetallic nanoprobes were monitored and normalized to quantify various concentrations of cholesterol or triglycerides, respectively. An interference study with ascorbic acid, glucose, and sodium and potassium ion illustrates the selectivity and specificity of the sensor.

The fifth chapter compiles the various possible explanations as well as the causes of the community transmission of the highly contagious SARS–CoV–2 infections via sneezing/coughing, utilizing COMSOL Multiphysics based numerical simulations. Emulating sneezing and coughing by mathematical functions was a real challenge for this modelling, and Gaussian approximation was made to model sneezing and coughing in this chapter. The flow trajectories of different size of the virus laden respiratory droplets, named as virulets, have been simulated to manifest the settling distance of the virulets to understand the role of bioaerosol

transmission in spreading of the disease. The flow profiles of the virulets proves that the prescription of 2 m of physical distance to control the SARS–CoV–2 infection is only applicable to the large ones whereas the bioaerosol are effective enough in spreading the disease to longer distances also. Likewise, the events like increased frequency of virulet ejection or a windy day further enhances the spread of the disease. Additionally, the effect of T and RH has also been examined to measure the rate of bioaerosol generation owing to the effect of evaporation, attributed to the occurrence of second wave of SARS–CoV–2 infection, for three different cities in India and three highly infected cities across the globe. The results explained the role of geographical influence on the prevalence of the two pandemic waves due to climatic variations. Based on the available data, a trend for future incidence of the SARS–CoV–2 infection waves have been predicted.

Future Scopes

The works covered in this thesis would certainly open up the avenue for a number of significant applications and a few future scopes include,

- Possibilities of technology transfer to the relevant group for the deployment of the developed biosensors for improved version of the prototypes.
- Opportunities for collaboration with hospitals, health centers, and the research groups for extending the work for more clinical trials.
- Incorporation of additional functionalities to the developed sensing protocols for further improvement of sensitivity and selectivity based on clinical studies.
- The thesis extends a scope for development of similar portable optoelectronic devices for multiplexed biosensing approaches.
- The thesis also provides scope to further miniaturize the device prototypes for the ease of field applications.
- Finally, the thesis can serve as a valuable research resource that may be used by researchers of diverse fields.

भारतीय प्रौद्योगिकी संस्थान गुवाहाटी
Indian Institute of Technology Guwahati

LIST OF PUBLICATIONS

1. From Thesis

1. **M. Basak**, S. Mitra, et. al, Non-invasive Point–of–Care Nanobiosensing of Cervical Cancer as an Auxiliary to Pap–Smear Test, ***ACS Appl. Bio Mater., 2021, 4, 6, 5378–5390***.

2. **M. Basak**, S. Mitra, D. Bandyopadhyay. Pathways to community transmission of COVID–19 due to rapid evaporation of respiratory virulets, ***J. Colloid Interface Sci., 2022, 229–245.***

3. **M. Basak**, S. Mitra, M. Gogoi, S. Sinha, H B Nemade, D. Bandyopadhyay, Point–of–Care Biosensing of Urinary Tract Infections Employing Optoplasmonic Surfaces Embedded with Metal Nanotwins, ACS ***Appl. Bio Mater., 2022, 5, 11, 5321–5332.***

4. **M. Basak**, H B Nemade, D. Bandyopadhyay, Quantification of Cholesterol and Tri-Glyceride Employing SERS of Silver shelled Gold Nanorods. (***Manuscript under preparation***),

2. In Collaboration

1. **M. Basak**, S. Mitra, D. Bandyopadhyay, Plasmonic Graphene Nanocomposite as Efficient Photothermal Antibacterial Agent, IEEE Explore, ***2022 IEEE International Conference on Emerging Electronics (ICEE), Bangalore, India, 2022.***

2. J. Mahanta, **M. Basak** et. al, D. Bandyopadhyay, Enhanced Hydrogen Production during Electro-Oxidation of Ethanol using Plasmonic Gold Nanoparticles, ***Energy Technol., 2022, 10, 10, 2200134.***

3. Book Chapters

1. **M. Basak**, S. Mitra, D. Bandyopadhyay, Advances in Materials, Methods, and Principles of Modern Biosensing Tools in Biosensing, Theranostic, and Medical Devices, Springer, 33–57 (2022).

2. S. Mitra, **M. Basak**, D. Bandyopadhyay, Multifunctional gold nanoparticles for biosensing: effects of surface plasmon resonance, localized surface plasmon resonance, fluorescence, and aggregation, Elsevier, 331–366 (2021).

4. Patents

Granted (Indian)

1. **M. Basak**, S. Mitra, SK. Agnihotri, A. Jain, A. Vyas, MLB. Bhatt, R. Sachan, M. Sachdev, S. Maity, N. Kakoti, HB. Nemade, D. Bandyopadhyay, POCT Device to Detect Cervical Cancer Specific Biomarker ***(Patent Grant number: 374832)***.

Filed

2. **M. Basak**, S. Mitra, D. Bandyopadhyay, S. Sinha, Point-Of-Care Optoplasmonic Pathogen Sensor for The Rapid Detection of Urinary Tract Infection (Indian, *Application number: PCT/IN2020/051023)*.

3. **M Basak**, S Mitra, SK Agnihotri, A Jain, A Vyas, MLB Bhatt, R Sachan, M. Sachdev, S. Maity, N Kakoti, HB Nemade, D. Bandyopadhyay, POCT Device to Detect Cervical Cancer Specific Biomarker (WIPO, *Application number: 202231046148)*.

5. Conferences

1. **Mitali Basak**, Dipankar Bandyopadhyay, ***Non-invasive Point-of-Care Nanobiosensing of Cervical Cancer as an Auxiliary to Pap-Smear Test***, Poster, 35th International Papillomavirus Conference - IPVC 2023, Washington DC, US, Apr 17th–21st 2023.

2. **Mitali Basak**, Shirsendu Mitra, Dipankar Bandyopadhyay, ***Plasmonic Graphene Nanocomposite as efficient Photothermal Antibacterial Agent***, Poster, 2022 IEEE International Conference on Emerging Electronics, Bengaluru, India, Dec 11th – 14th 2022.

3. **Mitali Basak**, Dipankar Bandyopadhyay, ***Non-invasive Point-of-Care Nanobiosensing of Cervical Cancer as an Auxiliary to Pap-Smear Test***, Short presentation, GOLD 2022, Quebec City, Canada, Jul 18th–22nd 2022

4. **Mitali Basak**, Dipankar Bandyopadhyay, ***Non-invasive Point-of-Care Nanobiosensing of Cervical Cancer as an Auxiliary to Pap-Smear Test***, Poster Presentation, META 2022, Paris, France, Jul 19th – 22nd 2022.

6. **Mitali Basak**, Shirsendu Mitra, Dipankar Bandyopadhyay, ***Non-invasive Point-of-Care Nanobiosensing of Cervical Cancer as an Auxiliary to Pap-Smear Test***, Flash Talk Presentation, ICANN 2021, IIT Guwahati, India, Dec 13th–14th 2021.

7. **Mitali Basak**, Shirsendu Mitra, Dipankar Bandyopadhyay, ***Non-invasive Point-of-Care Nanobiosensing of Cervical Cancer as an Auxiliary to Pap-Smear Test***, Oral Presentation, CUChEAA 2021, University of Calcutta, India, Dec 18th –20th 2021.

References

1. Tsalis, T. A., *et al.*, *Corporate Social Responsibility and Environmental Management* (2020) **27** (4), 1617
2. Fraisl, D., *et al.*, *Frontiers in Public Health* (2023) **11**
3. Cooke, J., *et al.*, *BMJ open respiratory research* (2015) **2** (1), e000086
4. Bauer, M. F., *et al.*, *Clin. Chem. Lab. Med.* (1999) **37** (9), 855
5. Gialamas, A., *et al.*, *Fam. Pract.* (2009) **27** (1), 17
6. KORPONAY-SZABÓ, I. R., *et al.*, *Aliment. Pharmacol. Ther.* (2005) **22** (8), 729
7. Price, C. P., and Van den Bruel, A., *Point of Care* (2017) **16** (3), 112
8. Pfäfflin, A., and Schleicher, E., *Anal. Bioanal. Chem.* (2009) **393** (5), 1473
9. Edwards, G., *et al.*, *Alcohol-related disabilities*. World Health Organization: 1977
10. Lerner, J. W., *et al.*, (1997)
11. Antia, R., *et al.*, *Nature* (2003) **426** (6967), 658
12. Vilariño-Güell, C., *et al.*, *The American Journal of Human Genetics* (2011) **89** (1), 162
13. Barbosa, A., and Palacios, M. J., *Polar Biology* (2009) **32** (8), 1095
14. Stuart, K., *et al.*, *The Journal of clinical investigation* (2008) **118** (4), 1301
15. Peleg, A. Y., and Hooper, D. C., *New England Journal of Medicine* (2010) **362** (19), 1804
16. Johnson, R. T., *Viral infections of the nervous system*. Lippincott-Raven Philadelphia: 1998
17. Richardson, M. D., and Warnock, D. W., *Fungal infection: diagnosis and management*. John Wiley & Sons: 2012
18. Speich, B., *et al.*, *The Lancet Infectious Diseases* (2016) **16** (1), 87
19. Bruno, A., *et al.*, *Neurology* (1999) **52** (2), 280
20. Tirschwell, D., *et al.*, *Neurology* (2004) **63** (10), 1868
21. Schlechte, J. A., *et al.*, *The Journal of Clinical Endocrinology & Metabolism* (1983) **56** (6), 1120
22. Dahlgren, E., *et al.*, *Fertility and sterility* (1992) **57** (3), 505
23. Lewandrowski, E. L., and Lewandrowski, K., *J Hosp Adm* (2013) **2** (2), 125
24. Clerc, O., and Greub, G., *Clinical Microbiology and Infection* (2010) **16** (8), 1054
25. Heneghan, C., *et al.*, *The Lancet* (2012) **379** (9813), 322
26. Yetisen, A. K., *et al.*, *Lab on a Chip* (2013) **13** (12), 2210
27. Srivastava, T., *et al.*, *J Hematol Transfus* (2014) **2** (3), 1028
28. Chan, T., and Gu, F., *Biosens. Bioelectron.* (2013) **42**, 12
29. Zhao, W., *et al.*, *ChemBioChem* (2007) **8** (7), 727
30. Morbioli, G. G., *et al.*, *Anal. Chim. Acta* (2017) **970**, 1
31. Dungchai, W., *et al.*, *Anal. Chim. Acta* (2010) **674** (2), 227
32. Luan, Q., *et al.*, *Sens. Actuators, B* (2017) **251**, 349
33. Wen, Y., *et al.*, *Scientific reports* (2012) **2**, 867
34. Cha, J., *et al.*, *Biosens. Bioelectron.* (2003) **18** (10), 1241
35. Pang, Y., *et al.*, *Int. J. Electrochem. Sci.* (2007) **2**, 681
36. Wang, P., *et al.*, *Biosens. Bioelectron.* (2012) **32** (1), 238
37. Zang, D., *et al.*, *Chem. Commun.* (2012) **48** (39), 4683
38. Bhattacharjee, M., *et al.*, *Biosens. Bioelectron.* (2017) **94**, 544
39. Ruiz, V., *et al.*, *Sens. Actuators, B* (2015) **218**, 73
40. Barbosa, C., and Dong, T., Modelling and design of a capacitive touch sensor for urinary tract infection detection at the point-of-care. In *2014 36th Annual International Conference of the IEEE Engineering in Medicine and Biology Society*, IEEE(2014), pp 4995
41. Hu, J., *et al.*, *Talanta* (2017) **165**, 419
42. Cheng, C., *et al.*, *Electrophoresis* (2017) **38** (12), 1617
43. Tanaka, Y., *et al.*, *Analytical chemistry* (2011) **83** (9), 3352
44. Zhao, J., *et al.*, *Journal of membrane science* (2012) **403**, 203
45. Albareda-Sirvent, M., *et al.*, *Sens. Actuators, B* (2000) **69** (1-2), 153
46. Sassolas, A., *et al.*, *Biotechnol. Adv.* (2012) **30** (3), 489
47. Basak, M., *et al.*, *ACS Applied Bio Materials* (2022) **5** (11), 5321
48. An, J. E., *et al.*, *ACS sensors* (2022) **7** (1), 99
49. Zhu, X., *et al.*, *Analyst* (2014) **139** (11), 2850
50. Ren, X., *et al.*, *ACS Sens.* (2017) **2** (9), 1267
51. Baldini, F., *et al.*, *Anal. Bioanal. Chem.* (2009) **393** (4), 1183
52. Tsalis, T. A., *et al.*, (2020) **27** (4), 1617
53. Kathirvel, S., and Thakur, J. S., *International Journal of Noncommunicable Diseases* (2018) **3** (1), 3
54. Antia, R., *et al.*, (2003) **426** (6967), 658
55. Vilariño-Güell, C., *et al.*, (2011) **89** (1), 162

56. Stuart, K., *et al.*, (2008) **118** (4), 1301
57. Starfield, B. J. A. J. o. P. H., (1996) **86** (10), 1365
58. Bajpai, N., and Goyal, S., (2004)
59. Sheeba, A., *et al.*, (2010), 215
60. Gopalakrishnan, S., *et al.*, (2014) **3** (4), 424
61. Krishnan, A., *et al.*, (2021) **21**, 1
62. Tahir, M., *et al.*, (2012) **4** (12), 2025
63. Anderson, G. G., *et al.*, (2003) **301** (5629), 105
64. Sibley, W., *et al.*, (1985) **325** (8441), 1313
65. Mirsky, H. S., and Cuttner, J. J. C., (1972) **30** (2), 348
66. Couch, J. A. J. T. B. o. C., Pathobiology, (1983) **6**, 79
67. Kahn, B. B. J. D., (1996) **45** (11), 1644
68. Leto, D., and Saltiel, A. R. J. N. r. M. c. b., (2012) **13** (6), 383
69. Olefsky, J. M. J. D., (1976) **25** (12), 1154
70. Tirschwell, D., *et al.*, (2004) **63** (10), 1868
71. Schlechte, J. A., *et al.*, (1983) **56** (6), 1120
72. Dahlgren, E., *et al.*, (1992) **57** (3), 505
73. Mitchell, R., *et al.*, (2003) **361** (9367), 1447
74. Sairam, M., *et al.*, *Separation & Purification Reviews* (2006) **35** (4), 249
75. Glaser, D. L., and Kaplan, F. S. J. S., (1997) **22** (24), 12S
76. Roop, J. J. R. J. o. L. S., Bioinformatics, Pharmaceuticals, and Chemical, (2018) **4**, 237
77. Mederos, M. A., *et al.*, (2021) **325** (4), 382
78. Berger, A., *et al.*, (2004) **29** (1), 13
79. Heikkinen, T., and Järvinen, A. J. T. L., (2003) **361** (9351), 51
80. Domachowske, J., and Suryadevara, M.,
81. Derakhshan-Nezhad, E. J. J. o. M. B., (2023) **11** (1-2), 36
82. Zaki, S. R., and Keating, M. K. J. P. p., (2018), 244
83. Wade, J. C. J. A. E. P. B., (2006) **2006** (1), 368
84. Davidson, R., *et al.*, *Oxford handbook of tropical medicine*. Oxford University Press: 2022
85. Dunachie, S. J., *et al.*, Infectious Disease. In *Medicine for Finals and Beyond*, CRC Press(2022), pp 21
86. Lewandrowski, E. L., and Lewandrowski, K. J. J. H. A., (2013) **2** (2), 125
87. Madimenos, F. C., *et al.*, (2022) **34** (11), e23808
88. Dima, K., Point of care testing (POCT) present and future. Google Scholar There is no corresponding record for this reference(2021)
89. Madimenos, F. C., *et al.*, *American Journal of Human Biology* (2022) **34** (11), e23808
90. Price, C. P., and John, A. S., *Point-of-care testing: making innovation work for patient-centered care*. American Association for Clinical Chemistry: 2012
91. Butler, S. A., *et al.*, *Clinical chemistry* (2001) **47** (12), 2131
92. Vicziany, M., and Hardikar, J., *Diagnostics* (2022) **12** (3), 644
93. Pezzuto, F., *et al.*, *The Open Public Health Journal* (2019) **12** (1)
94. WHO, (2014)
95. St John, A., and Price, C. P., *The Clinical Biochemist Reviews* (2014) **35** (3), 155
96. Schumacher, S., *et al.*, *Lab on a Chip* (2012) **12** (3), 464
97. Jung, W., *et al.*, *Microelectronic Engineering* (2015) **132**, 46
98. Stürenburg, E., and Junker, R., *Deutsches Ärzteblatt International* (2009) **106** (4), 48
99. Cho, I.-H., *et al.*, *Sensors and Actuators B: Chemical* (2015) **213**, 209
100. Wang, K., *et al.*, *Nano Biomed. Eng* (2016) **8** (3), 172
101. Tran, V., *et al.*, *Angewandte Chemie International Edition* (2019) **58** (2), 442
102. Maheshwari, N., *et al.*, *J. ISSS* (2014) **3** (2), 39
103. Wang, L.-J., *et al.*, *Biosensors and Bioelectronics* (2017) **87**, 686
104. Zhang, M., *et al.*, *Materials Today Bio* (2022) **14**, 100254
105. Andersen, G. N., *et al.*, *Journal of Ultrasound in Medicine* (2015) **34** (4), 627
106. Zhang, K., *et al.*, *Advanced Healthcare Materials* (2021) **10** (17), 2100734
107. Cui, F., *et al.*, *ACS sensors* (2020) **5** (11), 3346
108. Jain, S., *et al.*, *Biosensors and Bioelectronics* (2021) **179**, 113074
109. Parihar, A., *et al.*, *Bioengineering & Translational Medicine* (2023), e10481
110. Song, Y., *et al.*, *Advanced Materials* (2011) **23** (37), 4215
111. Zhao, W., *et al.*, *ChemBioChem* (2008) **9** (15), 2363
112. Ronkainen, N. J., *et al.*, *Chemical Society Reviews* (2010) **39** (5), 1747
113. Merkoçi, A., *The FEBS journal* (2007) **274** (2), 310

114. Shetty, S. S., *et al.*, *Materials Today: Proceedings* (2022) **55**, 122
115. Maanaki, H., *et al.*, *Biosensors and Bioelectronics: X* (2023) **15**, 100402
116. Berggren, C., *et al.*, *Electroanalysis: An International Journal Devoted to Fundamental and Practical Aspects of Electroanalysis* (2001) **13** (3), 173
117. Weaver, S., *et al.*, *Biosensors and Bioelectronics* (2022), 115014
118. Skládal, P., *TrAC Trends in Analytical Chemistry* (2016) **79**, 127
119. Tombelli, S., Piezoelectric biosensors for medical applications. In *Biosensors for medical applications*, Elsevier(2012), pp 41
120. Mejía-Salazar, J., and Oliveira Jr, O. N., *Chemical reviews* (2018) **118** (20), 10617
121. Bantz, K. C., *et al.*, *Physical chemistry chemical physics* (2011) **13** (24), 11551
122. Vo-Dinh, T., *et al.*, *Journal of biophotonics* (2010) **3** (1-2), 89
123. Benbrook, D. M., *Journal of Pharmacological and toxicological methods* (2002) **47** (3), 169
124. Mitra, S., and Basak, M., *Materials Today* (2022) **57**, 225
125. Shalaev, V. M., and Kawata, S., *Nanophotonics with surface plasmons*. Elsevier: 2006
126. Van Der Merwe, P. A., *Protein-ligand interactions: hydrodynamics and calorimetry* (2001) **1**, 137
127. Snopok, B., *Theoretical and Experimental Chemistry* (2012) **48** (5), 283
128. Piliarik, M., *et al.*, *Biosensors and Biodetection* (2009), 65
129. Liu, Y., *et al.*, *Scientific reports* (2015) **5** (1), 12864
130. Li, J., *et al.*, *Optics Express* (2020) **28** (9), 14007
131. Wang, Q., *et al.*, *Nanoscale* (2022) **14** (3), 564
132. Dostalek, J., *et al.*, *Sensors and actuators B: Chemical* (2001) **76** (1-3), 8
133. Zhao, Y., *et al.*, *Biosensors and Bioelectronics* (2019) **142**, 111505
134. Wu, T., *et al.*, *Optics express* (2017) **25** (17), 20313
135. Kim, D., *Applied Optics* (2005) **44** (16), 3218
136. Wang, Q., *et al.*, *IEEE Transactions on Nanotechnology* (2019) **18**, 1137
137. Jatschka, J., *et al.*, *Sensing and bio-sensing research* (2016) **7**, 62
138. Hutter, E., and Fendler, J. H., *Advanced materials* (2004) **16** (19), 1685
139. Mayer, K. M., and Hafner, J. H., *Chemical reviews* (2011) **111** (6), 3828
140. Angelomé, P. C., *et al.*, *Chemistry of Materials* (2012) **24** (7), 1393
141. Hartland, G. V., *Chemical reviews* (2011) **111** (6), 3858
142. Jain, P. K., and El-Sayed, M. A., *Chemical Physics Letters* (2010) **487** (4-6), 153
143. Zhang, Y. J., *et al.*, *Advanced Materials* (2021) **33** (50), 2005900
144. Jeong, S., *et al.*, *ACS applied materials & interfaces* (2019) **11** (47), 44458
145. Li, X., *et al.*, *Chemical Society Reviews* (2016) **45** (11), 3145
146. Kessentini, S., *et al.*, *The Journal of Physical Chemistry C* (2014) **118** (6), 3209
147. Yang, K., *et al.*, *Advanced Materials* (2021) **33** (50), 2007988
148. Zheng, P., *et al.*, *Physical Chemistry Chemical Physics* (2015) **17** (33), 21211
149. Basak, M., *et al.*, *ACS Applied Bio Materials* (2021) **4** (6), 5378
150. Saha, A., *et al.*, *The Journal of Physical Chemistry C* (2009) **113** (43), 18492
151. Zhang, R., *et al.*, *Nature* (2013) **498** (7452), 82
152. Mosca, S., *et al.*, *Nature Reviews Methods Primers* (2021) **1** (1), 21
153. Sahu, B. K., *et al.*, *Applied Surface Science* (2021) **537**, 147615
154. Neubrech, F., *et al.*, *Chemical reviews* (2017) **117** (7), 5110
155. Kravets, V. G., *et al.*, *Chemical reviews* (2018) **118** (12), 5912
156. Feng, J., *et al.*, *Nano letters* (2012) **12** (2), 602
157. Inan, H., *et al.*, *Chemical Society Reviews* (2017) **46** (2), 366
158. Snoek, B. C., *et al.*, *Scientific reports* (2019) **9** (1), 1
159. Duraisamy, K., *et al.*, *Advances in Biological Research* (2011) **5** (4), 226
160. Arbyn, M., *et al.*, *The Lancet Global Health* (2020) **8** (2), e191
161. Masilamani, V., *et al.*, *Journal of biomedical optics* (2012) **17** (9), 098001
162. Abulafia, O., *et al.*, *Gynecologic oncology* (2003) **90** (1), 137
163. Dillner, J., *et al.*, *Bmj* (2008) **337**
164. Qaseem, A., *et al.*, *Annals of internal medicine* (2014) **161** (1), 67
165. Bates, C. K., *et al.*, *Journal of general internal medicine* (2011) **26** (6), 651
166. Garg, R., and Desai, R., *Int J Adv Med* (2017) **4** (3), 799
167. Saslow, D., *et al.*, *CA: a cancer journal for clinicians* (2012) **62** (3), 147
168. Sankaranarayanan, R., *et al.*, *New England Journal of Medicine* (2009) **360** (14), 1385
169. Cuzick, J., *Jama* (2000) **283** (1), 108
170. Ramanujam, N., *et al.*, *Proceedings of the National Academy of Sciences* (1994) **91** (21), 10193
171. Sankaranarayanan, R., *et al.*, *International Journal of Cancer* (2003) **106** (3), 404

172. Nene, B., *et al.*, *International journal of cancer* (1996) **68** (6), 770
173. Loiudice, L., *et al.*, *European journal of cancer prevention* (1998) **7**, 295
174. Baldauf, J.-J., *et al.*, *European Journal of Obstetrics & Gynecology and Reproductive Biology* (1995) **58** (1), 33
175. Schneider, D. L., *et al.*, *American journal of obstetrics and gynecology* (1999) **180** (2), 290
176. Owen, W. F., *Kidney international* (1998) **54** (2), 627
177. Uhlén, M., *et al.*, *Molecular & cellular proteomics* (2005) **4** (12), 1920
178. Chalupa, P., *et al.*, *Infection* (2011) **39** (5), 411
179. Kim, S.-J., *et al.*, *Fisheries and aquatic sciences* (2001) **4** (1), 32
180. Lam, T. C., *et al.*, *Journal of proteome research* (2007) **6** (11), 4135
181. Trivedi, D. K., *et al.*, *ACS central science* (2019) **5** (4), 599
182. Hoffman, W. S., *Journal of Biological Chemistry* (1937) **120** (1), 51
183. Suzuki, M., *et al.*, *Investigative Ophthalmology & Visual Science* (2010) **51** (9), 4557
184. Foley III, J. D., *et al.*, *Oral surgery, oral medicine, oral pathology and oral radiology* (2012) **114** (2), 207
185. Choi, P., *et al.*, *Archives of Otolaryngology–Head & Neck Surgery* (2008) **134** (5), 539
186. Van Raemdonck, G. A., *et al.*, *PLoS One* (2014) **9** (9), e106488
187. Mandal, N., *et al.*, *IEEE Sensors Journal* (2020)
188. Maity, S., *et al.*, *ACS Sustainable Chemistry & Engineering* (2020)
189. Luppa, P. B., *et al.*, *TrAC, Trends Anal. Chem.* (2011) **30** (6), 887
190. Jang, A., *et al.*, *Meas. Sci. Technol.* (2011) **22** (3), 032001
191. Durham, J., and Pizzino, S., *Prehospital and Disaster Medicine* (2019) **34** (s1), s32
192. Buttner, W. J., *et al.*, *Int. J. Hydrogen Energy* (2011) **36** (3), 2462
193. Goto, M., *et al.*, Point-of-care SH-SAW biosensor. In *2010 IEEE International Ultrasonics Symposium*, IEEE(2010), pp 736
194. Gillespie, P., *et al.*, *Analyst* (2019) **144** (1), 114
195. Huang, C.-W., *et al.*, *Lab Chip* (2013) **13** (22), 4451
196. Nie, B., *et al.*, *Adv. Mater.* (2015) **27** (39), 6055
197. Wang, Y., *et al.*, *Small Methods* (2017) **1** (11), 1700197
198. Khoury, J., *et al.*, Optically actuated MEMS deformable mirror device. In *Frontiers in Optics*, Optical Society of America(2012), p FW5E. 3
199. Wu, Y., *et al.*, *Clin. Chim. Acta* (2015) **448**, 133
200. Horie, K., *et al.*, *Hum. Reprod.* (1993) **8** (11), 1955
201. O'brien, E., *et al.*, *Bmj* (2001) **322** (7285), 531
202. Wang, Y.-C., and Han, J., *Lab Chip* (2008) **8** (3), 392
203. Sepúlveda, B., *et al.*, *nano today* (2009) **4** (3), 244
204. Iarossi, M., *et al.*, *ACS omega* (2018) **3** (4), 3805
205. Peng, H., and Chen, I. A., *ACS nano* (2018) **13** (2), 1244
206. Laemmli, U. K., *nature* (1970) **227** (5259), 680
207. Fagnano, C., and Fini, G., *Journal of Raman spectroscopy* (1992) **23** (11), 637
208. Kengne-Momo, R., *et al.*, *International Journal of Spectroscopy* (2012) **2012**
209. Rudzinski, W. E., and Francis, K., *Applied Surface Science* (2010) **256** (17), 5399
210. Gordeeva, O., Cancer-testis antigens: unique cancer stem cell biomarkers and targets for cancer therapy. In *Seminars in cancer biology*, Elsevier(2018), Vol. 53, pp 75
211. Chakrabarti, R., *et al.*, *Asian journal of andrology* (2007) **9** (4), 445
212. Yeom, S.-H., *et al.*, *Sensors and Actuators B: Chemical* (2013) **177**, 376
213. Kelly, K. L., *et al.*, The optical properties of metal nanoparticles: the influence of size, shape, and dielectric environment. ACS Publications(2003)
214. Rechberger, W., *et al.*, *Optics communications* (2003) **220** (1-3), 137
215. Willets, K. A., and Van Duyne, R. P., *Annual review of physical chemistry* (2007) **58** (1), 267
216. El-Sayed, M. A., *Accounts of chemical research* (2001) **34** (4), 257
217. Michaels, A. M., *et al.*, *Journal of the American Chemical Society* (1999) **121** (43), 9932
218. Kelly, K. L., *et al.*, The optical properties of metal nanoparticles: the influence of size, shape, and dielectric environment. ACS Publications(2003), Vol. 107, pp 668
219. Smitha, S., *et al.*, *Nanotechnology* (2011) **22** (26), 265705
220. Dreaden, E. C., *et al.*, *Chemical Society Reviews* (2012) **41** (7), 2740
221. Rozanova, N., and Zhang, J., *Science in China Series B: Chemistry* (2009) **52** (10), 1559
222. Oulton, R. F., *et al.*, *nature photonics* (2008) **2** (8), 496
223. Kneipp, K., *et al.*, *Physical review letters* (1997) **78** (9), 1667
224. Halas, N. J., *et al.*, *Chemical reviews* (2011) **111** (6), 3913

225. Lin, K.-Q., *et al.*, *The Journal of Physical Chemistry C* (2016) **120** (37), 20806
226. Huang, Z., *et al.*, *Nano Research* (2019) **12** (2), 449
227. Pal, S. K., *et al.*, *RSC advances* (2019) **9** (72), 42145
228. Wei, W., *et al.*, *Angewandte Chemie International Edition* (2019) **58** (35), 11956
229. Liu, X., *et al.*, *Advanced Materials* (2015) **27** (45), 7314
230. Jia, K., *et al.*, *ACS Applied Materials & Interfaces* (2014) **6** (1), 219
231. Nehl, C. L., and Hafner, J. H., *Journal of Materials Chemistry* (2008) **18** (21), 2415
232. Anker, J. N., *et al.*, *Nanoscience and Technology: A Collection of Reviews from Nature Journals* (2010), 308
233. Tian, L., *et al.*, *Journal of the American Chemical Society* (2021) **143** (23), 8631
234. Mitra, S., and Basak, M., *Materials Today* (2022)
235. Cha, H., *et al.*, *ACS nano* (2014) **8** (8), 8554
236. Hu, Y., *et al.*, *Advanced Materials* (2016) **28** (41), 9152
237. Thacker, V. V., *et al.*, *Nature communications* (2014) **5** (1), 1
238. Indrasekara, A. S. D., *et al.*, *Advanced healthcare materials* (2013) **2** (10), 1370
239. Kim, H.-M., *et al.*, *IEEE Transactions on Instrumentation and Measurement* (2021) **70**, 1
240. Zhang, Q., *et al.*, *Analytical Chemistry* (2021) **93** (6), 3308
241. Acimovic, S. S., *et al.*, *ACS nano* (2009) **3** (5), 1231
242. Liu, Y., *et al.*, *Biosensors and Bioelectronics* (2020) **148**, 111839
243. Zhou, C., *et al.*, *ACS Applied Materials & Interfaces* (2021) **13** (28), 32780
244. Mach, K. E., *et al.*, *Trends in pharmacological sciences* (2011) **32** (6), 330
245. Mansour, A., *et al.*, (2009)
246. Natarajan, V., *Surgery (Oxford)* (2008) **26** (5), 193
247. Kunin, C. M., *Clinical Infectious Diseases* (1994) **18** (1), 1
248. Health, M. o., and India, F. W. G. o., (2021)
249. Vasudevan, R., *J Microbiol Exp* (2014) **1** (2), 00008
250. Goldstein, I., *Journal of women's health* (2010) **19** (3), 425
251. Akbar, D. H., and Board, A., *Saudi medical journal* (2001) **22** (4), 326
252. Wilson, M. L., and Gaido, L., *Clinical infectious diseases* (2004) **38** (8), 1150
253. Leman, P., *European Journal of Emergency Medicine* (2002) **9** (2), 141
254. Hurlbut III, T. A., and Littenberg, B., *American journal of clinical pathology* (1991) **96** (5), 582
255. El-Ghar, M. A., *et al.*, *Medicina* (2021) **57** (1), 32
256. Lawrentschuk, N., *et al.*, *International journal of urology* (2006) **13** (4), 350
257. Granger, J. H., *et al.*, *Chemical Society Reviews* (2016) **45** (14), 3865
258. Gür, S. D., *et al.*, *Materials Science and Engineering: C* (2019) **104**, 109869
259. Galvan, D. D., and Yu, Q., *Advanced healthcare materials* (2018) **7** (13), 1701335
260. Jin, C., *et al.*, *Materials Today Bio* (2022), 100263
261. Raj, V., *et al.*, *Sensing and bio-sensing research* (2015) **5**, 33
262. Zagorovsky, K., *et al.*, *ACS Nanoscience Au* (2022)
263. Tang, M., *et al.*, *Frontiers in Chemistry* (2020) **8**, 181
264. Adrover-Jaume, C., *et al.*, *Analyst* (2020) **145** (24), 7916
265. Özgür, E., *et al.*, *Talanta* (2020) **212**, 120778
266. Nair, S., *et al.*, *Analyst* (2020) **145** (6), 2133
267. Gomez-Cruz, J., *et al.*, *Biosensors and Bioelectronics* (2018) **106**, 105
268. Yeung, W. K., *et al.*, *Analyst* (2018) **143** (19), 4715
269. Bakthavathsalam, P., *et al.*, *Journal of nanobiotechnology* (2012) **10** (1), 1
270. Wang, H., *Scientific reports* (2018) **8** (1), 1
271. Rigo, M. V., *et al.*, *Vibrational Spectroscopy* (2011) **57** (2), 315
272. Asapu, R., *et al.*, *Nature Protocols* (2016) **11**, 664
273. Ren, J., *et al.*, *PloS one* (2019) **14** (6), e0218325
274. Yüce, M., and Kurt, H., *Rsc Advances* (2017) **7** (78), 49386
275. Wu, R., *et al.*, *Frontiers in chemistry* (2020) **8**, 121
276. Kubackova, J., *et al.*, *Physical Chemistry Chemical Physics* (2014) **16** (23), 11461
277. Gillibert, R., *et al.*, *Analyst* (2018) **143** (1), 339
278. Garcia-Rico, E., *et al.*, *Chemical Society Reviews* (2018) **47** (13), 4909
279. Szekeres, G. P., and Kneipp, J., *Frontiers in chemistry* (2019) **7**, 30
280. David, C., Raman spectroscopy for proteins. Horiba Scientific2012.
281. Wu, Z.-S., *et al.*, *Analytical chemistry* (2010) **82** (9), 3890
282. Zhao, W., *et al.*, *Journal of the American Chemical Society* (2008) **130** (11), 3610
283. Xie, Y., *et al.*, *Sensors and Actuators B: Chemical* (2021) **339**, 129865

284. Zhang, H., *et al.*, *Biosensors and Bioelectronics* (2015) **74**, 872
285. Arsenault, B. J., *et al.*, (2011) **8** (4), 197
286. Soppert, J., *et al.*, (2020) **159**, 4
287. Schade, D. S., *et al.*, (2020) **26** (12), 1514
288. Morris, A. L., and Mohiuddin, S. S., (2020)
289. Trajkovska, K. T., and Topuzovska, S. J. A. j. o. c., (2017) **18** (2), 149
290. Mayes, P. A., and Botham, K. M. J. a. L. m. b., (2003), 219
291. Norum, K. R., *et al.*, (1983) **63** (4), 1343
292. Markaki, I., *et al.*, (2014) **23** (1), e47
293. Lawes, C. M., *et al.*, (2004), 391
294. Robinson, D. J. J. o. C. P. S., (1973) **5**, 5
295. Brown, W. V. J. J. o. c. l., (2007) **1** (1), 7
296. Liu, J., *et al.*, (2013) **12**, 1
297. Nordestgaard, B. G., and Varbo, A. J. T. L., (2014) **384** (9943), 626
298. Nordestgaard, B. G. J. J. o. t. A. C. o. C., (2017) **70** (13), 1637
299. Children, N. E. P. o. B. C. L. i., and Pediatrics, A. J., (1992) **89** (3), 495
300. Stein, E., and Myers, G. J. C. c., (1995) **41** (10), 1421
301. Aldulaimi, A. K. O., *et al.*, (2023) **15** (9), 778
302. Nantaphol, S., *et al.*, (2015) **207**, 193
303. Amiri, M., and Arshi, S. J. E., (2020) **32** (7), 1391
304. Hefnawy, M. A., *et al.*, (2023), 117169
305. Bhardwaj, S. K., *et al.*, (2019) **7** (4), 1598
306. Mondal, K., *et al.*, (2017) **246**, 202
307. Pundir, C., and Aggarwal, V. J. A. b., (2017) **517**, 56
308. Khaliq, N., *et al.*, (2020) **302**, 127200
309. Zhang, W., *et al.*, (2014) **2** (48), 8490
310. Yang, D., *et al.*, (2023) **5** (2), 593
311. Vijayalakshmi, A., *et al.*, (2008) **23** (11), 1708
312. Hooda, V., *et al.*, (2018) **46** (sup2), 626
313. Pérez-Jiménez, A. I., *et al.*, (2020) **11** (18), 4563
314. Schlücker, S. J. A. C. I. E., (2014) **53** (19), 4756
315. Tahir, M. A., *et al.*, (2021) **13** (27), 11593
316. Gargiulo, J., *et al.*, (2019) **52** (9), 2525
317. Lin, S., *et al.*, (2021) **13** (44), 53289
318. Yang, X., *et al.*, (2023) **19** (22), 2205659
319. Haes, A. J., *et al.*, (2004) **108** (22), 6961
320. Dumont, E., *et al.*, (2016) **8** (10), 1077
321. Zhang, Y., *et al.*, (2017) **90**, 1
322. Yu, H., *et al.*, (2019) **5** (1), 45
323. Hartland, G. V. J. T. J. o. P. C. L., Metal at the Nanoscale: Manipulating Matter to Control Light. ACS Publications(2012), Vol. 3, pp 959
324. Giannini, V., *et al.*, (2010) **6** (22), 2498
325. Qian, X.-M., and Nie, S. M. J. C. S. R., (2008) **37** (5), 912
326. Radziuk, D., and Moehwald, H. J. P. C. C. P., (2015) **17** (33), 21072
327. Sun, D., *et al.*, (2019) **91** (24), 15484
328. Nikoobakht, B., and El-Sayed, M. A. J. C. o. M., (2003) **15** (10), 1957
329. Scarabelli, L., *et al.*, A "tips and tricks" practical guide to the synthesis of gold nanorods. ACS Publications(2015), Vol. 6, pp 4270
330. Zhu, J., *et al.*, (2018) **255**, 2927
331. Vial, S., and Wenger, J. J. A., (2017) **142** (18), 3484
332. Shikha, S., *et al.*, (2017) **7** (68), 42845
333. Wu, J., *et al.*, (2022) **14** (43), 4292
334. Rhee, K., *et al.*, (2023) **15** (5), 2087
335. Tian, X., *et al.*, (2012) **2** (22), 8289
336. Gabudean, A., *et al.*, (2011) **993** (1-3), 420
337. Putri, A. E., *et al.*, (2021) **536**, 147847
338. Jia, K., *et al.*, (2014) **6** (1), 219
339. Nirala, N. R., *et al.*, (2018) **190**, 506
340. Basak, M., *et al.*, (2021) **4** (6), 5378
341. Caudill, S. P., *et al.*, (1998) **44** (5), 1063

342. Wojnarowska-Nowak, R., *et al.*, (2020) **22** (5), 107
343. Kho, K. W., *et al.*, (2012) **6** (6), 4892
344. Ma, H., *et al.*, (2019) **91** (15), 9376
345. Torales, J., *et al.*, *International Journal of Social Psychiatry* (2020) **66** (4), 317
346. Rothan, H. A., and Byrareddy, S. N., *Journal of autoimmunity* (2020) **109**, 102433
347. Gudi, S. K., *et al.*, *medRxiv* (2020)
348. Kim, S., *et al.*, *International Journal of Hospitality Management* **93**, 102797
349. Roy, C. J., and Milton, D. K., (2004)
350. Sattar, S. A., *et al.*, *Critical Reviews in Environmental Science and Technology* (1987) **17** (2), 89
351. Riley, E., *et al.*, *American journal of epidemiology* (1978) **107** (5), 421
352. Liu, Y., *et al.*, *Viruses* (2020) **12** (10), 1174
353. Scharfman, B., *et al.*, *Experiments in Fluids* (2016) **57** (2), 1
354. Yang, S., *et al.*, *Journal of Aerosol Medicine* (2007) **20** (4), 484
355. Bourouiba, L., *Jama* (2020) **323** (18), 1837
356. Olch, P. D., *Annals of surgery* (1960) **152** (5), 923
357. Wells, W. F., *American Journal of Hygiene* (1934) **20**, 611
358. Roy, C. J., and Milton, D. K., Airborne transmission of communicable infection-the elusive pathway; ARMY MEDICAL RESEARCH INST OF INFECTIOUS DISEASES FORT DETRICK MD …2004
359. Frankova, V., *Acta virologica* (1975) **19** (1), 29
360. Organization, W. H., Modes of transmission of virus causing COVID-19: implications for IPC precaution recommendations: scientific brief, 27 March 2020; World Health Organization2020
361. Feng, Y., *et al.*, *Journal of aerosol science* (2020), 105585
362. Aliabadi, A. A., *et al.*, CFD simulation of human coughs and sneezes: a study in droplet dispersion, heat, and mass transfer. In *ASME International Mechanical Engineering Congress and Exposition*, (2010), Vol. 44441, pp 1051
363. Klompas, M., *et al.*, *Jama* (2020)
364. Bhardwaj, R., and Agrawal, A., *Physics of Fluids* (2020) **32** (6), 061704
365. Duguid, J., *Epidemiology & Infection* (1946) **44** (6), 471
366. Diwan, S. S., *et al.*, *Transactions of the Indian National Academy of Engineering* (2020) **5**, 255
367. Dbouk, T., and Drikakis, D., *Physics of Fluids* (2020) **32** (5), 053310
368. Busco, G., *et al.*, *Physics of Fluids* (2020) **32** (7), 073309
369. Zhang, J., *et al.*, *Environmental modelling & software* (2014) **58**, 71
370. Peng, S., *et al.*, *Science of The Total Environment* (2020), 142090
371. Gupta, J. K., *et al.*, *Indoor air* (2009) **19** (6), 517
372. Mittal, R., *et al.*, *Journal of fluid Mechanics* (2020) **894**
373. Sun, W., and Ji, J., *Indoor and Built Environment* (2007) **16** (6), 493
374. Wei, J., and Li, Y., *Building and Environment* (2015) **93**, 86
375. Chen, W., *et al.*, *Building and Environment* (2020) **176**, 106859
376. Mirzaie, M., *et al.*, *Journal of Hazardous Materials* (2021) **420**, 126587
377. Shao, S., *et al.*, *Journal of aerosol science* (2021) **151**, 105661
378. Zhang, Y., *et al.*, *Sustainable Cities and Society* (2019) **51**, 101721
379. Zhao, B., *et al.*, *Building and Environment* (2005) **40** (8), 1032
380. Crawford, C., *et al.*, *Scientific reports* (2021) **11** (1), 1
381. Conticini, E., *et al.*, *Environmental pollution* (2020), 114465
382. Mariam, *et al.*, *ACS Omega* (2021)
383. Diwan, S. S., *et al.*, *Transactions of the Indian National Academy of Engineering* (2020), 1
384. Basu, S., *et al.*, *Physics of Fluids* (2020) **32** (12), 123317
385. Chaudhuri, S., *et al.*, *Physics of Fluids* (2020) **32** (6), 063309
386. Huang, N.-Y., *et al.*, *Chemical Engineering Research and Design* (2021) **170**, 239
387. Netz, R. R., *The Journal of Physical Chemistry B* (2020) **124** (33), 7093
388. Feng, Y., *et al.*, *Journal of aerosol science* (2020) **147**, 105585
389. Pendar, M.-R., and Páscoa, J. C., *Physics of Fluids* (2020) **32** (8), 083305
390. Zhao, L., *et al.*, *Nano letters* (2020) **20** (10), 7744
391. Wang, C. C., *et al.*, *Science* (2021) **373** (6558), eabd9149
392. Nishimura, H., *et al.*, *PloS one* (2013) **8** (11), e80244
393. Bhattacharyya, S., *et al.*, *Chemical Engineering Science* (2006) **61** (13), 4451
394. Pan, Y., *et al.*, *The Lancet infectious diseases* (2020) **20** (4), 411
395. Anand, S., and Mayya, Y., *Scientific Reports* (2020) **10** (1), 1
396. Liu, C., *et al.*, *Structure* (2020) **28** (11), 1218
397. Bahl, P., *et al.*, *Experiments in Fluids* (2020) **61** (8), 1

398. Shafaghi, A. H., *et al.*, *Fluids* (2020) **5** (3), 113
399. Sun, Z., *et al.*, *Science of The Total Environment* (2020) **746**, 141347
400. Zhao, J., *et al.*, *Clinical Infectious Diseases* (2021) **73** (2), 328
401. Velavan, T. P., and Meyer, C. G., *Tropical medicine & international health* (2020) **25** (3), 278
402. Chen, N., *et al.*, *The lancet* (2020) **395** (10223), 507
403. Kumar, A., *et al.*, *Public Health in Practice* (2020) **1**, 100009
404. Finlay, B. B., *et al.*, *Proceedings of the National Academy of Sciences* (2021) **118** (6)
405. Abu Hammad, O., *et al.*, Factors influencing global variations in COVID-19 cases and fatalities; a review. In *Healthcare*, Multidisciplinary Digital Publishing Institute(2020), Vol. 8, p 216
406. Godri Pollitt, K. J., *et al.*, *Human genomics* (2020) **14**, 1
407. Islam, M. S., *et al.*, *Infection Control & Hospital Epidemiology* (2020) **41** (10), 1196
408. Liu, J., *et al.*, *Science of the total environment* (2020) **726**, 138513
409. Dawood, A. A., *New microbes and new infections* (2020) **35**, 100673
410. Vilches, T. N., *et al.*, *Vaccine* (2021) **39** (17), 2360
411. Williamson, R. E., and Threadgill, E. D., *Transactions of the ASAE* (1974) **17** (2), 254
412. Ranjan, C., and Najari, V., *Unpublished* (2020)
413. Hart, O. E., and Halden, R. U., *Science of the Total Environment* (2020) **727**, 138406
414. Tamerius, J. D., *et al.*, *PLoS pathogens* (2013) **9** (3), e1003194
415. Foster, H., *Blog post. Harvard University, The Graduate School of Arts and Sciences website* (2014)
416. Busco, G., *et al.*, (2020) **32** (7), 073309
417. Dbouk, T., and Drikakis, D. J. P. o. F., (2020) **32** (5), 053310
418. Wang, J., *et al.*, (2021)
419. Feng, Y., *et al.*, (2020) **147**, 105585
420. Netz, R. R. J. T. J. o. P. C. B., (2020) **124** (33), 7093